Design and Analysis of L-Band Reconfigurable Liquid-Metal Alloy Antennas

Jonathan Tyler Thews

Thesis submitted to the Faculty of the

Virginia Polytechnic Institute and State University

in partial fulfillment of the requirements for the degree of

Master of Science

in

Electrical Engineering

Alan J. Michaels, Chair

Gary S. Brown, Co-Chair

William A. Davis

Robert W. Hendricks

April 27, 2017

Blacksburg, Virginia

Keywords: liquid metal, antenna, reconfigurable, EGaIn, eutectic, gallium, indium, L-band

Design and Analysis of L-Band Reconfigurable Liquid-Metal Alloy Antennas

Jonathan Tyler Thews

Academic Abstract

Efficient reconfigurable antennas are highly sought after in all communication applications for the ability to reduce space cost while maintaining the ability to control the frequency, gain, and polarization. The ability to control these parameters allows a single antenna to maximize its performance in a wide range of scenarios to satisfy changing operating requirements. This thesis will describe reconfigurable antennas using liquid-metal alloys that give the system this ability by injecting or retracting the liquid metal from various channels. After simulations were performed in an electromagnetic simulation software, proof-of-concept models were built, tested, and compared to the simulations to verify the results.

Design and Analysis of L-Band Reconfigurable Liquid-Metal Alloy Antennas

Jonathan Tyler Thews

General Audience Abstract

Antennas that can change the tuned center frequency and/or the direction they are pointing are needed in many different applications. Antenna adaptability allows the system to maximize the physical dimensions of the antenna to satisfy a wide range of situations without losing performance. This thesis describes antennas using a liquid-metal alloy that can make physical adaptations for the need at hand. After simulations were performed using computer software, proof-of-concept models were constructed and empirically validated to verify the simulation models.

Acknowledgments

Most importantly, I would like to thank my father and mother who from the very beginning pushed me to do my best at all times and inspired me to become an engineer. I would also like to thank my brother for his encouragement, friendship, and assistance. To my undergraduate study group, Stephanie "Steph" Winter, John Michael "Mike" McHale, David Liss, Benjamin "Carlos" Carstens, Jessie Wilcox, and Nathan Tennyson, for the many laughs and late nights spent working in the library or lab. You all have taught me very valuable life lessons and have become lifelong friends. Last, I would like to thank the Hume Center researchers for their support and assistance in completing this project.

Contents

List of Figures

List of Tables

List of Abbreviations

A/D	Analog/Digital converter
AESA	Active Electronically Scanned Array
AJ	Anti-Jam
AR	Axial Ratio
AUT	Antenna Under Test
BW	BandWidth
CRPA	Controlled Radiation Pattern Antenna
dB	decibel
dBd	decibel dipole
dBi	decibel isotropic
DRA	Direct Radiating phased Array
E field	Electric field
EGaIn	Eutectic Gallium Indium alloy
EM	ElectroMagnetic
FBW	Fractional BandWidth
FEKO	electromagnetic simulation software tool
FET	Field Effect Transistor
FF	Far Field of the antenna
FNBW	First Null BeamWidth
GA	Genetic Algorithm
Galinstan	eutectic Gallium Indium Tin alloy
GPS	Global Positioning System
GNSS	Global Navigation Satellite System
H field	magnetic field
HPBW	Half-Power BeamWidth
IEEE	Institution of Electrical and Electronics Engineers
L-band	defined by IEEE as $1 - 2$ GHz frequency range
LC	Liquid Crystal

LHC	Left Hand Circular polarization
LP	Linear Polarization
MSDS	Material Safety Data Sheet
MEMS	MicroElectroMechanical System
NaK	Sodium Potassium alloy
NaOH	Sodium Hydroxide
PAA	Phased Array Antenna
PAFR	Phased Array-Fed Reflector antenna
PEC	Perfect Electric Conductor
PESA	Passive Electronically Scanned Array
Q-factor	Quality factor
RF	Radio Frequency
RHC	Right Hand Circular polarization
Rx	receiver/received power
SATCOM	SATellite COMmunications
SDR	Software Defined Radio
SMA	SubMiniature version A connector
S-parameters	Scattering parameters
TRL	Technical Readiness Level
T/R	Transmit/Receive module
Tx	transmitter/transmit power
USRP	Universal Software Radio Peripheral
VNA	Vector Network Analyzer
VSWR	Voltage Standing Wave Ratio

Chapter 1

Introduction

Our society is highly dependent on wireless communications to transmit data and perform day-to-day tasks. These tasks, including access to the User Segment of the Global Positioning System (GPS), Wi-Fi, Bluetooth, cellular phones, etc., have become integrated and integral to our daily lives. Wireless communication may be considered as the transmission of information between two or more points without a direct physical connection. The most common wireless technologies utilize radio waves to transmit the data. The radio frequency (RF) spectrum ranges from 3 kHz to 300 GHz (Fig. 1.1). Fig. 1.1 also shows the United States RF spectrum allocations, which was created to organize this cluttered spectrum. Since the RF spectrum is so large, it is further broken down into different bands described in Appendix A.3. However, with the ever increasing number of wireless services and

users, keeping the wireless networks running efficiently and the frequency spectrum organized has become increasingly more difficult. Too many devices at the same frequency can cause communications at that frequency to become unreliable due to increased interference levels, lowered effective signal-to-noise ratios and/or data collisions. Also, each system can only operate in the frequency band or bands they are assigned, which are not always directly adjacent to each other. Reconfigurable hardware technologies allow devices to be capable of operating in multiple frequency bands, allowing adaptations to different situations to maximize performance of the device.

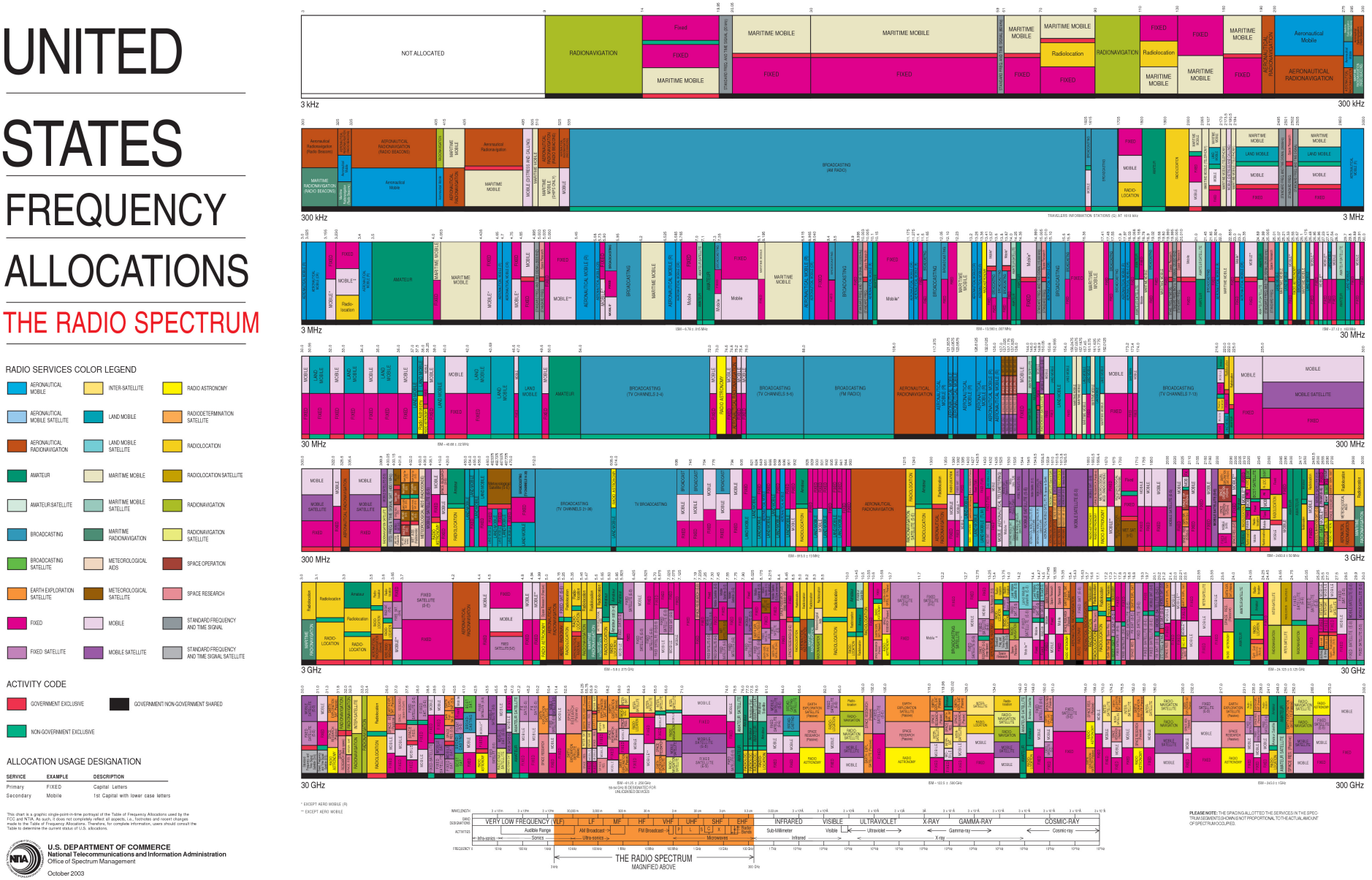

Figure 1.1: United States Frequency Allocations - The Radio Spectrum [15]

Researchers have employed many different techniques to create reconfigurable antennas able to change frequency, polarization, and radiation pattern, ranging from gimbals and phased arrays [45] to varactor diodes [46–49] to semiconductor switches in the form of PIN diodes [50–57] or field effect transistors (FETs) [58, 59] to microelectromechanical switches (MEMS) [60–65]. Table 1.1 lists some of the most commonly used techniques along with the advantages and disadvantages of each. Some sources comparing these techniques are [22–28]. The aim of this thesis is to experimentally advance liquid-metal antenna technology to create reconfigurable antennas. Liquid metal is inherently reconfigurable based on its continuously adaptable flow, thereby giving created antennas the ability to function in many different frequency bands despite using a common antenna volume.

Table 1.1: Reconfigurable Antenna Techniques [22–29]

Technique	Advantage	Disadvantage
1. Antenna on a Mechanical Motor Structure or Gimbals	• Fine step angles	• Heavy and slow compared to phased array • Mechanical moving parts
2. Phased Array Antennas (PAAs) [45]	• Fast scanning time and tracking ability • Multiple beams • No mechanical moving parts • High gain with low side lobes • Reliable - Breakdown of single component leads to degradation of system capabilities but not complete failure	• Expensive • Low bandwidth due to phase shifters • Very complex structure (processor, phase shifters, amplifiers) and feed network • Possible grating lobes with sparse array • Mutual coupling between elements
3. Mechanical Coaxial or Waveguide Switches [66]	• Excellent isolation • Low insertion loss • High power handing capabilities	• Bulky; heavy • Slow switching speed • Discrete reconfigurability
4. RF MEMS [60–65]	• Fast switching speed (1–200 μs) • Small size; low weight • Very low loss (0.05–0.2 dB) • High isolation • Very low power consumption (0.05–0.1 mW) • High Q-factor • High linearity • Monolithic integration • High bandwidth	• Discrete tuning capabilities • Low power handing capabilities (200–500 mW) • Difficult to interact with once fabricated • Lower reliability • Packaging must be considered • Bias lines can interfere with radiation pattern • High bias voltage (20–100 V)
5. RF FET [58, 59]	• Fast switching speed • Small size; low weight • Decent loss (higher than mechanical switch) • Decent DC power consumption (higher than mechanical switch) • Good isolation (lower than mechanical switch) • Some GaAs can be driven with digital signal • Low cost	• Discrete tuning capabilities • Low power handling capabilities • Non-linear • Low bandwidth • May require complex bias circuit

Technique	Advantage	Disadvantage
6. PIN Diode [50–57]	• Very fast switching speed (1–100 ns) • Small size; low weight • Lower bias voltage than varactor diode • Decent bias voltage ($3-5$ V) • Low cost • Low loss (0.3–1.2 dB) • Good isolation (lower than mechanical switch)	• Bias lines can interfere with radiation pattern • Possibly complex bias circuit • DC electric source necessary • Discrete adaptability • Low power handling capabilities • Power consumption (5–100 mW) • Non-linear • Low bandwidth
7. Varactor Diode [46–49]	• Continuous tuning • Fast tuning and switching • Easy to integrate • Low DC power consumption	• Moderately high bias voltage (>25 V) • Bias lines can interfere with radiation pattern • Frequency tunability dependent on variable capacitor span • Moderate isolation loss • May require complex biasing network
8. Photoconducting Switches [67, 68]	• Thermal and electric isolation from antenna and control circuit • Electromechanically transparent • High RF circuit isolation • Very fast switching speed (3–9 μs) • Decent power consumption (0–50 mW) • Low loss (0.5–1.5 dB) • Linear - no harmonics or intermodulation distortion • No RF bias lines	• Discrete switching mechanism • Need optical source - complex activation mechanism • Lossy
9. Shape Memory Polymer [69]	• Depending on polymer: no bias lines needed • Lightweight	• Depending on polymer: Temperature dependent -> external heat or cooling source needed • Slower switching speed
10. Liquid Crystals (LC) [70]	• Low bias voltage (<10 V) • Favorable at high frequencies (>30 GHz) due to loss tangent	• Low efficiency • High losses in LC material

Technique	Advantage	Disadvantage
11. Liquid Metals	• Continuous adaptability • Low weight • High adaptability • Multiple antenna option in same volume without mutual coupling • No RF bias lines	• Slow switching speed • Need for pumping mechanism • Durability (must be in liquid sealed container) • Temperature dependent • Oxidation layer for gallium alloys • Lower conductivity • Can't be used upside down unless in closed system

1.1 Motivation

Conventional electronic antennas are generally built from rigid materials such as: copper, aluminum, or gold. Once fabricated, these rigid structures are difficult to modify when they are implemented in the field. Utilizing liquid metal instead of a rigid material allows the user new design options and the ability to physically change their antenna in real time. It was decided from the background literature research that this reconfigurability is best achieved using liquid metals and will lead to improvements in creating wearable antennas, such as in bullet proof vests or wearable electronics, adaptable multiband cell phones, GNSS/GPS anti-jam/null-steering antennas, smart antennas that react to their environment, and many more applications.

As shown by many universities, liquid metals can be used to create stretchable/flexible [36, 71–73], self-healing [32, 73, 74] or wearable [75] antennas. These properties would be very useful in wearable electronics due to the antenna forming any shape necessary without breaking electrical connection. It is difficult to use solid metal antennas for this application because solid metals have a lower malleability and are prone to fatigue.

Also, liquid-metal antenna technology could be utilized to create a disaster

recovery antenna. In situations where there is a disaster, large amounts of equipment must be hauled into the disaster zone to assist with the rescue and rebuilding efforts. Among this large amount of equipment, antennas must be brought in to re-establish communications in the area. Depending on the situational needs, this could require a wide variety of frequencies, meaning a large variety of different antennas. Reconfigurable antennas could be used to minimize the number of antennas needed in these zones since they can be used at many different frequencies depending on the shape in which they are configured.

Reconfigurable antennas could also be used as smart antennas to react to the electromagnetic environment around them. The ability to change the shape of the antenna gives the user the capability of changing frequency, polarization, or beam direction in real-time. This means if there is an unwanted signal in a certain direction, the antenna could react and steer a null of the radiation pattern in that direction to effectively notch out the undesired signal.

The L-band was chosen in particular due to the smaller resonant size of the antennas and the fact that the established Global Navigation Satellite System (GNSS) runs in this frequency band. Applying the reconfigurable antennas to the GNSS system, specifically GPS, results in a wide range of possible benefits. This type of antenna could be used to create an anti-jam GPS antenna by creating a

null that blocks the interfering signal. This technique is one of the most common methods for removing unwanted or interfering signals from the receiver.

The broad use of GPS in both commercial and military applications makes the L-band a very attractive frequency band for liquid-metal antenna applications. GPS satellites use circularly polarized antennas (usually right hand circular); if the antenna was linearly polarized, it would be constantly changing polarization with respect to the ground station because of the constant motion of the satellite. Therefore, to efficiently receive GPS signals, a receiver must use a right hand circularly polarized antenna or a linear antenna with the understanding that a 3 dB loss is expected. It is common for a cheap GPS receiver to use a linearly polarized patch antenna with this accepted polarization mismatch. A liquid-metal antenna has the ability to change polarizations if necessary as long as the antenna is designed correctly, meaning these polarization mismatch losses can be minimized. Also, using antennas made from liquid metals can give a system the ability to react to its environment by beam steering the radiation pattern to track GPS satellites while also counteracting nearby unwanted signals by making physical adjustments to the antenna. Figure 1.2 displays a high level overview of a situation where this ability would be useful.

In the future, this technology may also be applied to phased array-fed reflector

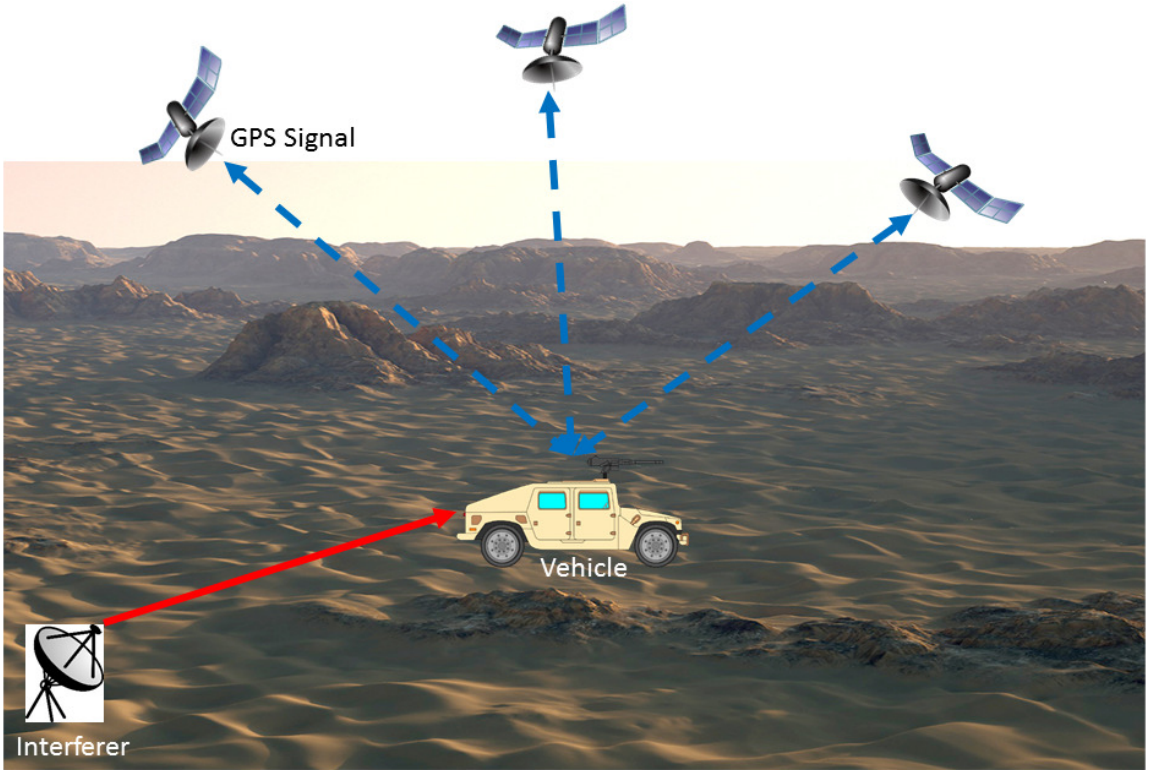

Figure 1.2: High-Level Operational Concept Graphic

(PAFR) antennas to reduce cost and overall system power consumption. By utilizing liquid metals in the phased array, fewer phase shifters are needed to perform the beam shaping, this could be achieved by adjusting the physical dimensions of the nearby antennas. This technology could lead to requiring fewer analog to digital (A/D) converters and therefore fewer transmit/receive (T/R) modules to run the system. By removing this hardware from the system, the overall cost of the system could be reduced.

1.2 Contributions

This work expands upon previous research done in creating reconfigurable antennas utilizing a liquid metal alloy. Chapter 2 introduces a background on different types of metals that are liquid at, or near, room temperature. This chapter also describes some of the material properties of the gallium-indium alloy chosen. Last, some experimental material testing is presented.

Chapter 3 describes three mechanical and electrical feeds for monopole antennas that allow for the easiest liquid metal injection/retraction without sacrificing the performance of the antenna. These three feeds were analyzed for their ease of use in injecting the liquid metal, as well as maintaining an acceptable return loss and outputting a decent gain over a range of frequencies. One of these feed methods had previously been used in liquid-monopole antennas and while the other two methods had not previously been studied. Simulations of each of the antenna feeds were done in FEKO and then compared to experimental results collected from prototype antennas that were built. Last, a prototype Wheeler Cap [6] was built to calculate the radiation efficiency of each antenna.

Chapter 4 introduces a 2D parasitic monopole array in which the user has the ability to change frequency and steer the main beam and nulls of the antenna. A

linear array had previously been researched; this chapter expands upon that work to create a two-dimensional array. This antenna design is based on the working principles of a Yagi-Uda antenna in which parasitic elements are used as either directors or reflectors for the energy. Since these parasitic elements are made from liquid metal, this gives the user the ability to change a parasitic element from a director to a reflector or get rid of it completely depending on the situation, but the spacing between elements must be kept constant. This ability means the user has much higher control over the antenna radiation pattern than its solid metal counterpart. Simulations were run in FEKO for both a four-element and a 16-element parasitic monopole array. For the four-element array, the simulations were compared to the experimental results of a built prototype.

Chapter 5 outlines the basis of the dual helix antenna which allows the user to not only change frequencies but also change polarizations. This type of antenna has not been previously used in this manner to create the desired reconfigurability. In this antenna, the user can choose which helix channel gets injected with liquid metal with each channel having a different circumference (change of frequency) or direction of rotation (change of polarization). A prototype dual helix was built having an inner helix which is RHC and close to GPS L1 frequency and an outer helix which is LHC and is close to GPS L2 and L5 frequencies. Simulations were performed in FEKO

to evaluate the performance of the prototype helix. Coupling between the two helix antennas was also tested to see if multiple helix antennas could be used at the same time in such close proximity.

Chapter 6 proposes an array consisting of both a parasitic monopole array and dual helix antennas that can be 3D printed. This antenna array will be modular, allowing the user the ability to decide which piece of the antenna is needed for each situation. This creates a multi-use antenna within a compact volume. The use of additive manufacturing to crate the structure for the liquid-metal antenna has not been previously researched.

Chapter 7 summarizes possible future work to be done in this field. In this chapter, other feed methods for the monopole are presented along with other antenna designs that could benefit from using liquid metal. Also, a reservoir and pump system is described for injecting or retracting the liquid metal from the antenna without the need of a syringe. Other areas of research are also suggested on how to improve upon utilizing liquid metals in antennas. Last, more research needs to be done before this technology is prepared for testing within a system, such as improving the valve system along with the pumps used.

Chapter 8 provides final conclusions.

1.2.1 Publications

Work performed as part of this thesis also contributed to five peer-reviewed publications (two presented and three pending decisions) as listed below.

Thews, J. T.; Michaels, A. J.; Davis, W. A., "Design and Analysis of Feed Techniques for Reconfigurable Liquid-Metal Monopole Antennas," *National Radio Science Meeting, 2017*. January 2017. Boulder, CO.

Thews, J. T.; Michaels, A. J., "Analysis of Parasitic Effects of Sodium Hydroxide (NaOH) Electrolyte on Liquid-Metal Monopole Antennas," *National Radio Science Meeting, 2017*. January 2017. Boulder, CO.

Thews, J. T.; O'Donnell, A.; Michaels, A. J., "Design and Analysis of Two-Dimensional Parasitic Liquid Metal Monopole Array," *Military Communications Conference 2017*. October 2017. Baltimore, MD. [submitted]

Thews, J. T.; O'Donnell, A.; Michaels, A. J., "Design and Analysis of Dual Helix Liquid Metal Antenna," *Military Communications Conference 2017*. October 2017. Baltimore, MD. [submitted]

Thews, J. T.; O'Donnell, A.; Michaels, A. J., "Simulation of 3D Printed Antenna Array for Liquid Metal Antenna Applications," *Military Communications Conference 2017*. October 2017. Baltimore, MD. [submitted]

Chapter 2

Liquid-Metal Alloys

This chapter introduces an overview of liquid metals and the properties of the chosen liquid metal used throughout the later chapters.

2.1 Liquid Metal

The most common liquid metal at room temperature is mercury, however this element is very toxic to humans and dense [76, 77], making it highly unfavorable compared to the alternatives. Three other metals that have melting temperatures just above room temperature include cesium (28.5°C), gallium (29.76°C) and rubidium (39.3°C). Cesium and rubidium are not good for antenna applications since they are both explosively reactive with water and air. Another well-known liquid metal is

sodium-potassium alloy (NaK), which is liquid from −12.6°C to 785°C, however it is highly reactive with water and may catch fire when exposed to air [78, 79]. Indium (In) also has a relatively low melting point (156.61°C) and a low toxicity [80, 81] making it useful in creating alloys and solders. Table 2.1 compares the boiling point, freezing point, conductivity, surface tension, density, and bulk viscosity of multiple liquid metals.

Table 2.1: Physical Properties of Liquid Metals [30–44]

	Boiling Point (°C)	Freezing Point (°C)	Electrical Conductivity (σ) (S/m) ($\times 10^6$)	Surface Tension (γ) (N/m)	Density (ρ) (kg/m^3)	Bulk Viscosity ($mPa*s$)	Pros	Cons
EGaIn	2000	15.5	3.4	0.624	6095	1.99	Low toxicity	Oxidation layer
Galinstan (EGaInSn)	> 1300	-19	3.46	0.718	6440	2.4	Low toxicity Low freezing point	Oxidation layer
Mercury (Hg)	356.62	-38.83	1.041	0.47	13530	1.55	Low freezing point	High toxicity
Cesium (Cs)	669	28.4	4.878	0.0394	1843	0.686	Low toxicity Photoemissive	Extremely reactive Pyrophoric
Rubidium (Rb)	688	38.9	7.813	0.0847	1472	0.69	Electropositive	Slightly radioactive Reactive w/ water Reactive w/ air
Sodium Potassium (NaK)	785	-12.6	2.632	0.108	867	1.1	Low freezing point	Reactive w/ water Reactive w/ air

Liquid-metal alloys have been used in many electrical applications such as: frequency tuners [82], absorbers [83], resonators [31, 84], filters [85–91], switches

[92, 93], baluns [94], inkjet printing for flexible electronics [95, 96], and antennas. In terms of antennas, liquid metals have been used to create many different types, including monopole [97–103], patch [71,104–107], inverted F [108], slot [109,110], and cone [72] antennas. One benefit of using liquid metal to create the antenna is that it allows the antenna to be tuned continuously, rather than discretely, by changing the physical length of the radiating element.

2.2 Eutectic Gallium Indium (EGaIn)

Alloys of gallium were chosen due to their low toxicity, low viscosity and high conductivity. It was decided to use EGaIn in this research because it is easier to produce compared to Gallistan without sacrificing performance. A property of metal alloys is the eutectic point, which is the point at which the combined metals have the lowest melting point. For gallium-indium, this point is at 85.8 atomic percentage (at%) gallium and 14.2 at% indium, creating a melting point of 15° Celcius [111], which is lower than the independent melting points of both constituent metals (Ga:29.76°C, In:156.6°C), helping ensure the alloy's viability and stability for use as an antenna at room temperature. Fig. 2.1 shows the binary phase diagram where this optimal ratio is evident. EGaIn has a viscosity of about 2x water [112], making it easy to inject or retract from the channel. This alloy also has a low toxicity

according to the CRC handbook [113], consisting of indium, which is commonly used as solder, and gallium, which has a toxicity on the order of aluminum [114]. Therefore general handling procedure of the alloy is relatively benign, barring ingestion.[1]

The atomic structure of liquid Ga, EGaIn and EGaInSn was analyzed by the Department of Mechanical Engineering at University of Michigan. They found that due to the larger atomic volume of the indium and tin, displacing extra gallium atoms with either of those will gradually shift the first peak position of the pair coorelation function ($g(r)$) to the right and increases the atomic volume [115]. They also analyzed the constant charge density contours for EGaInSn at 310 K. It was found that the electron distribution near the indium and tin atoms is similar to that of mercury, where the low-energy orbital electrons are strongly bonded to the atom, causing a low melting temperature [115]. This explains the low melting temperature of EGaIn and EGaInSn compared to Ga (Table 2.1). Some previous work also showed that as the temperature of the liquid metal increases, the conductivity decreases [115–117]. This ranges from about $3.3 * 10^6$ S/m at 291 K to $2.02 * 10^6$ S/m at 723 K for Galinstan [116]. This means that if an antenna is operated at near the melting

[1]To begin these experiments, material safety data sheets (MSDS) for gallium, indium and one molar sodium hydroxide were found. To help ensure experimental safety, these materials were handled in a chemical laboratory; a standard operating procedure document was written and approved and facility employees gave an orientation of the chemical lab. Personal protection in the form of latex gloves and safety goggles were used when handing the alloy as an added safety measure.

point of EGaIn (15°), the liquid metal will have a higher conductivity. It should be considered that EGaIn expands by 3.2 volume % when it solidifies [112], therefore the structure containing the liquid metal would need to be designed to handle this expansion.

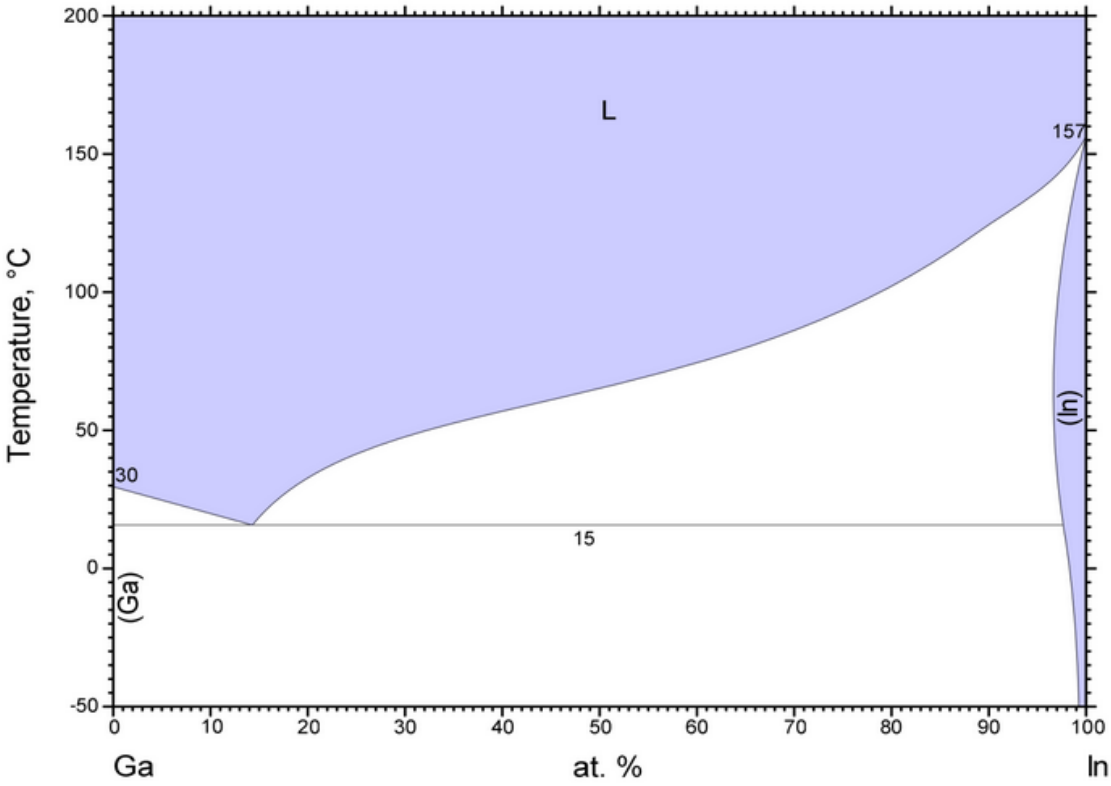

Figure 2.1: Binary Phase Diagram of Gallium and Indium [16,17]

EGaIn has an electrical conductivity of $3.4 * 10^6$ S/m at room temperature [100]. For comparison, solid copper has an electrical conductivity of $5.96 * 10^7$ S/m, and mercury has an electrical conductivity of $1 * 10^6$ S/m at 25°C. A material with a lower

electrical conductivity means that it has a higher electrical resistivity. This means the antenna made of EGaIn will have higher losses due to this higher resistivity than an antenna made from copper.

EGaIn is mechanically stable in microchannels because of the surface oxide skin that forms. This oxide layer has a chemical composition of Ga_2O_3 [18, 118]. In our application, the oxidation was a hinderance, therefore, a one molar solution of sodium hydroxide (NaOH) was used to counteract the effect of the oxidation layer that forms where the liquid metal contacts oxygen. This oxidation layer forms almost instantly, but is a passivating layer [18, 118], meaning the growth is essentially complete at a thickness of about 5Å[118]. This oxidation layer can be broken with minimal agitation (Fig. 2.2), however reforms quickly. As can be seen from Fig. 2.2, the actual alloy is a shiny silver color rather than a grey. Due to the oxygen that was present in the tubing prior to the injection of the liquid metal, an oxidation layer forms the moment the liquid metal comes into contact with oxygen. This oxidation layer sticks to the inside of the tubing that was used, making it difficult to determine the height of the antenna if any liquid metal was retracted. The NaOH counters this problem efficiently with a layer as small as one millimeter or less. NaOH, being an electrolyte, has a conductivity of about 181 mS/cm (18.1 S/m) in a one molar solution [119,120] (Eqn. 2.1), which is higher than that of seawater ($\approx$ 50 mS/cm) [1,119,120],

assuming the seawater solution is 3.5% weight percent composed of sodium chloride [121]. This is not significant compared to the conductivity of EGaIn, however, there can be minor performance effects of the antenna based on how much NaOH is on top of the EGaIn[2](see Chapter 3). NaOH was used to remove this skin layer because, according to the Pourbaix diagram (Fig. 2.3), the skin layer can be removed at pH < 3 or pH > 11.5 [18], where 1M NaOH has a pH of 14 [122, 123]. According to Dr. Dickey [112], this oxidation layer can be removed by a pH < 3 or pH > 10. Gallium wetting on glass can be prevented with a cover of distilled-water or paraffin [114]. Distilled water can also be used to prevent GaIn from wetting of pyrex by the combination of the surface oxide to form gelatinous $Ga_2O_3(H_2O)_n$ [114].

$$\begin{aligned} 1 \text{ mol NaOH} &= \frac{40\text{g NaOH}}{1 \text{ mol NaOH}} = 40\text{g NaOH} \\ 1\text{M NaOH} &= \frac{1 \text{ mol NaOH}}{1\text{L } H_2O} = \frac{40\text{g NaOH}}{1000\text{g } H_2O} = .04 \text{ NaOH} = 4\text{wt\% NaOH} \end{aligned} \tag{2.1}$$

The skin depth is calculated using the equation Eqn. 2.2 where ρ is the electrical resistivity and μ is the magnetic permeability. Using an electrical conductivity of $3.4 * 10^6$ S/m, the calculated skin depth is 8.6 μm at 1 GHz and 6.1 μm at 2 GHz. The electrical conductivity (σ) of a material is equal to the reciprocal of the electrical

[2]The boundary between the EGaIn and the NaOH may have unknown effects on the performance of the antenna. In this study, it is assumed the boundary has negligible effect. Further studies are needed to verify this boundary does not impact the overall performance.

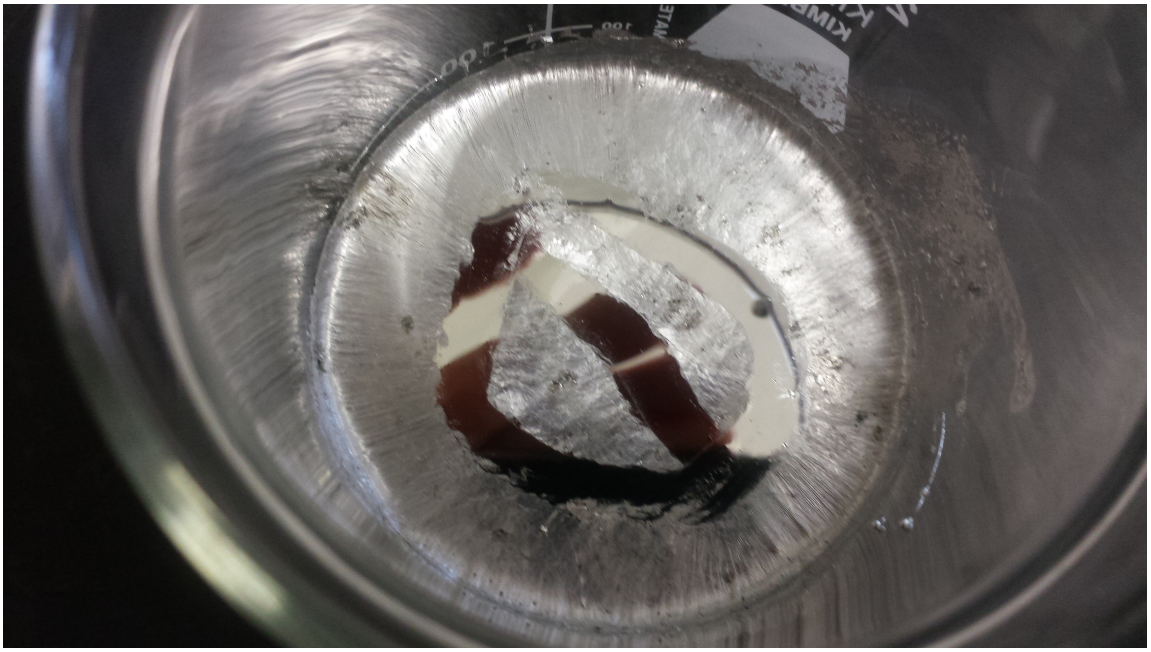

Figure 2.2: Broken Oxidation Layer from Agitation

resistivity (ρ) (Eqn. 2.3). With the resistivity, we can also find the resistance per unit length of the liquid metal. At high frequencies, the resistance per unit length is given by Eqn. 2.4, giving 5.4 $\frac{\Omega}{m}$ at 1 GHz and 7.7 $\frac{\Omega}{m}$ at 2 GHz.

$$\delta = \sqrt{\frac{\rho}{2 * \pi * f * \mu}} \tag{2.2}$$

$$\rho = \frac{1}{\sigma} \tag{2.3}$$

$$R_{unit\_length} = \frac{R_s}{2\pi r} \tag{2.4}$$

$$R_s = \sqrt{\frac{\omega\mu}{2\sigma}} \tag{2.5}$$

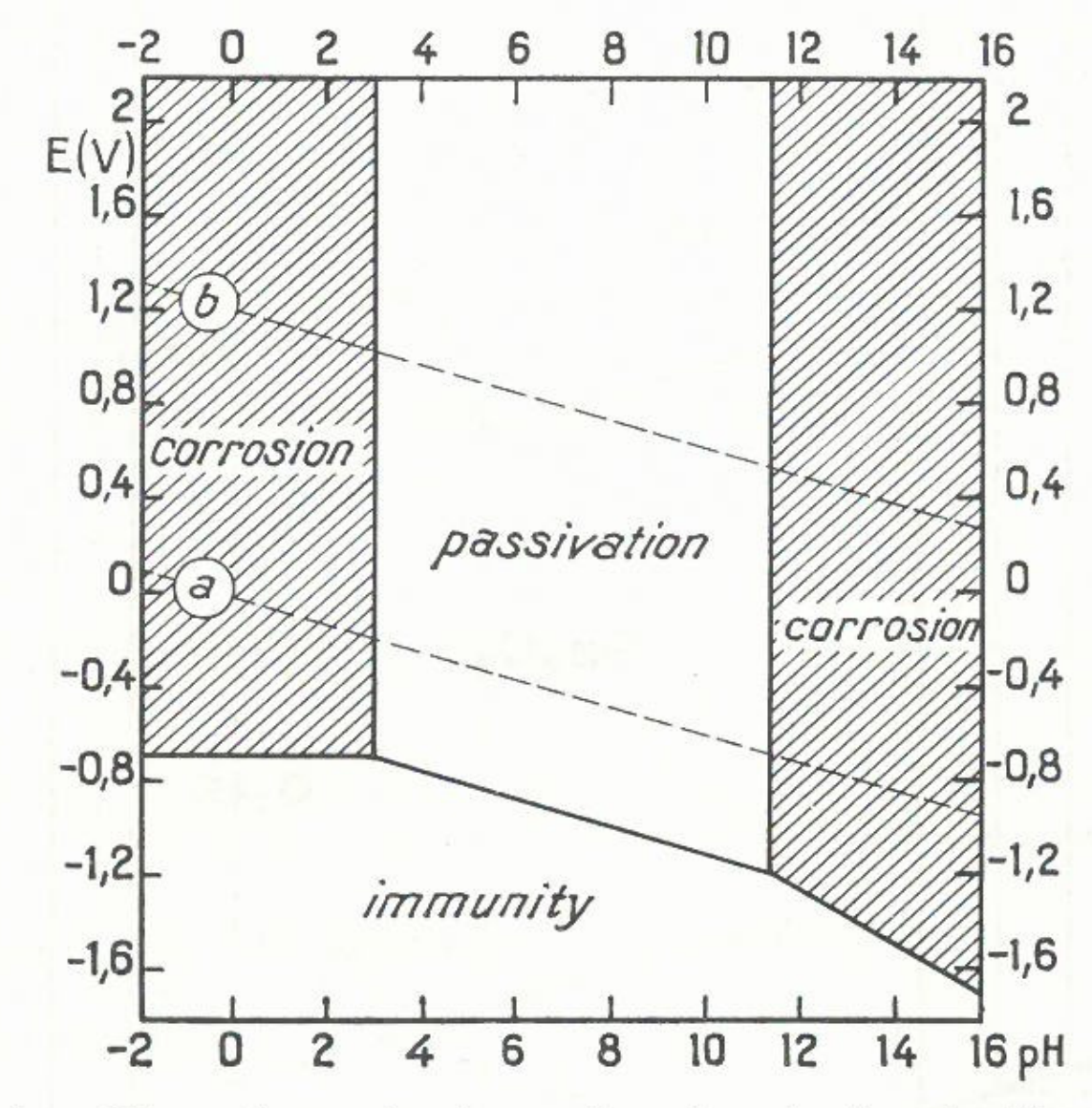

Figure 2.3: Pourbaix Diagram - Theoretical Conditions of Corrosion, Immunity and Passivation of Gallium, at 25°C, Assuming Passivation by a Film of $\alpha - Ga_2O_3$ [18]

2.2.1 EGaIn Experiments

As part of the experimental setup, some corrosive testing with the EGaIn was performed on the materials that would be used for the antennas. These materials included wire (copper, gold, and aluminum), latex gloves, nylon, and the tubing (polyethylene, ethylene-vinyl acetate and silicone). The testing was done by placing a drop of EGaIn onto the object to be tested, then agitating the top layer of the EGaIn with the object to remove the oxidation layer and allow the object under test to come into contact with the alloy (Fig. 2.4). It was discovered that the EGaIn reacted negatively with aluminum wiring, corroding it into a flaked powder overnight. In Fig. 2.5a, it can be seen that the aluminum wire is beginning to react with the EGaIn; In Fig. 2.5b, it can be seen that the aluminum wire has fully corroded and is no longer usable. This is a well-known reaction caused by gallium attacking the grain boundary of aluminum [17]. There is no evidence of adverse effects on the other materials after $\approx$ 1.5 years but it was beyond the scope of this study to perform metallurgy to analyze grain boundary attacks.

Testing was also done on how the EGaIn and NaOH interacts if the liquid metal was injected into the tubing above the NaOH. From this experiment, it was seen that the NaOH and EGaIn perform similar to oil and water. In the "oil-water" experiment, the water ions are more attracted to their own molecules than those of

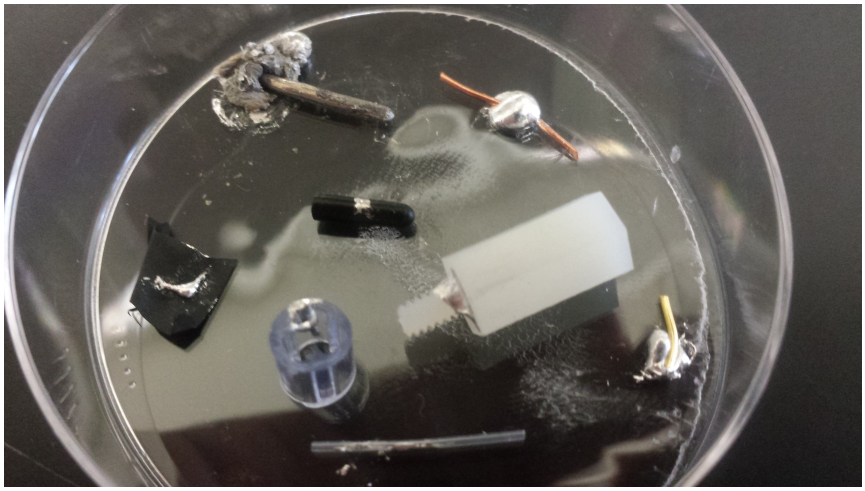

Figure 2.4: Corrosion Testing of Multiple Materials in Contact with EGaIn

(a) Aluminum Wire Beginning to Corrode

(b) Aluminum Wire Fully Corroded

Figure 2.5: Aluminum Wire Corrosive Testing

the oil and vice versa, therefore the two chemicals won't mix to create a solution. Instead, the oil floats above the water because it has a lower density (Fig. 2.6). The NaOH and EGaIn have a similar relationship in that the NaOH and EGaIn don't chemically interact and the NaOH floats above the EGaIn. First, the liquid metal was injected into the tubing using a syringe and needle. The liquid metal formed small spheres (Figs. 2.7a-2.7b) that easily pierced the NaOH barrier and then reformed with the liquid metal in the tubing after a short period of time ($\approx$ 1 s). Next, a more significant volume of the liquid metal was injected into the top of the tubing, with the tubing pinched in the middle to prevent flow (Fig. 2.7c). Once the tube was straightened, the metal fell easily, pausing shortly at the NaOH barrier, and then the entire mass continued to move through the NaOH easily before reforming with the metal already down there (Fig 2.7c). The liquid metal did leave a streak at the top of the tube, though it didn't coat the tube; so if there was any consideration of injecting metal from the top of the antenna and having it fall through the NaOH, that might be problematic. It is assumed the streak is comprised of Ga_2O3, which may have parasitic effects on the performance of the antenna of a layer remains inside the tubing above the antenna.

Figure 2.6: Classic Interaction Between Oil (Top Layer) and Water (Bottom Layer)

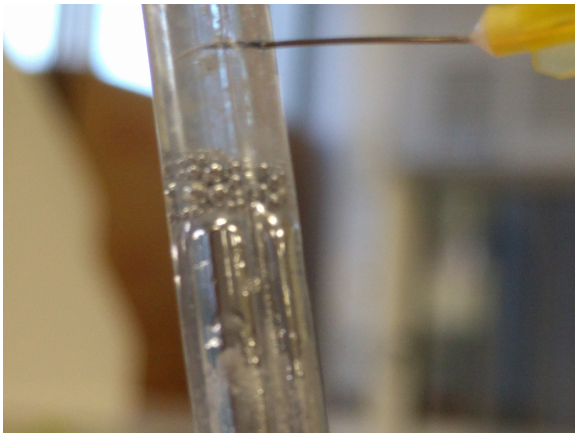

(a) Spheres of EGaIn Injected with Syringe and Needle

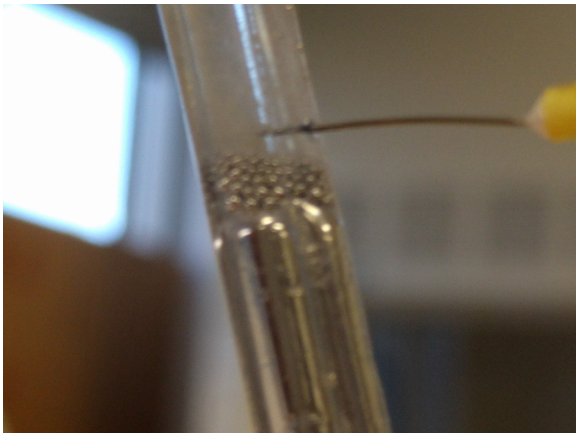

(b) EGaIn Spheres Recombine with EGaIn Mass

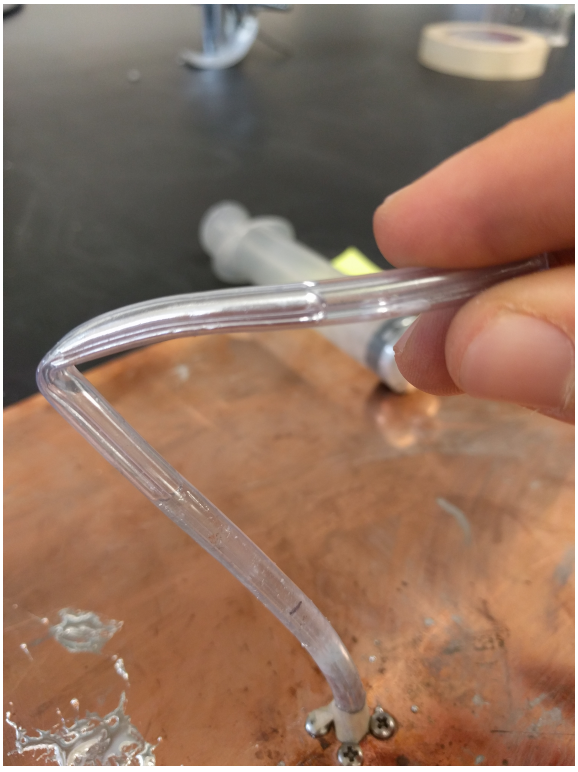

(c) Mass of EGaIn Collected in Tube Before Dropping into NaOH

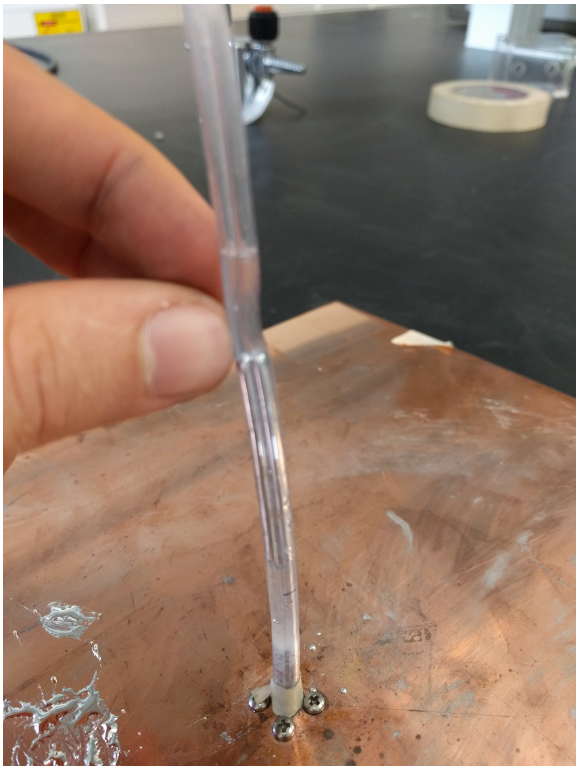

(d) Mass of EGaIn Passing Through the NaOH

Figure 2.7: EGaIn Injection Testing

2.2.2 Conclusions

This section shows eutectic gallium indium is a viable alternative to using mercury as a liquid metal because of the low melting point and low toxicity. The eutectic point is at 14.2 at% In (21.4 wt% In) and 85.8 at% Ga (78.6 wt% Ga).

One of the disadvantages of working with a gallium alloy is the oxidation layer that forms almost instantaneously when it comes into contact with oxygen. This oxidation layer can be corroded with a solution of pH < 3 or pH > 10. The NaOH solution used to corrode the oxidation layer may cause problems when creating a liquid-metal antenna as shown in Chapter 3. The liquid metal has a conductivity of $3.4 * 10^6$ S/m, meaning it has a lower conductivity than copper, but is still high enough for the application. Using this liquid metal in an antenna will have higher Ohmic losses than one made from copper, but these losses are outweighed by the reconfigurable benefits. In our initial testing of the EGaIn, it became clear the liquid metal reacted negatively with aluminum, rendering it unusable. Copper and gold wire appear unaffected by direct contact with the EGaIn, but further, more thorough, studies are needed. This is important because the SubMiniature version A (SMA) connectors used were gold plated. Depending on the application, the user may wish to add tin to the alloy, which creates a much lower melting point at about $-19°$C [33] (Fig. 2.8).

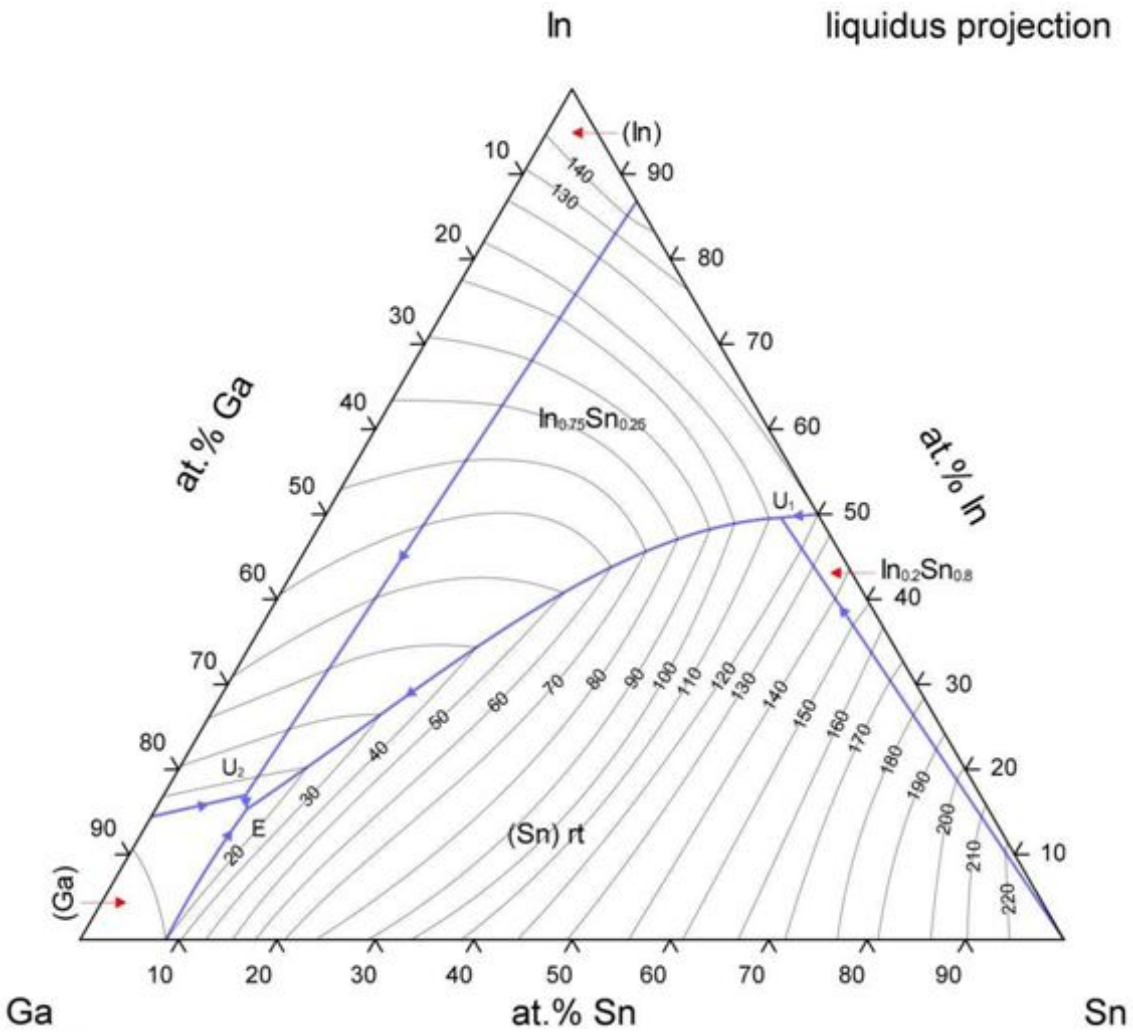

Figure 2.8: Ternary Phase Diagram of Gallium, Indium and Tin [19]

Chapter 3

Liquid-Metal Monopole Antenna - Feed Methods

Liquid-metal antennas are a relatively new technology and are being studied because of their inherent reconfigurable nature. While previous researchers have studied different types of antennas, the electrical feed methods for these antennas have not yet been studied extensively. This chapter will look into different electrical and mechanical feeds for a monopole antenna while still retaining the ability to reconfigure the height of the antenna and maintain an acceptable performance. A prototype liquid-metal monopole antenna was built and three different electrical feed methods were analyzed, comparing the results to simulation produced in the electromagnetic modeling software. Each of the different feed methods was mechanically feasible,

however one in particular would be easiest to scale to a more complex array that will utilize a common liquid metal filled reservoir between them. Along with these feed methods, the parasitic effect of the NaOH that is placed on top of the liquid metal is also discussed.

3.1 Introduction

Researchers at North Carolina State University and the University of Hawaii at Manoa were pioneers in liquid-metal antenna technology. Researchers at NC State have created a pressure responsive liquid-metal dipole and an electrochemically controlled monopole [100]. Researchers at the University of Hawaii at Manoa showed it is possible to use liquid metal to tune the operational frequency of a monopole antenna over an impressive two octaves by adjusting its length while maintaining a consistant gain [99]. Researchers at University of Hawaii also created a linear Yagi-Uda antenna with an array of monopoles and showed that it is possible to beam steer and frequency tune the antenna by adjusting the heights of the liquid metal in each element, however they needed to manually inject and retract the metal with a syringe [97, 98]. Previously, switches were used to reconfigure Yagi-Uda antennas to achieve the same effect [124, 125]. Both of these universities used an electrical feed at the base of the antenna, right at the ground plane.

A framework describing the liquid antenna feed methods under consideration is provided in Section 3.2. Next, a detailed model of the feeds used for the liquid-metal antenna are specified in Section 3.3. The feed types that will be discussed are a bottom feed, a bottom feed with an injection stub for liquid metal, and an offset feed that is below the ground plane. Then, simulation versus experimental results will be compared in Section 3.4. The simulations were limited in some ways by the ability of the software in mapping liquids to antenna elements. Lastly, future work with other feed technique ideas and where to progress from here will be discussed in Chapter 7.

3.2 Experimental Framework

The L-Band ($1-2$ GHz) was the frequency of interest because of the relatively small size of the antennas and the availability of GNSS at this frequency. The tubing used in the antenna was $\frac{3}{16}$ inch (≈ 4.76 mm) inner diameter polyethylene oxygen connecting tubing [126]. The inner diameter of this oxygen tubing is considered the diameter of the antenna, which affects the s_{11} parameter of the monopole as seen in Fig. 3.1 and also affects the bandwidth of the antenna [13]. Interestingly, this plot also shows that as the wire radius increases, the center frequency changes. Specifically, for the 75 Ω impedance curves, as the radius increased, the center frequency drastically

changed from about 1.54 GHz at 0.5 mm to about 1.44 GHz at 2.4 mm. This effect is also seen in the upcoming prototype antennas, forcing a liquid metal height that is slightly different from exactly $\frac{\lambda}{4}$. This effect is due to the resonant length of the antenna becoming shorter as the diameter of the antenna increases [13, 127]. The ground plane is a 300 mm by 300 mm copper sheet, which was large enough that a consistent radiation pattern was seen. The SMA connector was connected to the ground plane through four #2 screws with nuts and washers. The element length was determined by injecting or retracting metal by the use of a syringe.

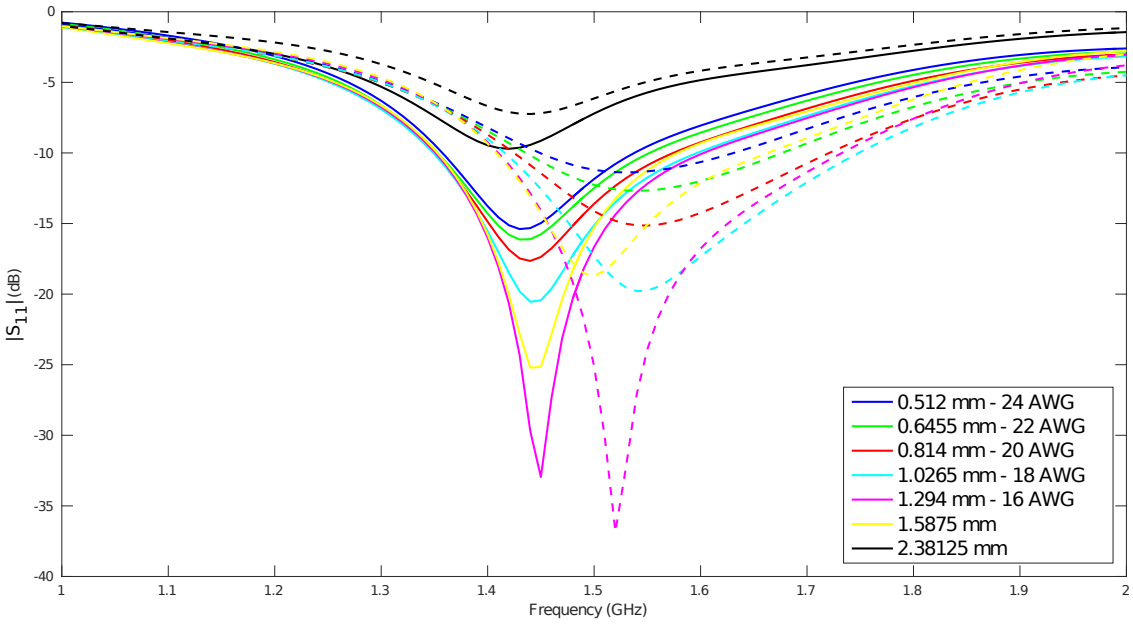

Figure 3.1: Comparison of Different Wire Radii and Different Characteristic Impedances (50Ω - Solid Lines; 75Ω - Dashed Lines)

A monopole antenna is generally $\frac{1}{4}$ wavelength mounted above some sort of conductive ground plane. This means that with image theory, the monopole becomes a dipole of two times the monopole length. Therefore the radiation pattern of the monopole above the ground plane is known from the pattern of the dipole (Fig. 3.2a). The impedance of a quarter-wave monopole is half that of a half-wave dipole, meaning it is about 36.5 + j21.25 Ohms. The directivity of the monopole antenna is twice that of a dipole antenna because no radiation occurs below the ground plane. In theory, with an infinite ground plane, the maximum directivity occurs on the same plane as the ground plane (Fig. 3.2a). However, in practice, with a finite sized ground plane, the radiation pattern is skewed upwards while still remaining omni-directional (Fig. 3.2b). A large enough ground plane is required so that the impedance of the monopole is minimally affected. This length should be at least a few wavelengths in size around the monopole. Also, using a square ground plane instead of a circular one can effect parts of the radiation pattern, making the antenna more directional (Fig. 3.2c).

This section will analyze three different feeds for the liquid-metal monopole antenna. The first feed is a bottom-fed monopole (Fig. 3.3a), which is the most common way to feed a monopole. The second feed method also uses a bottom feed, however this monopole has a stub on the side for injecting or retracting the liquid

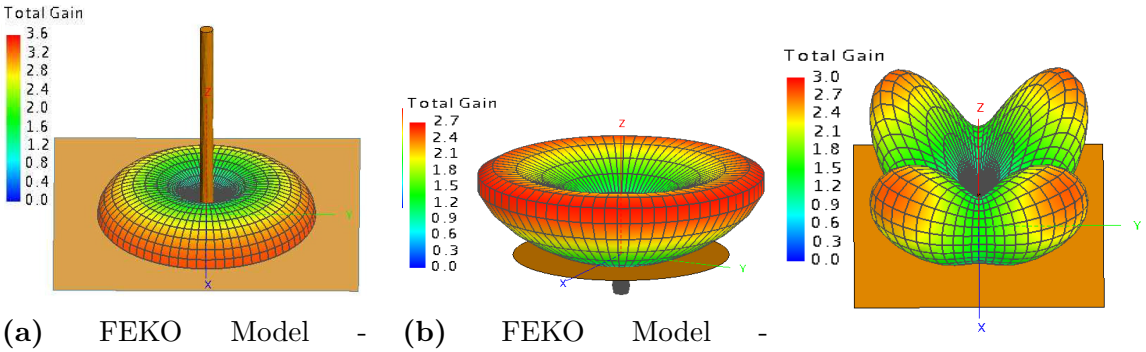

(a) FEKO Model - Radiation Pattern of a Monopole with an Infinite Ground Plane

(b) FEKO Model - Radiation Pattern of a Monopole with an Circular Ground Plane

(c) FEKO Model - Radiation Pattern of a Monopole with an Square Ground Plane

Figure 3.2: FEKO Models - Comparing Radiation Patterns of Different Ground Planes

metal (Fig. 3.3b). The last feed method is an offset feed that is below the ground plane (Fig. 3.3c).

There is about a 1-2 mm error in the measurement of the antenna because the EGaIn creates a meniscus where it contacts the NaOH as seen in Fig. 3.4. This convexity makes it difficult to precisely measure the effective length of the monopole. For all the future measurements in this paper, the antenna was measured to the top of the meniscus.

The simulations were performed in the electromagnetic modeling software FEKO [128]. Recently, a new student license is being offered for free through Altair, with some restrictions on the complexity of the model. Some of the limitations

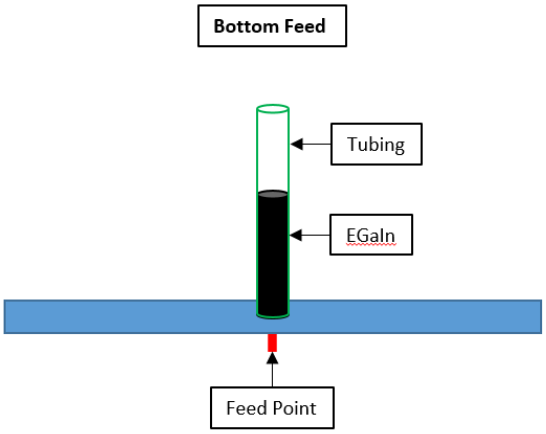

(a) Bottom-Fed Monopole Antenna

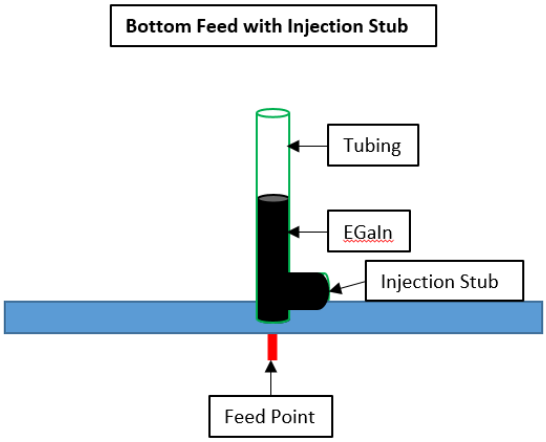

(b) Bottom-Fed Monopole Antenna with Injection Stub

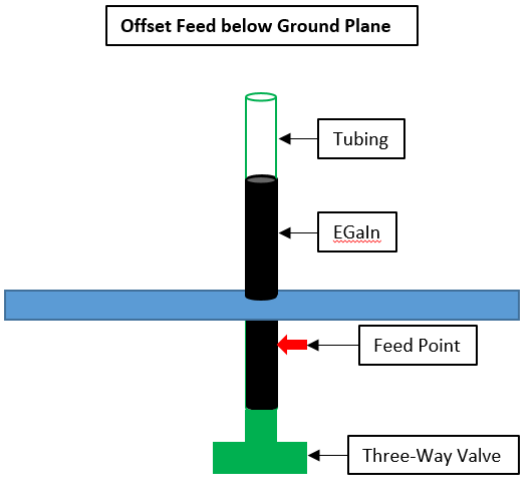

(c) Below Ground Offset-Fed Monopole Antenna

Figure 3.3: Antenna Models - Simple Diagram

Figure 3.4: Meniscus at EGaIn/NaOH Boundary

that hindered the simulations were number of mesh triangles of $25,000$, number of frequency values of 20, main memory allocated by kernel of 1 GByte, optimization degrees of freedom of 3 and optimization steps of 50. The solver uses a combination of complex computation methods, such as method of moments and finite element method, to solve for different sections of the model. FEKO works by first creating a mesh around the model and then using a combination of different solvers to account for each part of the model. The first step in designing the feed methods was building each of the feeds as FEKO models. Fig. 3.5 shows the model of the offset-fed monopole antenna and also shows the meshing of triangles on the model.

The ground plane is colored black because of the point of view, not because it is a different material.

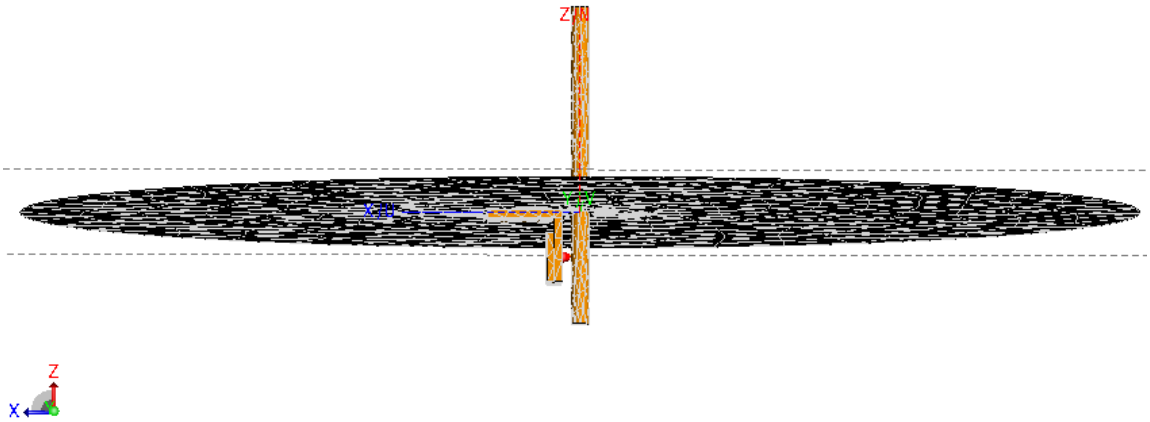

Figure 3.5: FEKO Model of Offset-Fed Antenna

3.3 Detailed Model

There is almost no practical lower bound to the diameter of the antenna. As shown by NC State, EGaIn has a bulk viscocity of $1.99 * 10^{-3}$ Pa $\cdot$ s and can flow through a channel 20 μm thin if enough pressure is applied [32]. This means the liquid metal will easily flow through the valves and T-junctions in the setup and also means the diameter of the tubing could be made much smaller without having to worry about the fluid flow.

3.3.1 Bottom Feed

This feed type is the typical feed for a monopole antenna. The downside of this design is that to inject or retract liquid metal from the antenna, it was necessary to pierce the tube with a needle and manually inject/retract the liquid metal (Fig. 3.6a). The liquid metal will not flow out of the hole created by the needle because of the oxidation layer that forms but, over time, if the tube is pierced too many times in the same location, the tubing will unacceptably degrade. Also, a needle gauge of 30 AWG was used to inject the liquid metal into the tubing. While this size needle was fairly easy to push the liquid metal, this gauge of needle bent and broke quickly when poking it into the tubing. A larger gauge needle would most likely have been more durable when piercing the polyethylene tubing, however a larger needle would also likely create larger holes per puncture, thus quickening the breakdown of the tubing. This makes this design non-optimal for connecting a pump or some type of liquid-metal reservoir. This lack of automation and the breakdown of the tube over time with usage will limit future applications. As stated above, this method of injection, using a needle to inject or retract the metal is the same method the University of Hawaii has been using with their antennas.

3.3.2 Bottom Feed with Injection Stub

This feed type is also the typical feed for a monopole antenna. The difference in this antenna is how the liquid metal is injected into the antenna. In this setup, the syringe can be directly attached into the side stub to inject metal into the antenna without having to pierce the tube. Theoretically, a tube could be attached there, instead of a syringe, which is then connected to a pump to be able to pump the metal directly into the antenna at will. Attached to the stub is a one-way valve with a Luer Lock, which means it only allows fluid to flow in one direction, from the syringe into the antenna. This means that once the liquid metal is injected, it will not drain out the side of the antenna, however this also means that to retract metal from the prototype antenna, it was necessary to pierce the tube with a needle.

There is a practical bound for the smallest length of the antenna because of the nature of the T-junction used. The T-junction, shown in Fig. 3.6b, is white for 24 mm before connecting to the clear tubing. This means that if the liquid metal is below 24 mm, it is not easy, if not impossible, to determine the length of the antenna by sight. Therefore, there is a maximum frequency of 3.1 GHz with this setup. The injection stub that is attached to the side of the antenna is 17 mm in length, which would correspond to a resonant frequency of 4.4 GHz. This stub will actually act as a second monopole, making the antenna dual-band [129], however the length of the

stub put the operating frequency outside the band that was analyzed. Therefore the effects of the stub on the antenna in question are minimized.

The one-way valve is not a permanent solution to this type of feed. The one-way valve used, meant to hold against less dense liquids, slowly leaked the liquid metal over time. This did not happen quickly, so measurements of the antenna could still be taken but over the course of a few hours, the lock would not be able to hold back the liquid metal in the antenna. A Q-tip was used to prevent this leak by stuffing it into the end of the one-way valve. Also, in the future, if a reservoir was attached to the injection stub, a multi-directional valve would need to replace the one-way valve. The multi-directional valve would allow the user to inject the metal into the antenna and retract the metal at will. The reservoir would need to be placed below the ground plane to not affect the performance of the antenna. Also, when the valve is closed, the excess liquid metal in the tube that connects the valve to the reservoir would need to be retracted below the ground plane so the liquid-metal antenna does not couple with the metal in the tube.

3.3.3 Offset Feed below Ground Plane

In this setup, the SMA connector is connected to the ground plane through the use of an L-bracket (Fig. 3.6c). The SMA flange is soldered onto one side of the L-bracket

and then the other side of the L-bracket is connected to the ground plane through a #6 screw. The pin of the SMA connector is piercing the tubing and then glued into place with Krazy Glue. Below the SMA connector, the tubing is attached to a 3-way valve. This valve allows the decision to inject or retract metal depending on which direction the valve is opened. To use the antenna efficiently, the valve needs to be closed off so that the extra metal remaining in the valve does not contact the antenna. In this setup, the SMA pin is located 12 mm below the ground plane and the top of the valve is 18 mm below the SMA pin. So in total, there is 30 mm of extra metal below the ground plane. Fig. 3.6c shows the SMA connector being poked through the tubing below the ground plane and the valve system for injection. Fig. 3.6c also shows the extra metal sitting in the valve system and a small amount inside the syringe waiting for injection.

This method of feeding the monopole antenna makes it very easy to scale to multiple independent eletrical feeds from one [gated] series mechanical fluid feed. Tubing could be used to connect the valves underneath each of the feeds and liquid metal could be run through those tubes. By turning the valves, the user can decide how much metal to inject into each of the antennas to receive the antenna properties desired.

3.4 Simulation and Measured Performance

Fig. 3.7 shows a comparison using FEKO between a bottom-fed monopole antenna made from a perfect electric conductor (PEC) and a bottom-fed monopole antenna made out of a material with the conductivity of EGaIn. Each curve represents a quarter-wave monopole from 1 GHz to 2 GHz in 100 MHz steps. This shows how a material of lower electrical conductivity will have a higher s_{11} parameter due to the higher electrical resistivity. The resolution of the PEC model is lower due to the restrictions placed on the student license of FEKO. It should be noted that the reference impedance for both simulation and experimental results was 50 Ohms.

At first, the measurement tool used for the s_{21} measurements was a Kent Electronics log periodic antenna attached to an Ettus N210 USRP running GNU-Radio. GNU-Radio is a free and open-source toolkit for software defined radio. The N210 USRP was characterized by using a power divider from the signal generator going to the GNU-radio flowgraph and to a Rhode & Schwarz power meter. The realized gain of the log periodic antenna was calculated by taking two Ettus VERT2450 omni-directional vertical antennas, one used for transmitting and the other for receiving, placing the receive antenna next to the log-periodic, which was also used to receive, and documenting the power levels measured. With

these power levels, Friis transmission equation (Eqn. 3.1), was used to calculate the realized gain of the log-periodic antenna over the L-band. This method turned out to be very imprecise because the common receive and transmit antennas were not manufactured to run in this frequency band. A Python script, created by Deirdre Kilcoyne, was modified to streamline the measurement taking process. This script took the maximum of the FFT 1171 times (1.6e6 sampling rate with 4096 FFT size taken over 3 seconds) and averaged them together. This process also turned out to be very imprecise because of the RF front-end of the USRP, with a fluctuation of multiple dB.

$$P_r = P_t G_t G_r \left(\frac{\lambda}{4\pi R}\right)^2$$
$$P_r(dB) = P_t(dBm) + G_t(dB) + G_r(dB) + 20log_{10}\left(\frac{\lambda}{4\pi R}\right) \tag{3.1}$$

To minimize the error of the measurement system, a second measurement setup was created using a Rhode & Schwarz NRP-Z11 universal power sensor to measure the receive power of the log-periodic antenna. The gain of the log-periodic antenna was assumed to be 6 dBi based on its data sheet [130]. The lab in which the measurements were taken was also analyzed to more accurately account for the multipath scattering due to the metal throughout the room. It was discovered that

the effective path loss exponent in the lab was closer to 2.46, rather than 2. This means that the lab the antenna is being tested in has a marginally higher loss due to all the surrounding objects. An accurate measure of the path loss in the room is required to accurately measure the gain of the antenna under test (AUT). The AUT was powered using a Mini Circuits SSG-4000LH signal generator. The AUT was mounted on a cart with the signal generator and network analyzer below it (Fig. 3.8a) and paper with degree increments labeled from a protractor was taped to the ground plane (Fig. 3.8b). A string was attached from the base of the antenna to the SMA connector of the log-periodic antenna to keep a consistent distance in the far field (Eqn. 3.2) of both antennas. The AUT was rotated around and the probe antenna was kept in the same location to try to minimize multi-path error that are introduced from the lab environment (Fig. 3.10). However, even though it is known that the cart is made of plastic, this could still have an effect on the antenna pattern because as the cart is rotated, different parts of the cart are facing the probe antenna. The cart may be reinforced with something other than plastic inside or objects sitting in the bottom of the cart may have an effect on the experimental data. A similar method was used for the elevation measurements with the string (Fig. 3.9a), however the probe antenna needed to be held in place above the AUT (Fig. 3.9b). An improvement that could be made to the test setup would be to build a

wooden boom structure that could be rotated and hold the AUT in place. This would minimize the error that is introduced from a person standing close to the antennas that are being tested. Since this monopole is theoretically vertically polarized, the s_{21} measurements shown below are all taken with the log-periodic antenna positioned vertically (Fig. 3.8a). Horizontal polarization measurements were also taken to verify the liquid-metal antenna was only transmitting vertically polarized wave fronts. All of these horizontal polarization measurements were in the noise floor for the power sensor, meaning the AUT was actually vertically polarized (as expected).

$$R >= \frac{2D^2}{\lambda} \tag{3.2}$$

$$\text{Monopole: } R = \frac{2D^2}{\lambda} = \frac{2\left(\frac{1}{4}\lambda\right)^2}{\lambda} = 2\left(\frac{1}{4}\right)^2\lambda = \frac{1}{8}\lambda$$

$$\text{Log Periodic: } R = \frac{2D^2}{\lambda} = \frac{2\,(140\text{mm})^2}{\lambda}$$

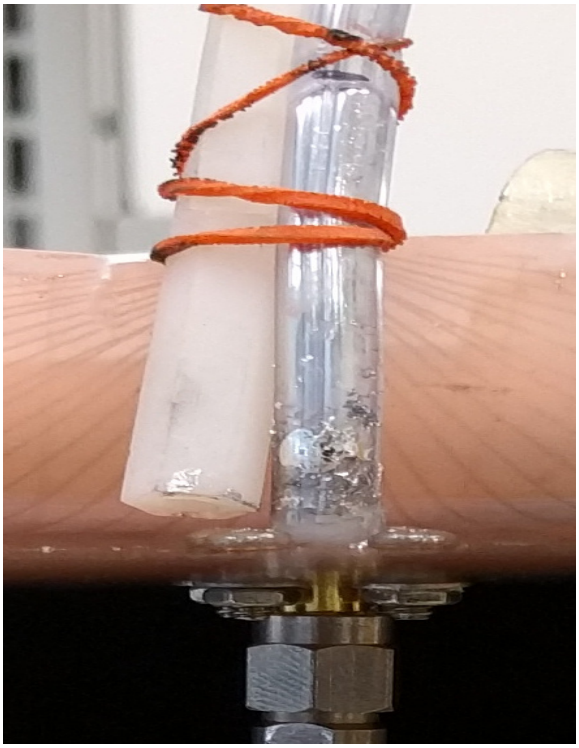

(a) Bottom-Fed Monopole Antenna

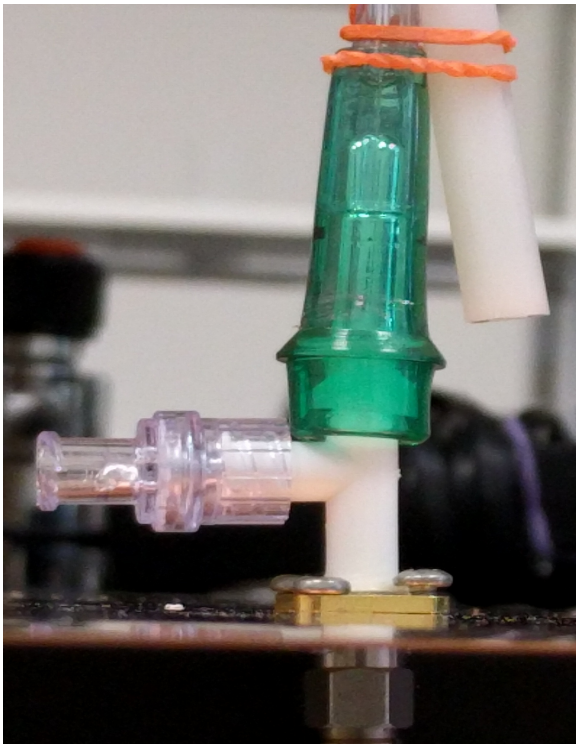

(b) Bottom-Fed Monopole Antenna with Injection Stub

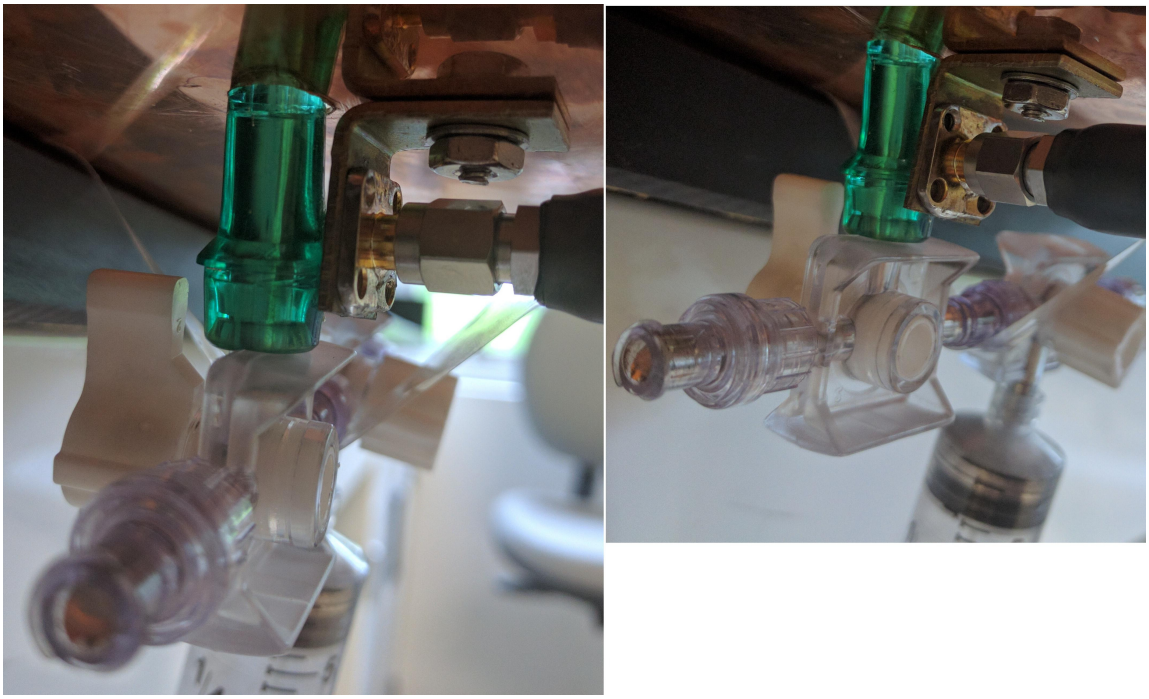

(c) Left: Below Ground Offset-Fed Monopole Antenna Showing SMA Connection; Right: Below Ground Offset-Fed Monopole Antenna Showing Extra Metal Sitting in Valves and Syringe

Figure 3.6: Prototypes of Monopole Feed Methods

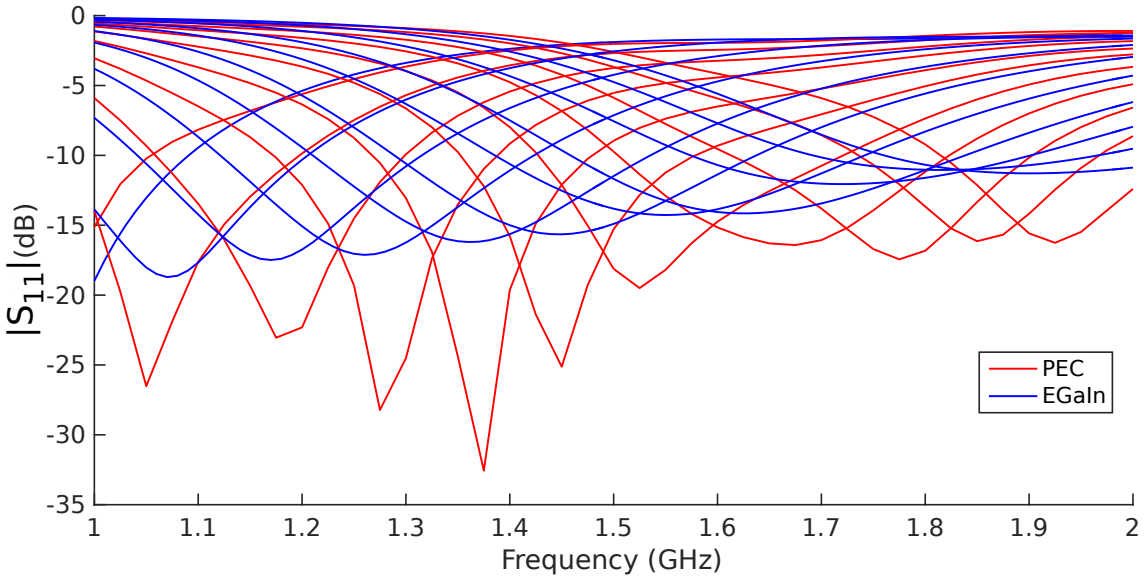

Figure 3.7: FEKO Return Loss Comparison Between PEC (Red) and EGaIn (Blue) for a 1.5875 mm Radius Antenna

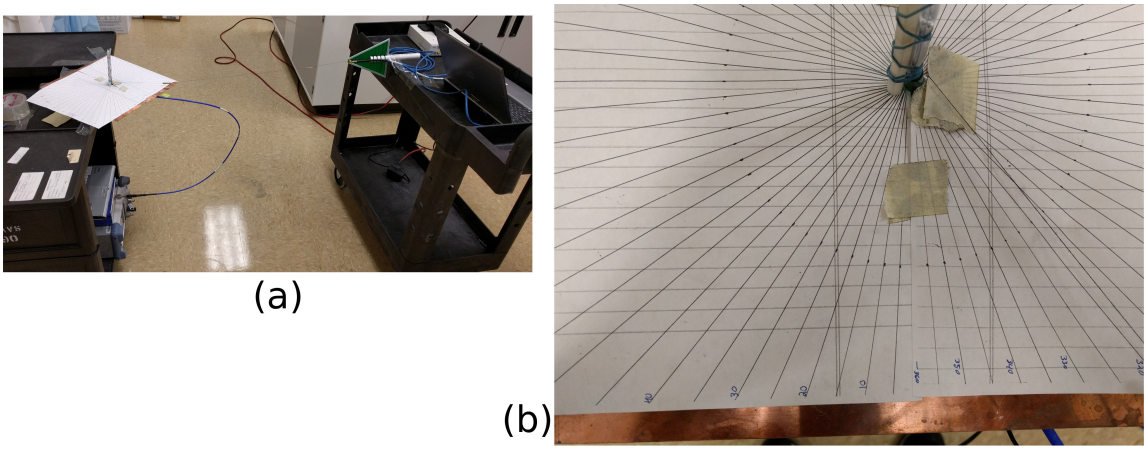

Figure 3.8: (a) Full Setup for Testing the Liquid-Metal Antenna Azimuth Radiation Pattern; (b) Setup for Testing the Liquid-Metal Antenna Azimuth Radiation Pattern

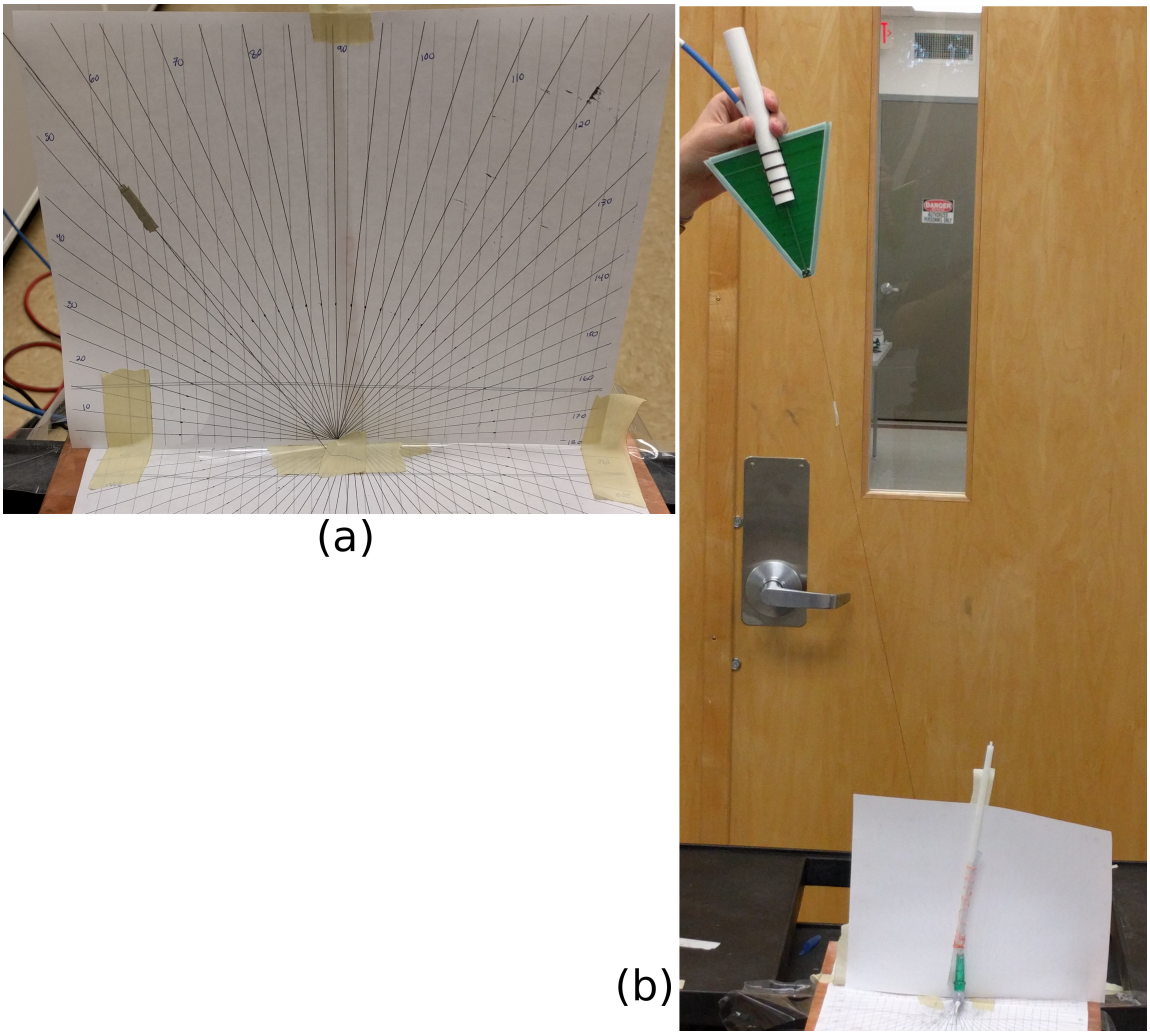

Figure 3.9: (a) Setup for Testing the Liquid-Metal Antenna Elevation Radiation Pattern; (b) Full Setup for Testing the Liquid-Metal Antenna Elevation Radiation Pattern

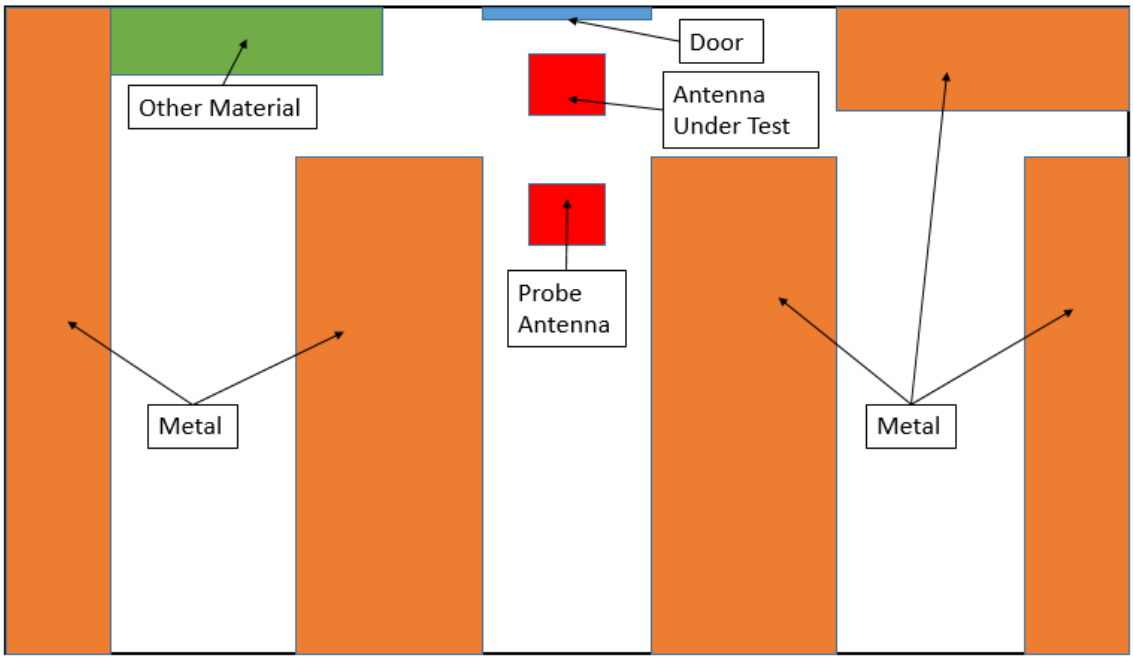

Figure 3.10: Simple Diagram of the Chemical Lab Used to Build and Test the Antennas

For s_{11} measurements, a makeshift vector network analyzer with a bi-directional coupler (Mini-Circuits ZABDC20-252H+) and an Ettus B210 USRP were put together. Analysis of the insertion loss, directivity, and coupling of the bi-directional coupler was done with the network analyzer (Appendix D). The Ettus B210 USRP was characterized in the same way as the N210 USRP and using GNU Radio, the complex impedance, $|s_{11}|$ and VSWR were calculated (Fig. 3.11). This method had a poor resolution (Figs. 3.12a-3.12b) because the user is required to manually adjust the frequency of interest on both the GNU Radio flowgraph and the signal generator before recording the data. It was also determined that the quality of the RF front end was not sufficient for the measurements (Figs. 3.12a-3.12b), therefore, a different measurement method was needed to quickly and accurately measure the return loss of the liquid-metal antenna. Instead of using a USRP, the measurement tool used for the following s_{11} measurements was a Rhode & Schwarz ZVL vector network analyzer. The equations used in this flowgraph include:

$$\Gamma = \frac{Z_L - Z_0}{Z_L + Z_0} \tag{3.3}$$

$$VSWR = \frac{1 + |\Gamma|}{1 - |\Gamma|} \tag{3.4}$$

$$|s_{11}| = \sqrt{\frac{\text{Power reflected from input}}{\text{Power incident on input}}} \tag{3.5}$$

$$s_{11} = \Gamma \tag{3.6}$$

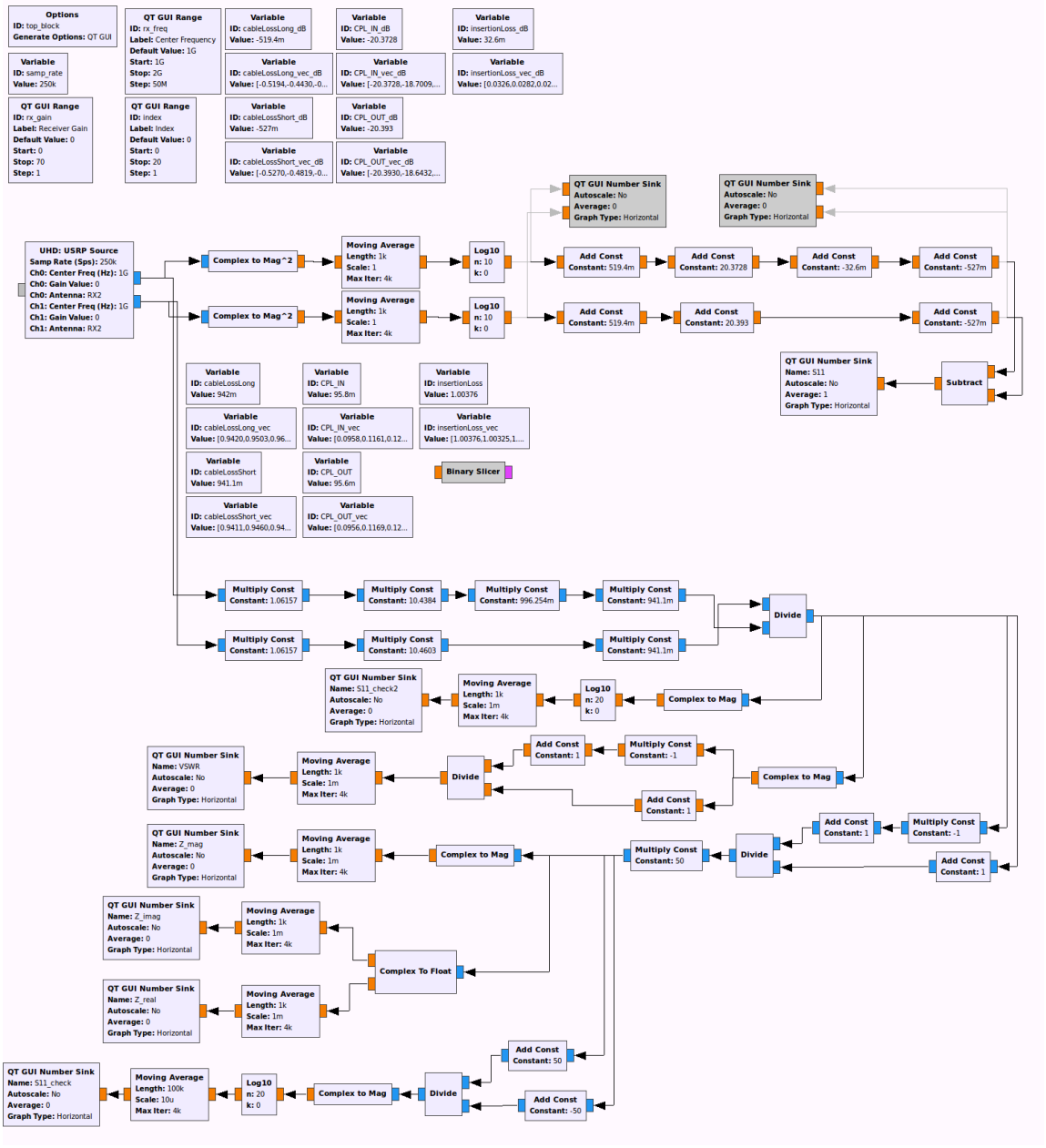

Figure 3.11: GNU Radio Companion Flowgraph for Antenna Measurements

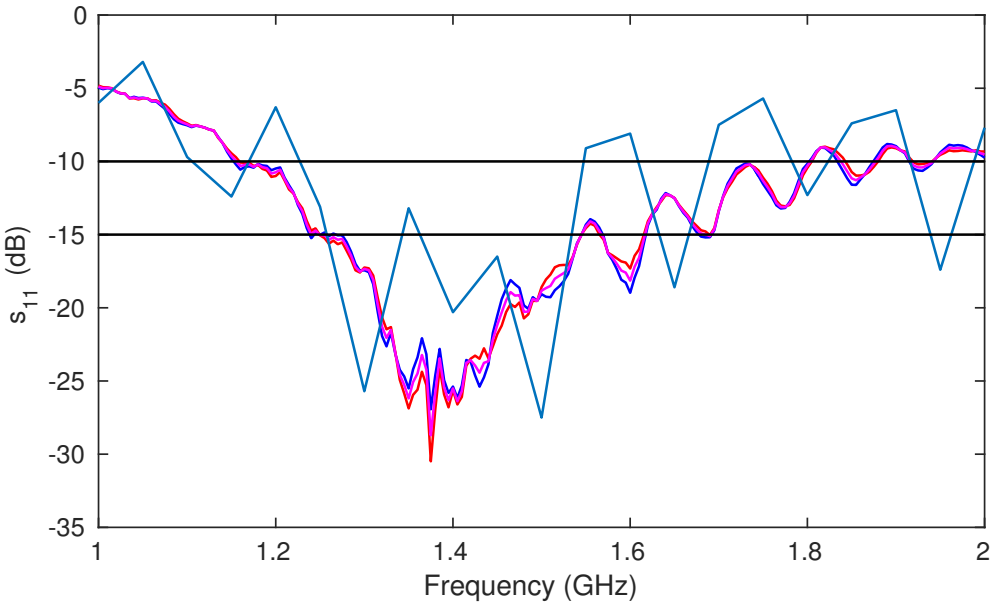

(a) EGaIn Height of 43mm (Dark Blue - Network Analyzer; Red - Network Analyzer; Magenta - Average Between Network Analyzer Measurements; Navy Blue - Bi-Directional Coupler Measurements)

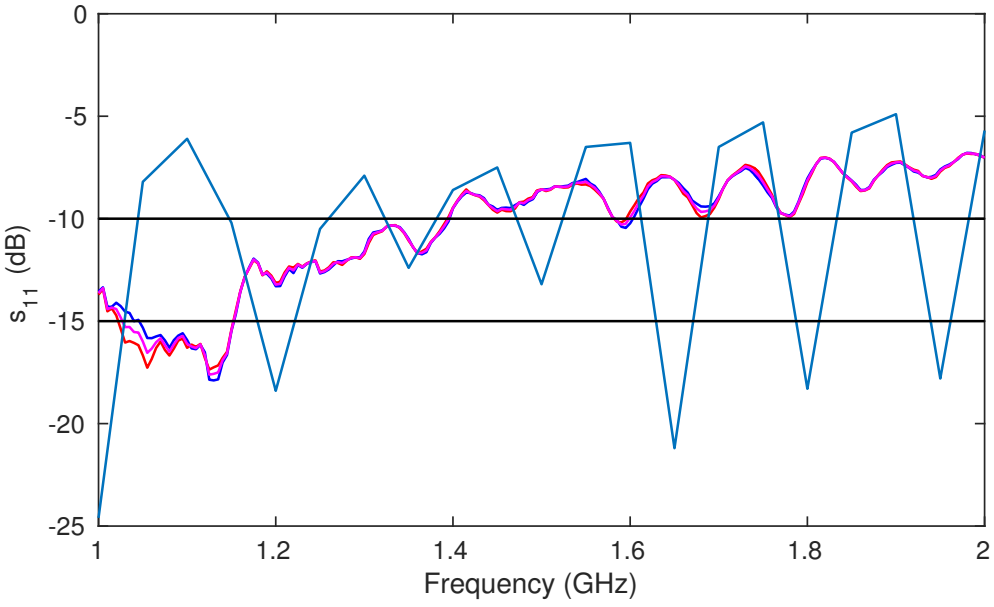

(b) EGaIn Height of 64mm (Dark Blue - Network Analyzer; Red - Network Analyzer; Magenta - Average Between Network Analyzer measurements; Navy Blue - Bi-Directional Coupler Measurements)

Figure 3.12: Network Analyzer vs. Bi-Directional Coupler Return Loss Results

3.4.1 Bottom Feed

In Fig. 3.13, FEKO simulations of a bottom-fed monopole antenna are presented and Fig. 3.14 network analyzer data from the liquid-metal monopole are presented. By comparing these two plots, it is clear that the simulation and experimental data are very similar to each other in terms of relative curves, however the network analyzer data drops down quite a bit further than the FEKO simulation. We think this is due to how FEKO handles the electrical feed of a thick monopole. In FEKO, monopoles are normally created using a wire and are very small in comparison with the wavelength of interest but in our case the monopole had to be modeled using a cylinder because of the large size of the inner diameter of the tubing. So, to model the bottom feed, a wire electrical feed was connected to the middle of the bottom of the larger cylinder antenna. This geometry could cause some mismatch issues that would negatively effect the return loss of the antenna because the energy is being transferred from a very small wire into the bottom of a large cylinder.

In Figs. 3.15-3.17, the radiation pattern data is compared. It is possible to see from the green curve (1.5 GHz) of Fig. 3.14 that the antenna has a 10 dB bandwidth of about 600 MHz and a 15 dB bandwidth of about 200 MHz. This turns out to be much better than the simulation, which barely reaches -10 dB at 1.5 GHz. In blue is the FEKO simulation of the radiation pattern and in red is the experimental

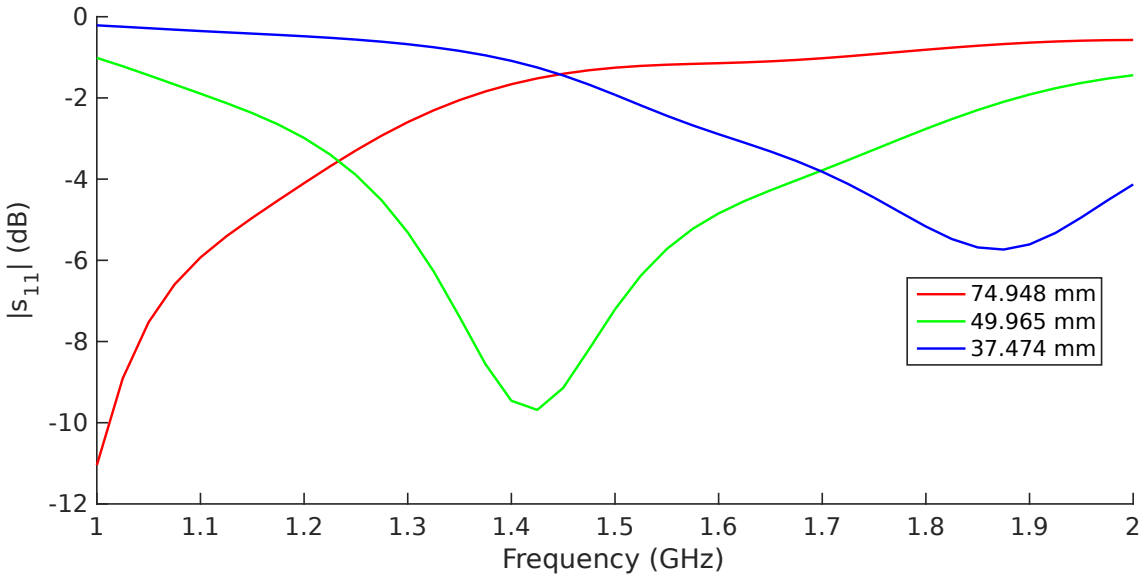

Figure 3.13: Bottom-Fed Monopole: s_{11} FEKO Results for 1.0 GHz (Red), 1.5 GHz (Green) and 2.0 GHz (Blue) Antennas with Diameter of 4.7625 mm

data collected. The experimental data curves are not as smooth because the data was taken by hand at 10 degree increments and fluctuates more because the power sensor that was used to take measurements fluctuated by a few tenths of a dBm to one dBm. All of the azimuth data points were taken at an angle of about 0 degrees, which is not the point of maximum gain for this monopole antenna. Theory says a monopole antenna should have a maximum gain of about 5.15 dBi; the FEKO simulations showed the monopole antenna having a maximum gain of about 4.57 dBi at 2 GHz, 4.23 dBi at 1.5 GHz and 3.6 dBi at 1 GHz; experimental results showed a maximum realized gain of 4.8 dBi at 2 GHz, 2.4 dBi at 1.5 GHz and 0.2 dBi at

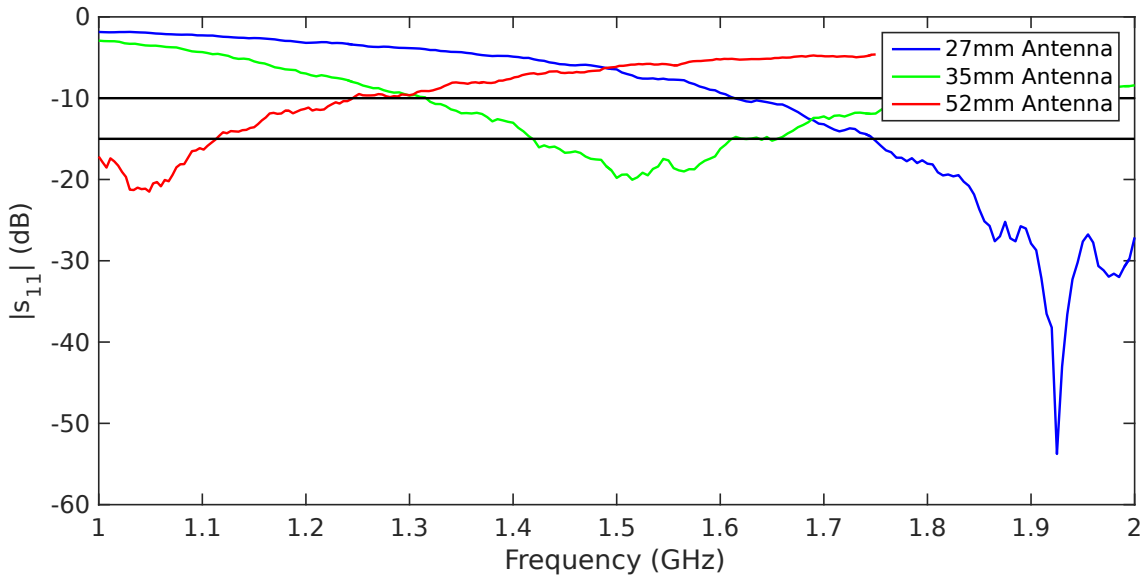

Figure 3.14: Bottom-Fed Monopole: s_{11} Network Analyzer Results for the Three Antenna Lengths Used for Radiation Patterns (Red - 52 mm; Green - 35 mm; Blue - 27 mm); Two Black Lines Are Reference Lines at -10 dB and -15 dB.

1 GHz. Since the s_{11} value for each antenna was below -15 dB at the frequency of interest, using the mismatch loss ($q = 1 - |s_{11}|^2$) showed the gain of each antenna was less than 0.1 dBi higher than the realized gain. From these radiation pattern plots, it is possible to see that the antenna is performing as expected from the simulation, however more testing is required to calculate the efficiency of the antenna.

More s_{11} results were taken with the network analyzer to show the effect of changing both the height of the liquid metal (Fig. 3.18) and the height of the NaOH on top of the liquid metal (Fig. 3.19). As shown in Fig. 3.18, as the liquid metal height changes, the center frequency shifts but the s_{11} parameter stays relatively even.

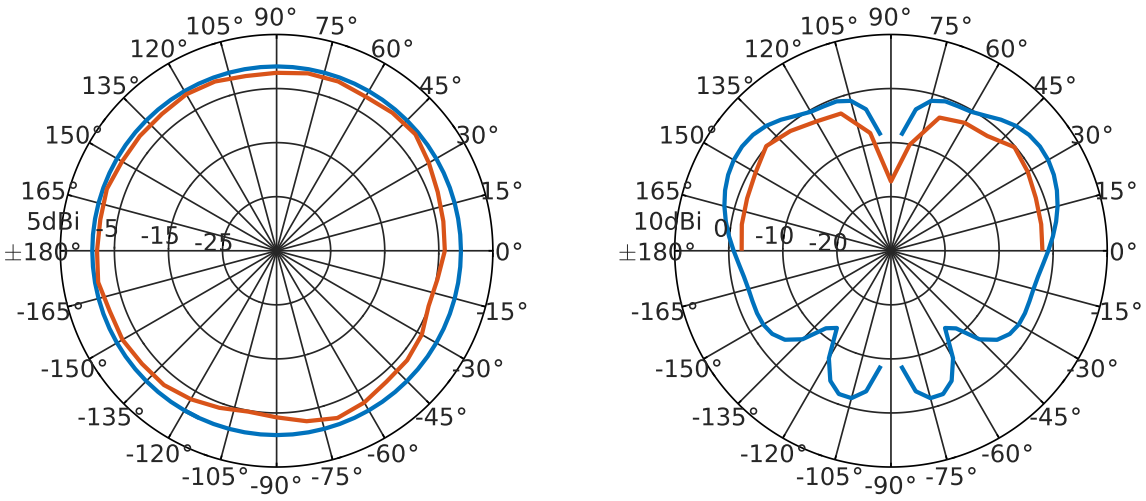

Figure 3.15: Bottom-Fed Monopole: s_{21} Results - 1.0 GHz (Blue - Simulation; Red - Experimental; Left - Azimuth; Right - Elevation). Azimuth Data Points Taken at 0 Degree Elevation in 10 Degree Increments.

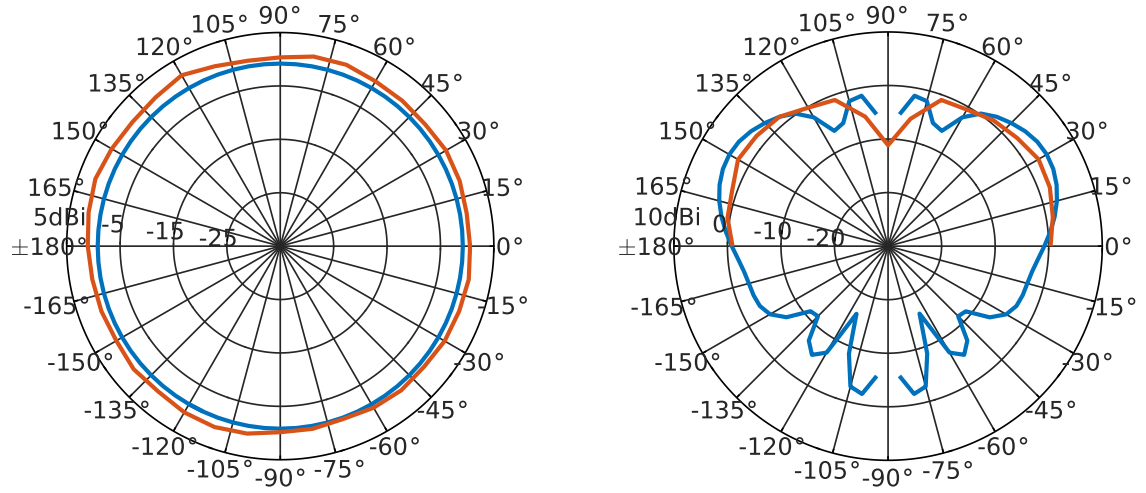

Figure 3.16: Bottom-Fed Monopole: s_{21} Results - 1.5 GHz (Blue - Simulation; Red - Experimental; Left - Azimuth; Right - Elevation). Azimuth Data Points taken at 0 Degree Elevation in 10 Degree Increments.

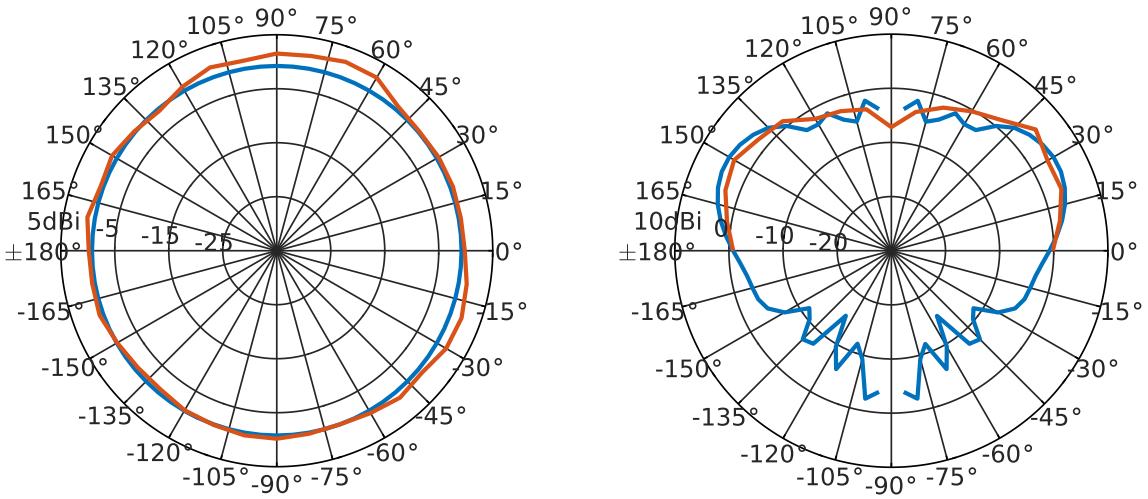

Figure 3.17: Bottom-Fed Monopole: s_{21} Results - 2.0 GHz (Blue - Simulation; Red - Experimental; Left - Azimuth; Right - Elevation). Azimuth Data Points Taken at 0 Degree Elevation in 10 Degree Increments.

In Fig. 3.19, the liquid metal height is kept the same and the height of the NaOH changes. The liquid-metal antenna with 1 mm of NaOH on top has a minimum s_{11} at ≈1.8 GHz, however when 30 mm of NaOH is added on top of the same antenna, the minimum swings to ≈1.1 GHz. This shows that as the amount of NaOH on top of the EGaIn incrases, the effective length of the antenna also increases because the resonant frequency is decreasing.

3.4.2 Bottom Feed with Injection Stub

The second antenna feed type was the bottom-fed monopole with the side stub for injecting or retracting the liquid metal. In Fig. 3.20, FEKO simulations of this

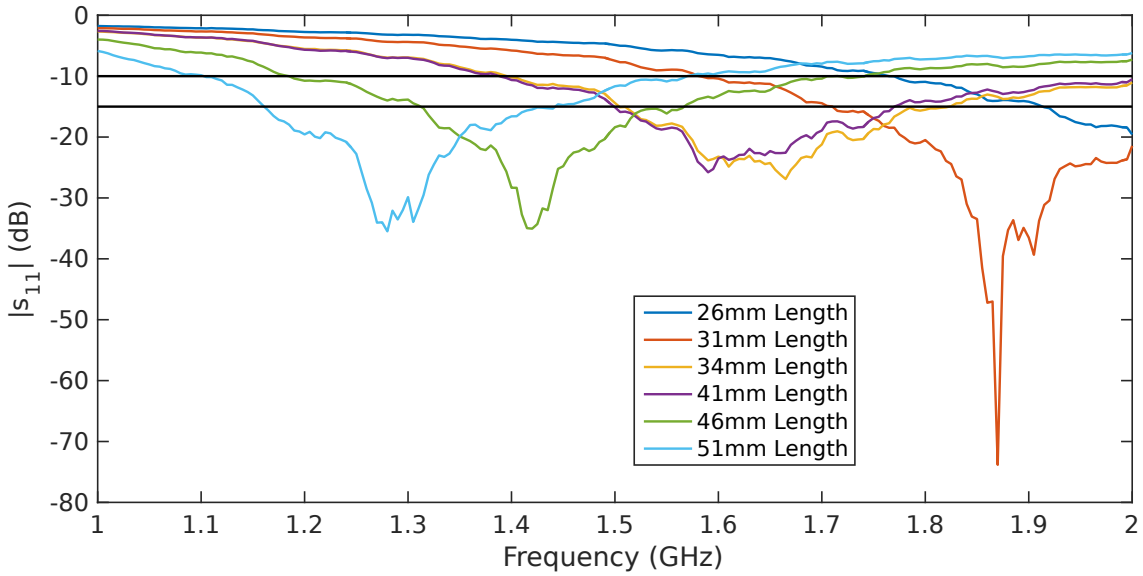

Figure 3.18: Bottom-Fed Monopole: s_{11} Network Analyzer Results for Multiple Liquid Metal Lengths with NaOH Height of 7 mm (Dark Blue - 26 mm; Red - 31 mm; Orange - 34 mm; Purple - 41 mm; Green - 46 mm; Light Blue - 51 mm)

antenna are presented and Fig. 3.21 network analyzer data from the liquid-metal monopole are presented. These two plots are very similar to each other, however the experimental antenna at 2 GHz (blue) had a strange oscillation after around 1.5 GHz. A possible explanation for this oscillation is due to the inside of the tubing used having small seams (Fig. 3.22). This could cause the current flowing over this seam to oscillate slightly at higher frequencies. Another possible explanation for this oscillation is due to standing waves caused by the reflective surfaces in the lab. An anechoic chamber and tubing without ridges would be needed to determine the cause of these oscillations. Also, for both the simulation and experimental results,

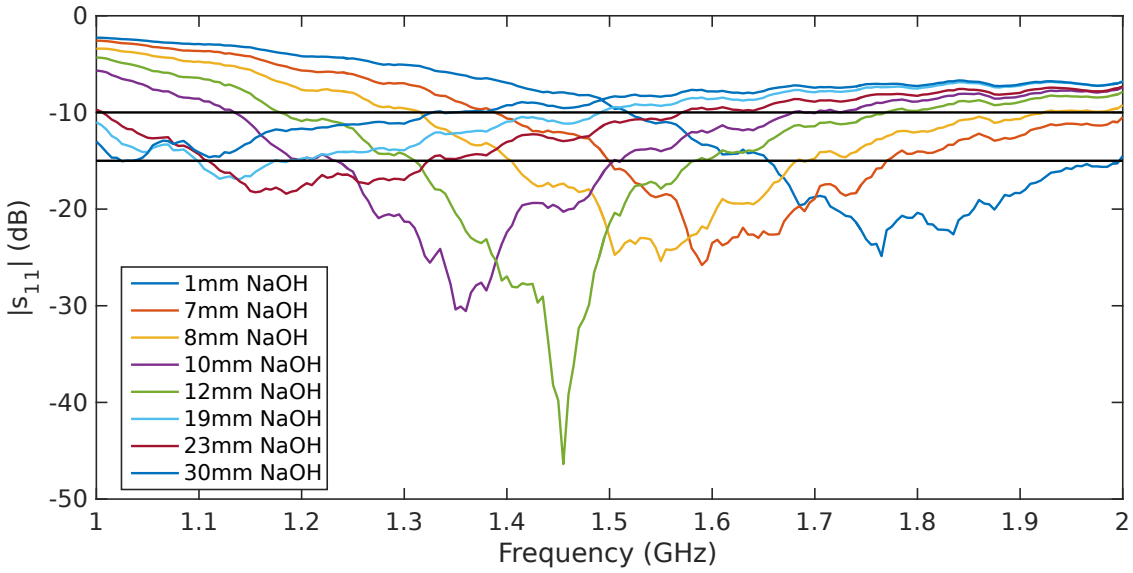

Figure 3.19: Bottom-Fed Monopole: s_{11} Network Analyzer Results for Multiple NaOH Heights with Liquid Metal Length of 33 mm (Blue - 1 mm; Red - 7 mm; Orange - 8 mm; Purple - 10 mm; Green - 12 mm; Light Blue - 19 mm; Maroon - 23 mm; Dark Blue - 30 mm)

the 2 GHz antenna had a lower s_{11} parameter than 1 GHz or 1.5 GHz. As shown in Fig. 3.21, the green curve has a 10 dB bandwidth of about 550 MHz, while the simulation (Fig. 3.20) had a 10 dB bandwidth of less than 100 MHz. This is most likely due to the thickness of the monopole and FEKO making assumptions about how to account for a thick monopole.

In Figs. 3.23-3.25, the radiation pattern data from simulation and experiments are compared. As in the previous antenna, the experimental data curves are not as smooth because the data was taken by hand at 10 degree increments and fluctuates

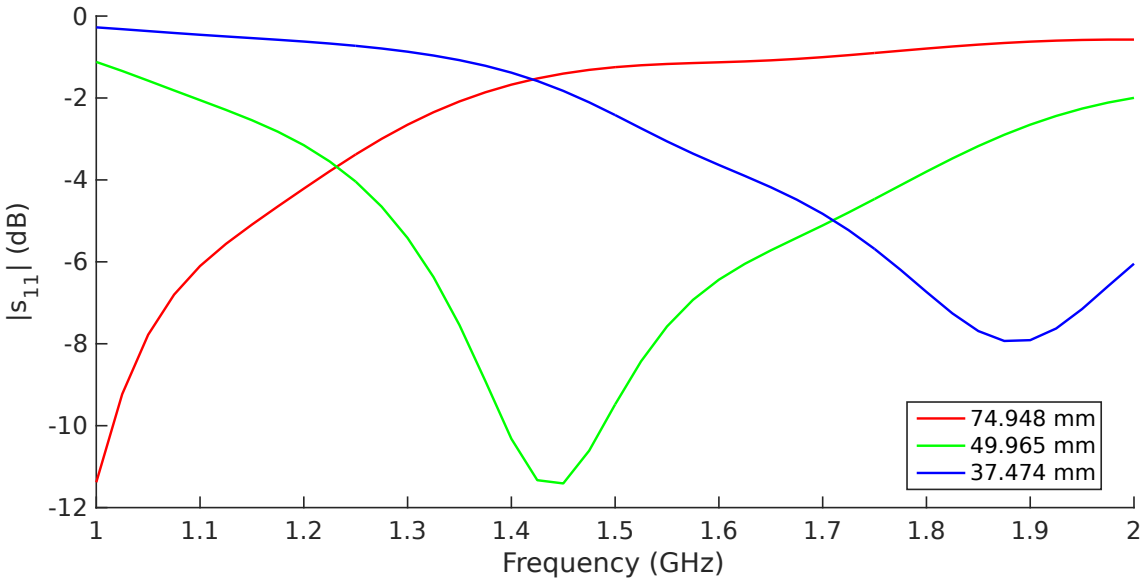

Figure 3.20: Bottom-Fed Monopole with Injection Stub: s_{11} FEKO Results for 1.0 GHz (Red), 1.5 GHz (Green) and 2.0 GHz (Blue) Antennas with Diameter of 4.7625 mm

more because the power sensor. All of the azimuth data points were taken at an angle of about 0 degrees, which is not the point of maximum gain for this monopole antenna.

More s_{11} results were taken with the network analyzer to show the effect of changing both the height of the liquid metal (Fig. 3.26) and the height of the NaOH on top of the liquid metal (Fig. 3.27). As shown in Fig. 3.26, as the liquid metal height changes, the center frequency shifts, however in this antenna the s_{11} parameter does not remain even. As the antenna shortens and approaches 2 GHz, the s_{11} parameter gets worse, but still remains below -10 dB. In Fig. 3.27, the liquid metal height is

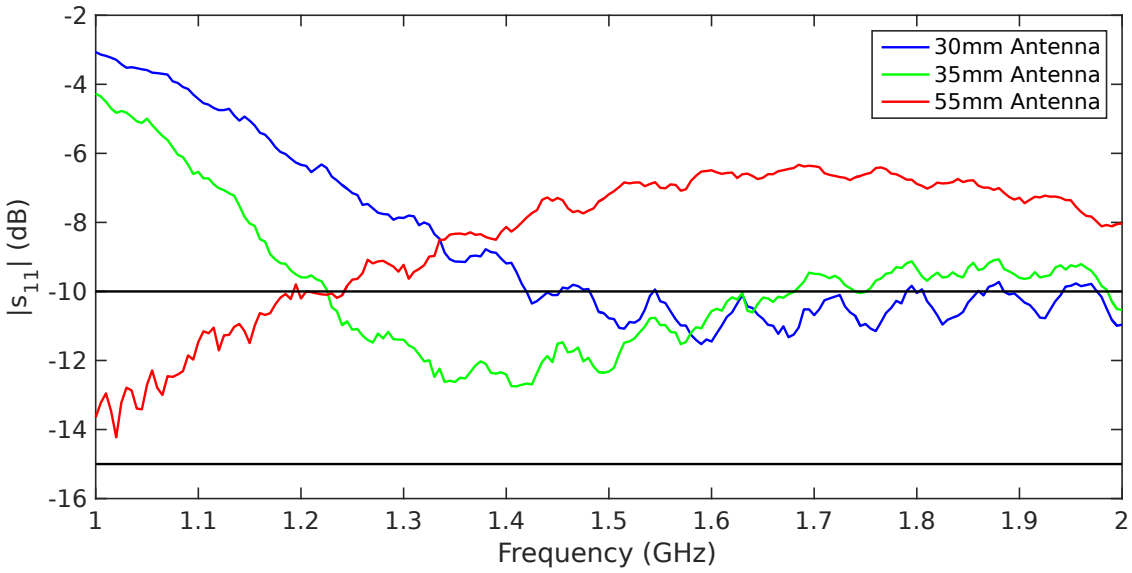

Figure 3.21: Bottom-Fed Monopole with Injection Stub: s_{11} Network Analyzer Results for the Three Antenna Lengths Used for Radiation Patterns (Blue - 30 mm; Green - 35 mm; Red - 55 mm)

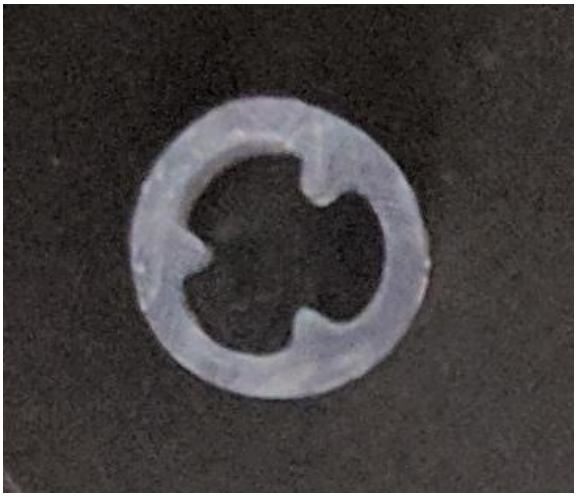

Figure 3.22: Ridges Along the Inside of the Tubing Possibly Cause Oscillations in the Return Loss at High Frequencies

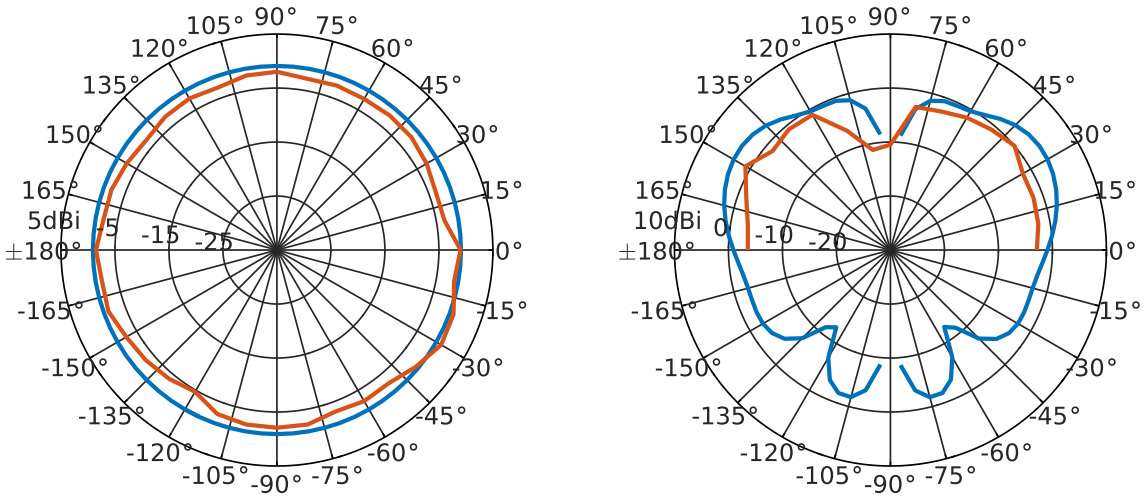

Figure 3.23: Bottom-Fed Monopole with Stub: s_{21} Results - 1.0 GHz (Blue - Simulation; Red - Experimental; Left - Azimuth; Right - Elevation). Azimuth Data Points Taken at 0 Degree Elevation in 10 Degree Increments.

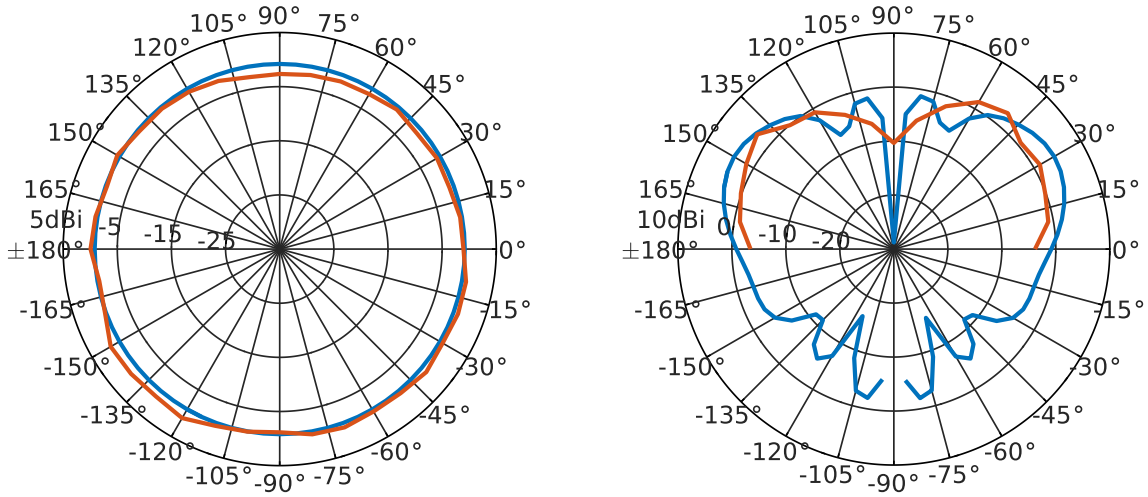

Figure 3.24: Bottom-Fed Monopole with Stub: s_{21} Results - 1.5 GHz (Blue - Simulation; Red - Experimental; Left - Azimuth; Right - Elevation). Azimuth Data Points Taken at 0 Degree Elevation in 10 Degree Increments.

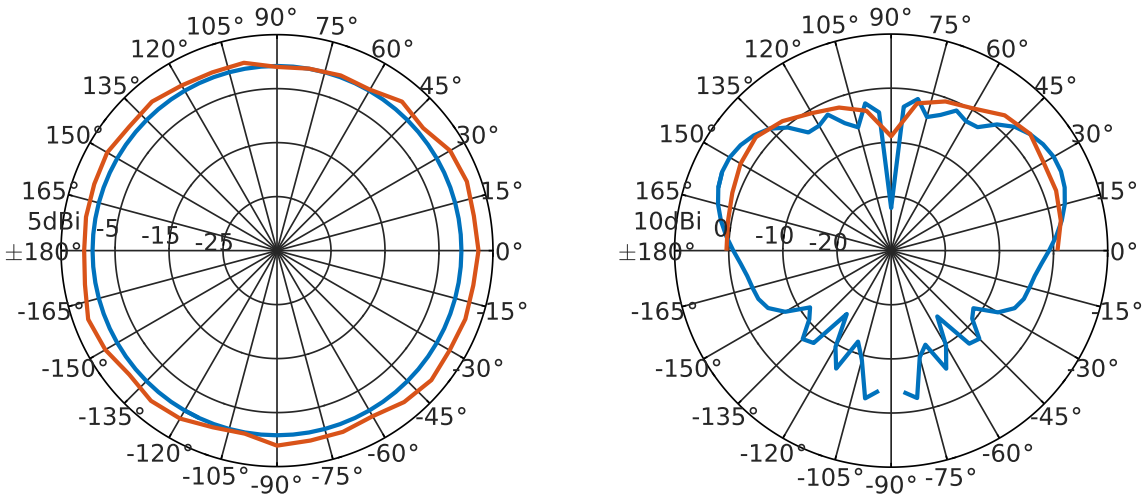

Figure 3.25: Bottom-Fed Monopole with Stub: s_{21} Results - 2.0 GHz (Blue - Simulation; Red - Experimental; Left - Azimuth; Right - Elevation). Azimuth Data Points Taken at 0 Degree Elevation in 10 Degree Increments.

kept the same and the height of the NaOH changes. As shown in this plot, the return loss stays relatively even at around −18 dB. When the NaOH height was increased to 37 mm, there was a drop in return loss near 2 GHz because this is very close to a half-wavelength monopole. With a EGaIn height of 41 mm and a NaOH height of 37 mm, the effective length of the antenna is 78 mm, while a half-wavelength monopole at 2 GHz would be 75 mm. The return loss remains at around −18 dB even though the NaOH height is almost equal to the EGaIn height.

3.4.3 Offset Feed below Ground Plane

The third and final antenna feed type was the offset-fed monopole that was below the ground plane. In Fig. 3.28, FEKO simulations of this antenna are presented and Fig. 3.29 network analyzer data from the liquid-metal monopole are presented. Again, the simulation and experimental data are similar with the network analyzer data showing an s_{11} that is slightly better. This feed method was the easiest to inject and retract metal from the antenna, just having to turn a valve near the feed point and pushing or pulling on the plunger of the syringe.

In Figs. 3.30-3.32, the radiation pattern data from simulation and experiments are compared. In the previous two antenna feed types, the azimuth data followed much closer to the simulated pattern than this antenna feed type. The data shows that this feed was still keeping a similar pattern but was commonly jumping around with a difference of 4 dB and sometimes 8 dB. Also, for this antenna, as the antenna height approached 2 GHz, the antenna would start transmitting more energy below the ground plane than above it. This is due to the length of metal sitting below the ground plane to be too close to resonant at 2 GHz. This caused the antenna to have about a 0 dBi realized gain above the ground plane at 2 GHz. At 1.5 GHz, the antenna had about a 2 dBi maximum realized gain and at 1 GHz, the antenna had a 1.5 dBi maximum realized gain. From this, it can be concluded that this feed type

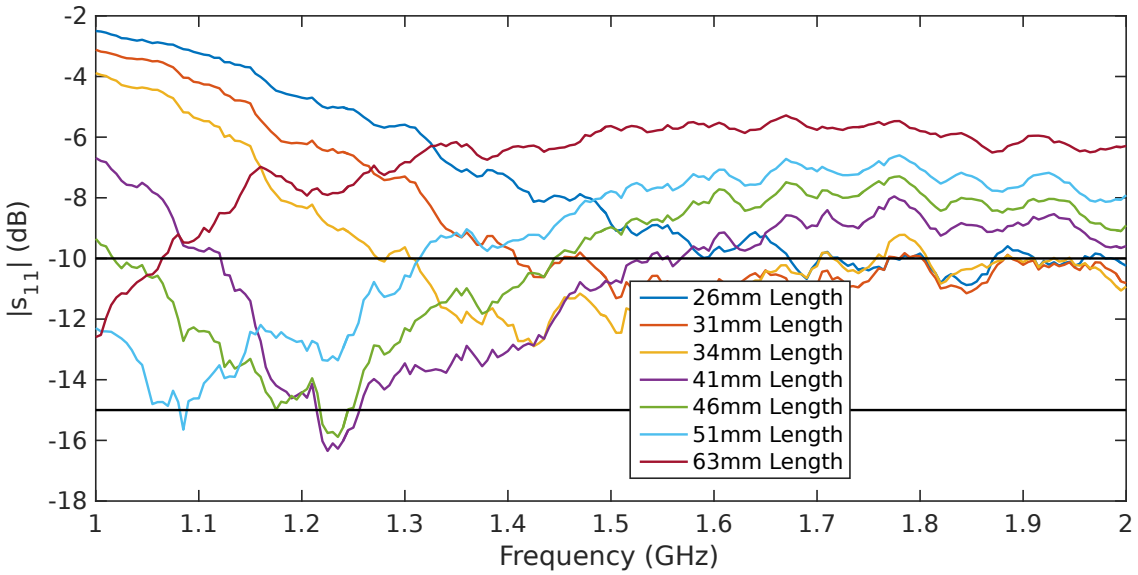

Figure 3.26: Bottom-Fed Monopole with Injection Stub: s_{11} Network Analyzer Results for Multiple Liquid Metal Lengths with NaOH Height of 4 mm (Blue - 26 mm; Red - 31 mm; Orange - 34 mm; Purple - 41 mm; Green - 46 mm; Light Blue - 51 mm; Maroon - 63 mm)

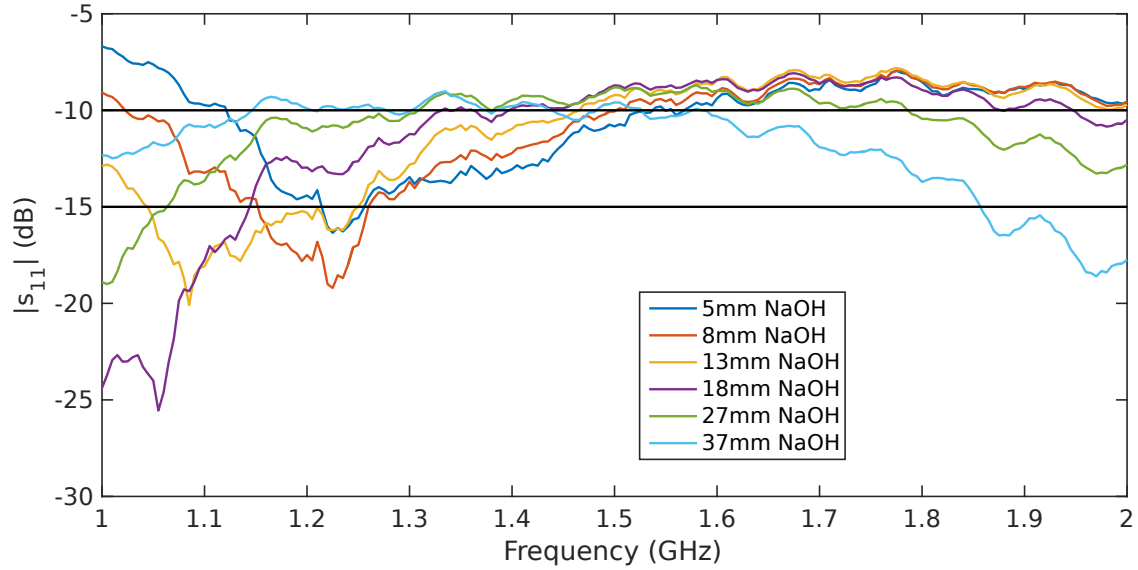

Figure 3.27: Bottom-Fed Monopole with Injection Stub: s_{11} Network Analyzer Results for Multiple NaOH Heights with Liquid Metal Length of 41 mm (Blue - 5 mm; Red - 8 mm; Orange - 13 mm; Purple - 18 mm; Green - 27 mm; Light Blue - 37 mm)

would only work for antennas of lower frequencies unless the metal that is below the ground plane can be lessened or eliminated.

More s_{11} results were taken with the network analyzer to show the effect of changing both the height of the liquid metal (Figs. 3.33- 3.34) and the height of the NaOH on top of the liquid metal (Fig. 3.35). Interestingly in Fig. 3.35, the larger amounts of NaOH on the antenna, the better the match of the antenna (the lower the return loss). This could be due to this specific feed inherently performing better at lower frequencies. So as the effective length of the antenna increased with the increased amount of NaOH, the resonant frequency decreased.

As the height of the antenna approached the length below the ground plane, the performance of the antenna decreased. This means that as the antenna approached 2 GHz, the performance of the antenna decreased. Since there is extra metal down below the ground plane, the coupling effect of this metal was tested by moving a syringe full of liquid metal in close proximity with the antenna (Fig. 3.36). The effects on the s_{11} parameter of moving this liquid metal in close proximity is show in Figs. 3.37-3.39.

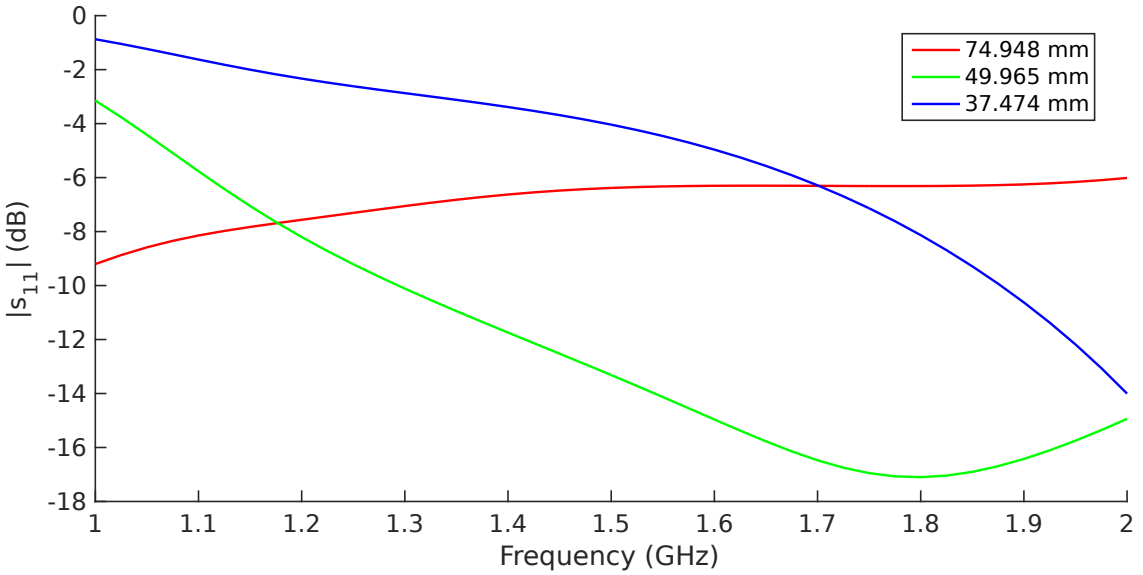

Figure 3.28: Offset-Fed Monopole with Injection Stub: s_{11} FEKO Results for 1.0 GHz (Red), 1.5 GHz (Green) and 2.0 GHz (Blue) Antennas with Diameter of 4.7625 mm

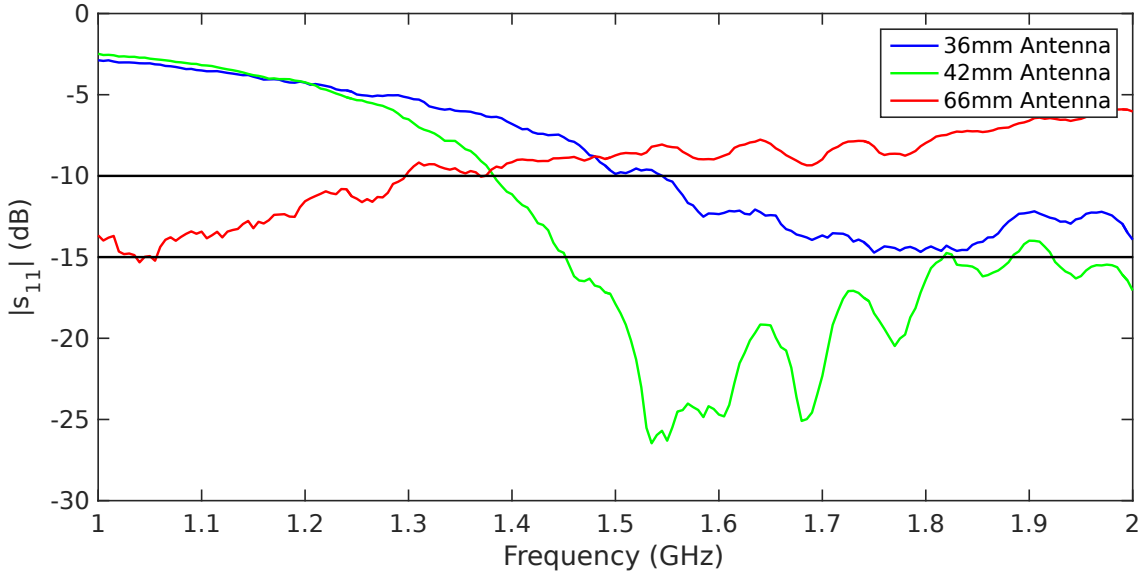

Figure 3.29: Offset-Fed Monopole: s_{11} Network Analyzer Results for the Three Antenna Lengths Used for Radiation Patterns (Blue - 36 mm; Green - 42 mm; Red - 66 mm)

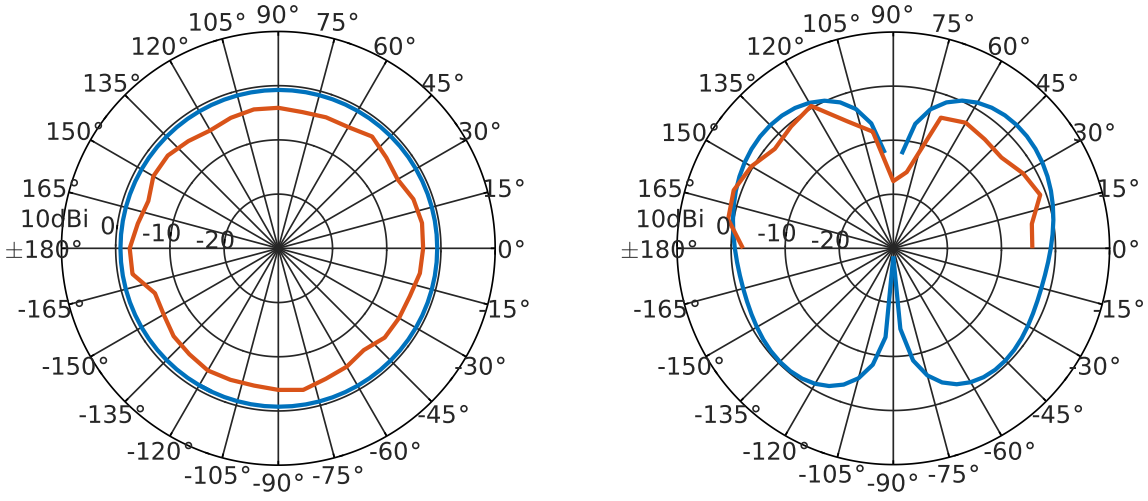

Figure 3.30: Offset-Fed Monopole: s_{21} Results - 1.0 GHz (Blue - Simulation; Red - Experimental; Left - Azimuth; Right - Elevation). Azimuth Data Points Taken at 0 Degree Elevation in 10 Degree Increments.

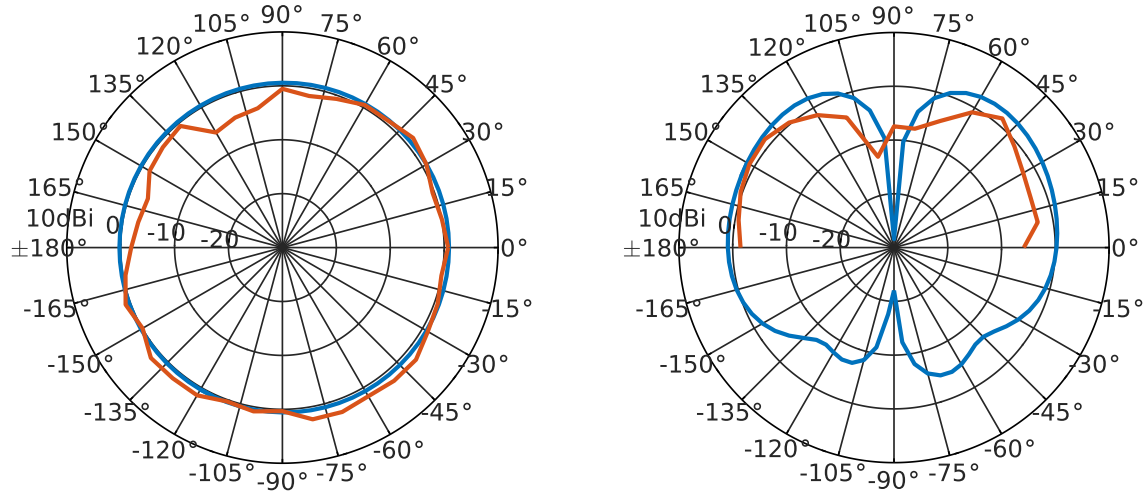

Figure 3.31: Offset-Fed Monopole: s_{21} Results - 1.5 GHz (Blue - Simulation; Red - Experimental; Left - Azimuth; Right - Elevation). Azimuth Data Points Taken at 0 Degree Elevation in 10 Degree Increments.

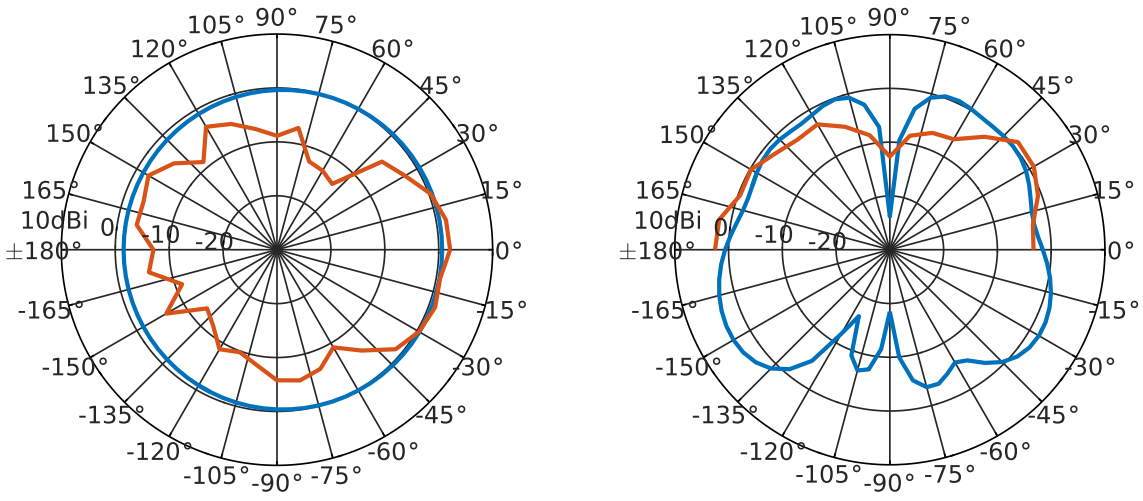

Figure 3.32: Offset-Fed Monopole: s_{21} Results - 2.0 GHz (Blue - Simulation; Red - Experimental; Left - Azimuth; Right - Elevation). Azimuth Data Points Taken at 0 Degree Elevation in 10 Degree Increments.

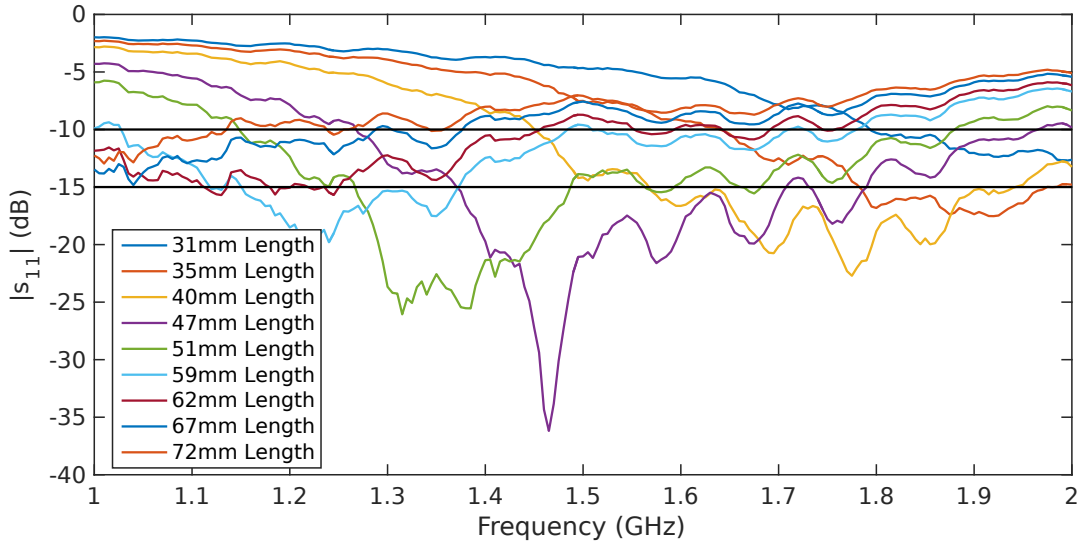

Figure 3.33: Offset-Fed Monopole: s_{11} Network Analyzer Results for Multiple Liquid Metal Lengths with NaOH Height of 0 mm (Blue - 31 mm; Red - 35 mm; Orange - 40 mm; Purple - 47 mm; Green - 51 mm; Light Blue - 59 mm; Maroon - 62 mm; Blue - 67 mm; Red - 72 mm)

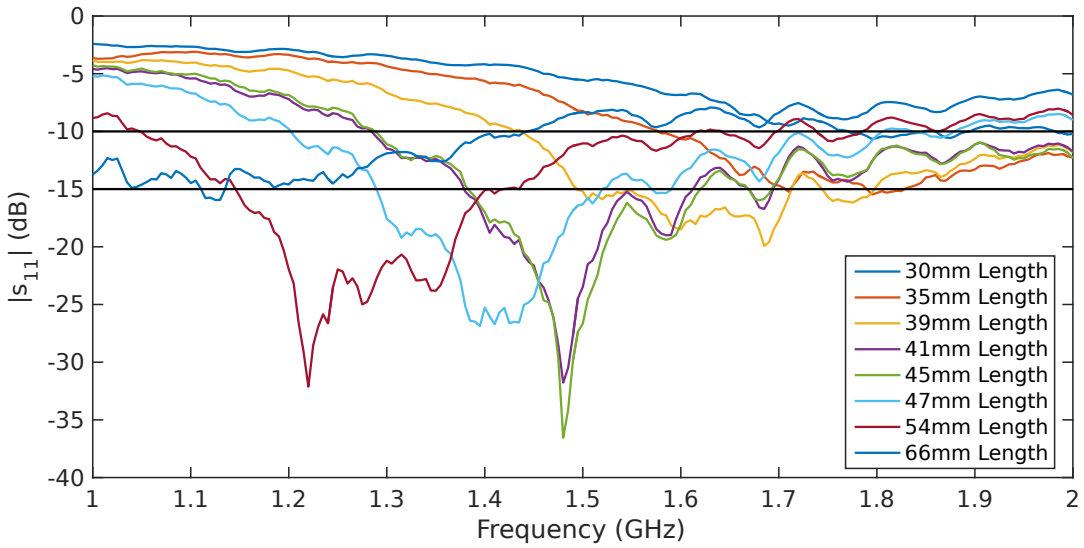

Figure 3.34: Offset-Fed Monopole: s_{11} Network Analyzer Results for Multiple Liquid Metal Lengths with NaOH Height of 2 mm (Blue - 30 mm; Red - 35 mm; Orange - 39 mm; Purple - 41 mm; Green - 45 mm; Light Blue - 47 mm; Maroon - 54 mm; Blue - 66 mm)

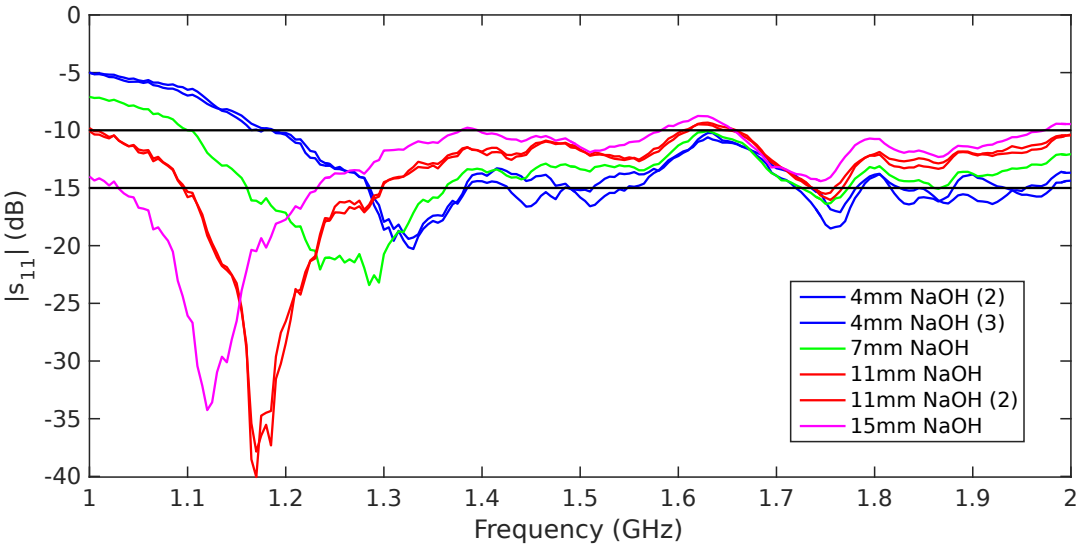

Figure 3.35: Offset-Fed Monopole: s_{11} Network Analyzer Results for Multiple NaOH Heights with Liquid Metal Length of 46 mm (Blue - 4 mm; Green - 7 mm; Red - 11 mm; Cyan - 15 mm)

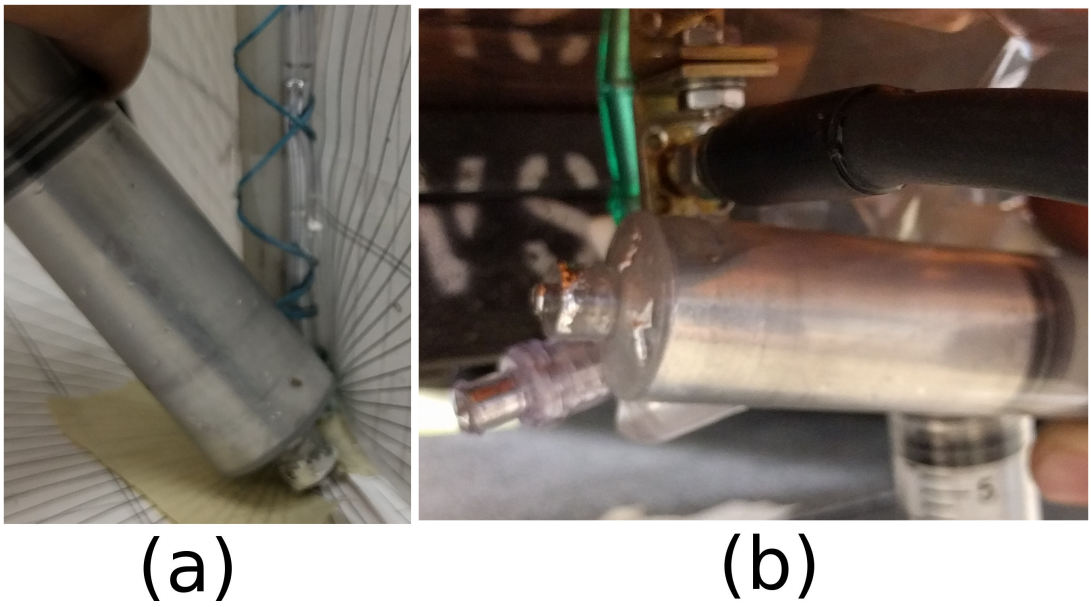

Figure 3.36: (a) Test Setup For the Coupling of the Liquid Metal Below the Ground Plane; (b) Test Setup For the Coupling of the Liquid Metal Above the Ground Plane

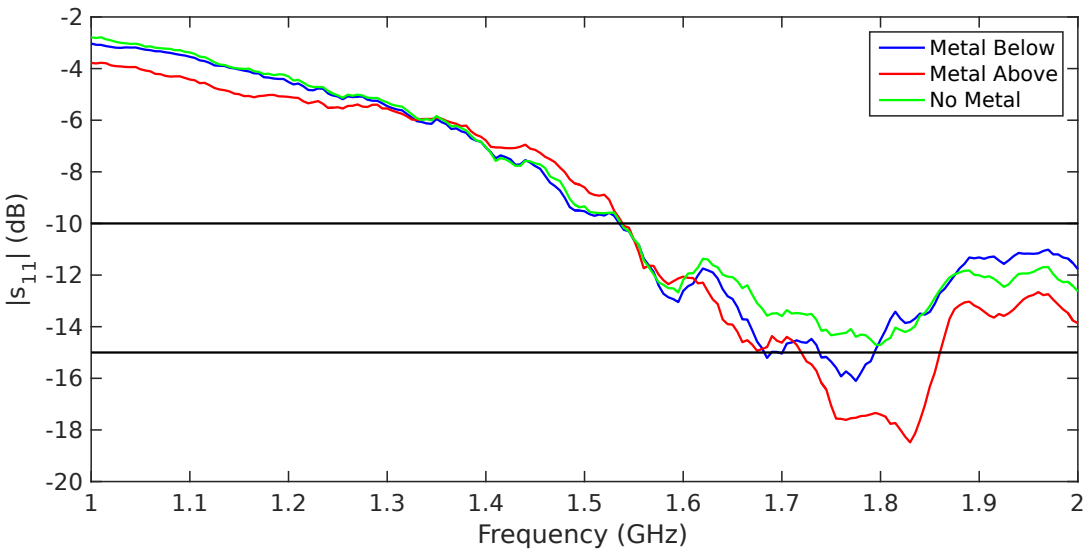

Figure 3.37: Results of Coupling with 36 mm Antenna (Blue - Metal Below the Ground Plane; Red - Metal Above the Ground Plane; Green - No Metal in Proximity)

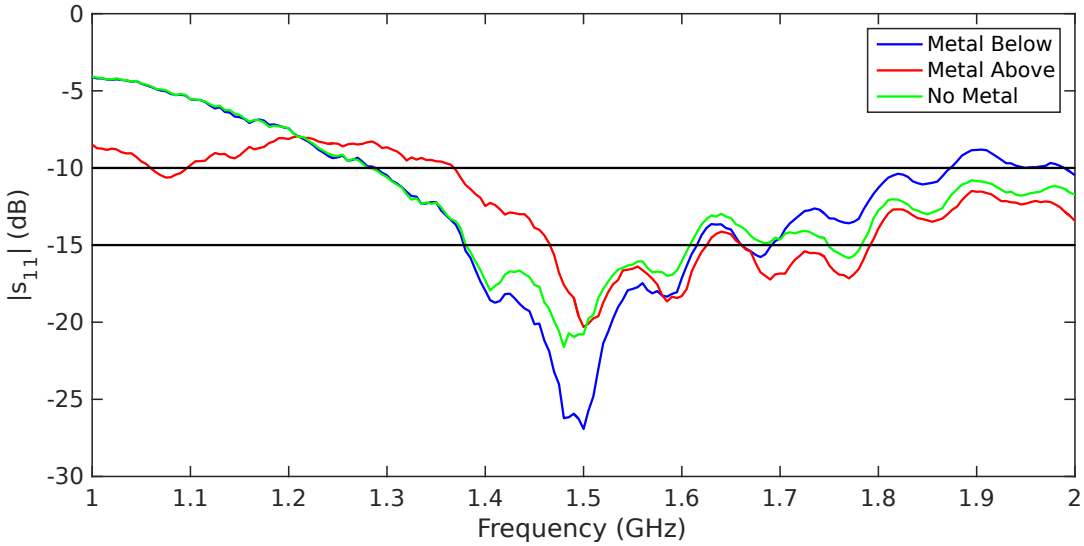

Figure 3.38: Results of Coupling with 42 mm Antenna (Blue - Metal Below the Ground Plane; Red - Metal Above the Ground Plane; Green - No Metal in Proximity)

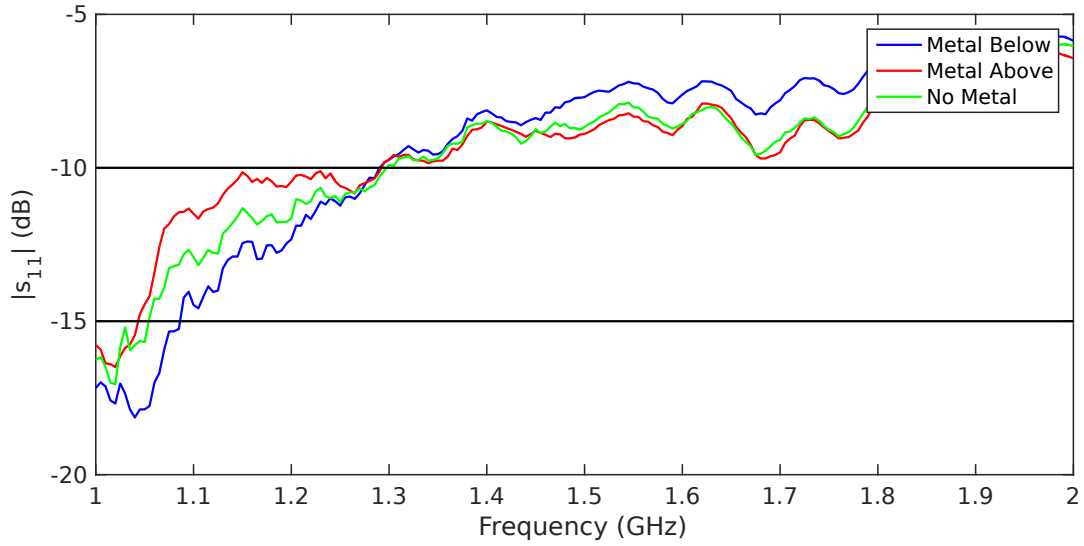

Figure 3.39: Results of coupling with 66 mm antenna (Blue - Metal Below the Ground Plane; Red - Metal Above the Ground Plane; Green - No Metal in Proximity)

3.5 Wheeler Cap

A Wheeler Cap is a method for determining the efficiency of an antenna first suggested by Dr. Harold A. Wheeler in 1959 [6]. The efficiency of the antenna is the proportion of power the antenna actually radiates versus the amount of power delivered to it, in other words, efficiency quantifies the resistive losses of the antenna. The antenna's loss can be modeled as a resistor placed in series with the radiation resistance (Fig. 3.40), assuming the antenna is at resonance, so there is no reactance.

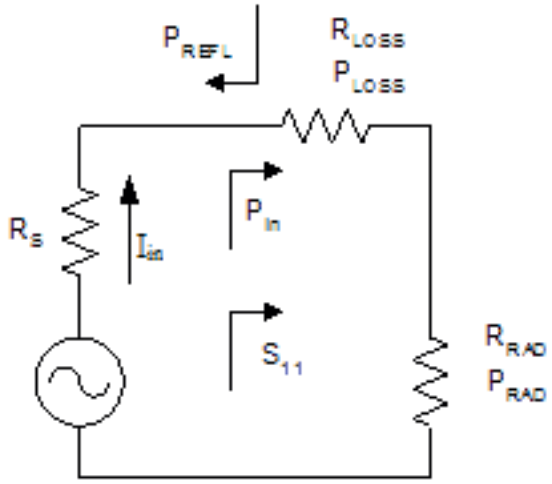

Figure 3.40: Model of Antenna Loss [8]

The method described by Wheeler places a hollow conductive sphere at the radius of the transition between the energy-storing near field and its radiating far field [8]. This transition radius occurs at a distance of $\frac{\lambda}{2\pi}$. The idea here is all the power

radiated by the antenna is reflected back by the cap and not allowed to escape, making $R_{rad} = 0$. Thus by making separate s_{11} measurements with and without the cap, the efficiency of the antenna can be obtained. Given the radius of the cap, a $\frac{\lambda}{4}$ monopole antenna will now fit under the cap, therefore a cylindrical cap is necessary. The derivation of the efficiency from return loss measurements are described in C.2.

Fig. 3.41 shows the prototype Wheeler Caps that were used in the efficiency experiment. Figs. 3.42- 3.44 show the return loss curves for the antennas in free space and with the Wheeler Cap in place for 1 GHz, 1.5 GHz and 2 GHz. The efficiency of the antenna was calculated using the constant loss resistor method equation (Eqn. 3.7). The results are listed in Table 3.1. From the results, all three antennas have a lower efficiency at 2 GHz, this could be due to the construction of the Wheeler Cap. As can be seen in Fig. 3.41, the prototype Wheeler Caps are not perfectly circular, which can cause some problems if they infringe on the near field of the antenna. Also, the material used to make the caps is aluminum, which has a finite conductivity, therefore some of the energy incident on the Wheeler Cap will be lost due to Ohmic losses rather than reflected back to the antenna. In [5], prototype Wheeler Caps were designed and tested on multiple different types of antennas. For the monopole antenna, a radiation efficiency of $> 99\%$ was measured between 1 GHz and 3 GHz. The liquid-metal monopole designed in this section has a lower radiation

efficiency than the monopole antenna in [5]. This discrepancy could be a result of the liquid metal having a lower conductivity, leading to more Ohmic losses, and/or the Wheeler Caps constructed for this thesis are not as structurally exact as the Wheeler Caps machined by Wang.

Figure 3.41: Prototype Wheeler Caps (From Left to Right: 1 GHz, 1.5 GHz, 2 GHz)

$$\epsilon_e = 1 - \frac{(1 - s_{11_{FS}})(1 + s_{11_{WC}})}{(1 + s_{11_{FS}})(1 - s_{11_{WC}})} \tag{3.7}$$

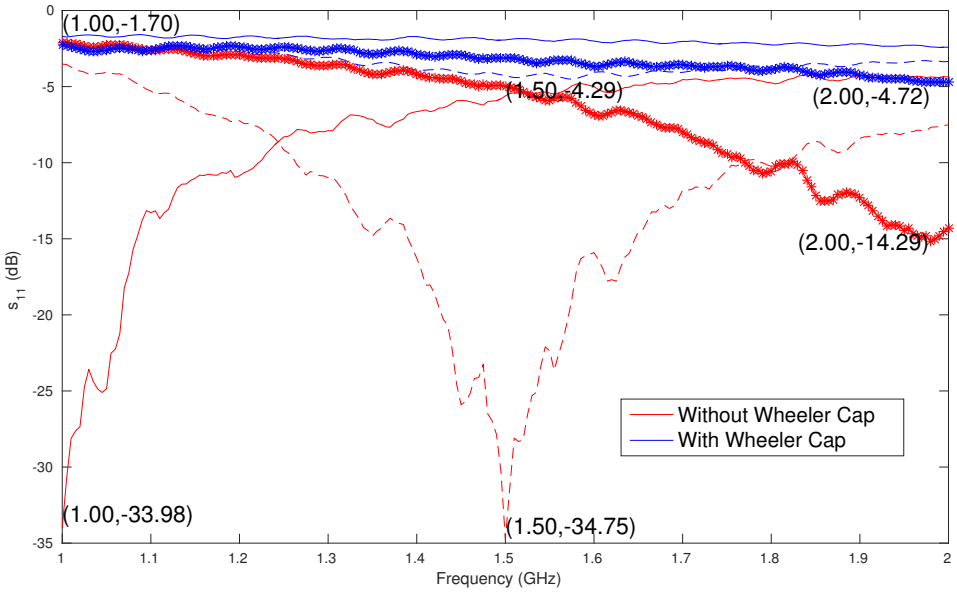

Figure 3.42: Return Loss for Bottom-Fed Antenna with (Blue) and Without (Red) the Wheeler Cap at 1 GHz (Solid), 1.5 GHz (Dashed), and 2 GHz (Star)

Table 3.1: Calculated Antenna Radiation Efficiency Using Wheeler Cap

Frequency	Bottom Fed	Bottom Fed with Stub	Offset Fed
1.0 GHz	86%	82%	74%
1.5 GHz	75%	77%	63%
2.0 GHz	67%	65%	55%

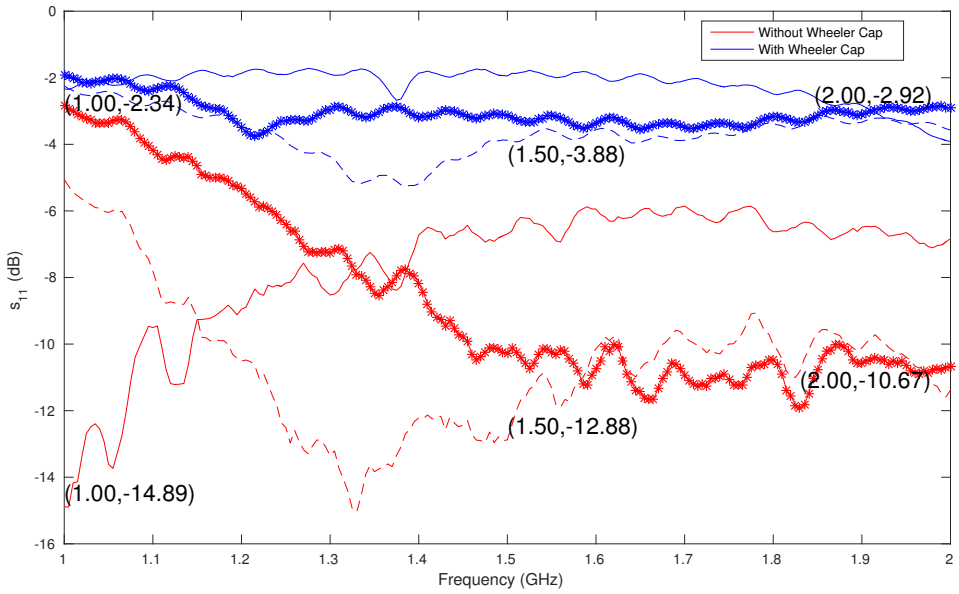

Figure 3.43: Return Loss for Bottom-Fed with Injection Stub Antenna With (Blue) and Without (Red) the Wheeler Cap at 1 GHz (Solid), 1.5 GHz (Dashed), and 2 GHz (Star)

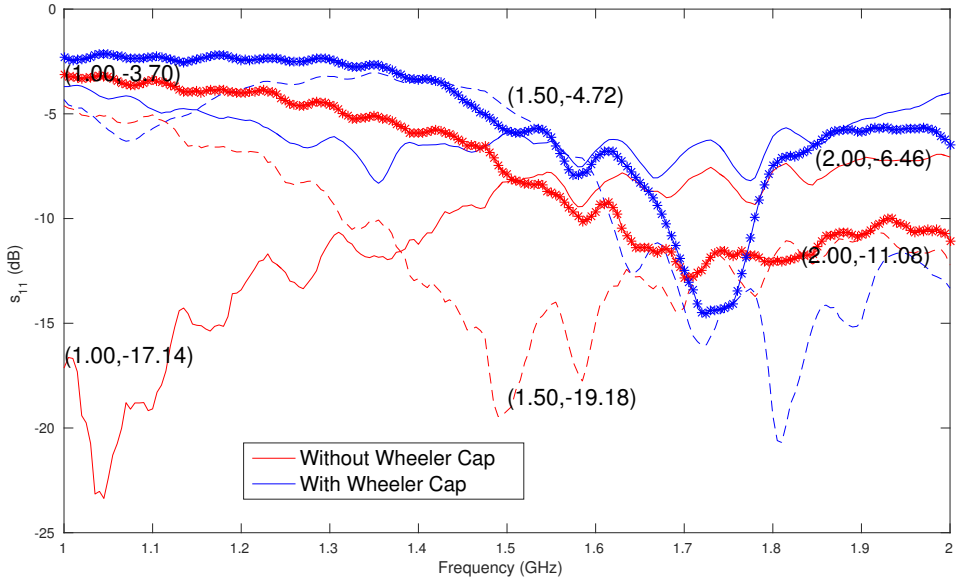

Figure 3.44: Return Loss for Offset-Fed Antenna With (Blue) and Without (Red) the Wheeler Cap at 1 GHz (Solid), 1.5 GHz (Dashed), and 2 GHz (Star)

3.6 Conclusion

This section analyzed three unique feed methods for the liquid-metal monopole antenna. Simulations done in FEKO were compared with experimental results taken in a chemical lab. These comparisons showed the prototype antennas performed as well as expected based on FEKO simulations. Depending on the applications, different feed methods would be more practical than others. The offset feed is the easiest to scale to a more complex antenna array, however the excess metal below the ground plane would need to be decreased for this antenna to function efficiently at higher frequencies. The bottom-fed monopole with the stub is the next easiest to combine with a reservoir system but with this antenna, the metal that remains in the tubing between the antenna and the reservoir would need to be retracted back into the reservoir with each use. Otherwise, that metal will couple with the metal inside the antenna and would ruin the antenna's efficiency. A closer look at the gamma match needs to be taken because this feed method would hopefully eliminate the problem of the offset feed by having the feed raised above the ground plane and a shorting pin to ground the antenna at the base. This would hopefully limit the amount of current that travels to the metal below the ground plane and radiates energy downward.

Chapter 4

Parasitic Monopole Array

The goal of this section is to expand from previously researched liquid-metal linear array models [97, 98] into a dynamically driven two-dimensional liquid-metal array. Simulations were performed using FEKO to prove the concept that a multi-dimensional array will provide the user more control over the direction of the main beam and also the direction of the nulls, making the resulting array useful for spatially tracking signals and mitigating interference. A proof-of-concept hardware model of the 2D array antenna was built and tested in the context of a dual-frequency GPS antenna (L1, L2/L5), with results found comparable to simulation. Since the antennas are made from liquid metal, these results make it possible for the user to change the parasitic elements within the 2D array from negligible (height of zero) to directors, to reflectors, or back with the use of a syringe or pump. This spatially

adaptable antenna also benefits from the use of a single digitizer chain, offering a concrete alternative for anti-jam GPS antennas as the technology matures.

4.1 Introduction

Previous work done at the University of Hawaii at Manoa [97, 98] showed that it is possible to create a linear Yagi-Uda antenna with liquid metal, and with this design, be able to change the direction of maximum gain by adjusting the liquid metal heights. Some simulation work done by some researchers at Illinois Institute of Technology [131], showed it is possible to design a 2D passive element array that allows for extensive control over beam steering. The Yagi-Uda antenna is an optimization problem by adjusting the spacing and heights of the parasitic elements [132,133]. When using conventional solid Yagi-Uda antennas, the spacing and height of the directors and reflectors must be chosen and set at specific values, but when using liquid metal, the spacing must still remain constant, but the height of each of the elements can be adjusted to fit the needs of the user.

By steering the main beam/nulls of the antenna, a single antenna feed can be used with near field parasitic to subsequently locate a signal. This has an advantage over common phased arrays because this requires only a single electrical feed and

doesn't require phase shifters at all. Therefore the overall cost, complexity, and power consumption of the antenna system as a whole is decreased. Another method commonly used to do beam steering besides phased arrays is mounting the antenna on a mechanical gimbal structure. This type of structure is often heavy and the mechanical components are less durable, potentially wearing out over time. The parasitic elements act as directors or reflectors depending on their height and can be adjusted by injecting or retracting the liquid metal to control the beam. One example where this ability could be useful is in anti-jam GPS (AJ-GPS) antennas. The most common technique for pre-correlation protection against interference is using a controlled radiation pattern antenna (CRPA) [134, 135]. The proposed antenna could be used to steer nulls in the direction of an interfering signal, while still being able to track the satellites with the steerable main beam.

This section will discuss the fundamentals of a parasitic monopole array and how maximum performance can be achieved by deciding both the spacing and height of the parasitic elements. With the parasitic elements being made from liquid-metal conductors, this gives the antenna the ability to actively change the height of the elements, while the spacing must remain constant. Simulation results were conducted in FEKO to decide the necessary spacing for the parasitic elements and also analyze the effect of the element heights on the radiation pattern. Next, a proof-of-concept

antenna was built and tested, comparing the experimental results to the simulation results. It was found from this comparison that the built antenna performed very similar to the expected simulation results. Last, some applications for this antenna are discussed.

4.2 Parasitic Antenna Array Simulation

Utilizing the electromagnetic modeling software FEKO, antenna patterns for a 4-element parasitic antenna array with a single monopole exciter in the center (Fig. 4.1) was analyzed. This antenna functions very similar to a Yagi-Uda antenna, but in two dimensions. In all of the upcoming simulations, the parasitic element at 45° was kept at a height of 0 mm and the frequency of interest was the GPS L1 band (1575.42 MHz).

In Fig. 4.2a, as the spacing, d, of the parasitic elements from the active monopole changes, the overall maximum gain does not drastically change, but there is a significant impact to the nulls created at about 90° and 180° and the size of the backlobe at −135°. These nulls are due to the destructive interference created by the parasitic elements re-radiating the energy of the active monopole. Fig. 4.2b shows when the spacing between the parasitic elements and the active monopole antenna

are kept constant, but the height, h, of the parasitic elements changes, there is a large change in the radiation pattern. The most noticeable change is at a parasitic element height of $h = 65$ mm: there is a large null at -90 and 180 degrees, however at a parasitic element height of $h = 45$ mm, there is a large null at 45 degrees. When the parasitic element is longer than $\frac{\lambda}{4}$, it acts as a reflector [133], but when it is shorter than $\frac{\lambda}{4}$, it acts as a director [133]. This matches the function of the Yagi-Uda antenna that uses a reflector height larger than the active element height and a director height smaller than that active element height. In this case, since the design frequency is 1575.42 MHz, a quarter-wavelength is about 47.57 mm.

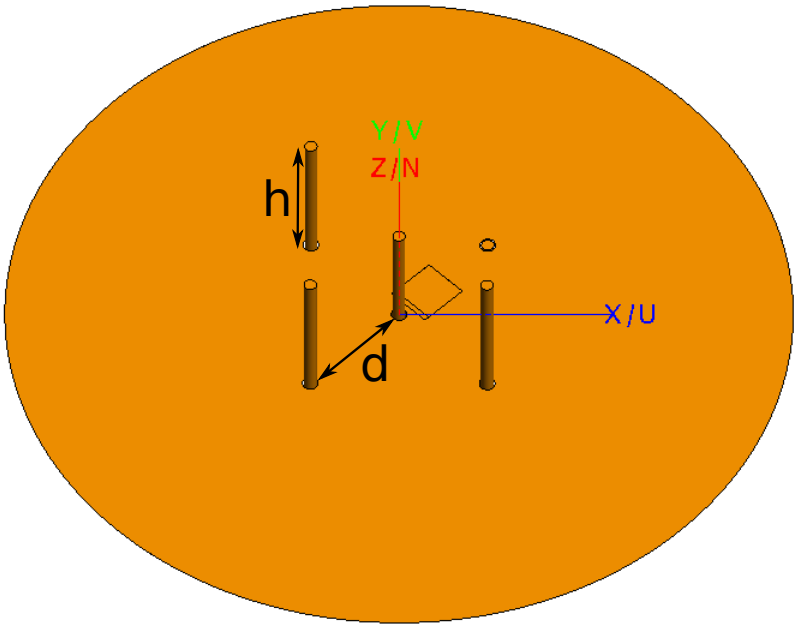

Figure 4.1: Simulation Model for Array of Four Parasitic Elements (Center - Driven Element)

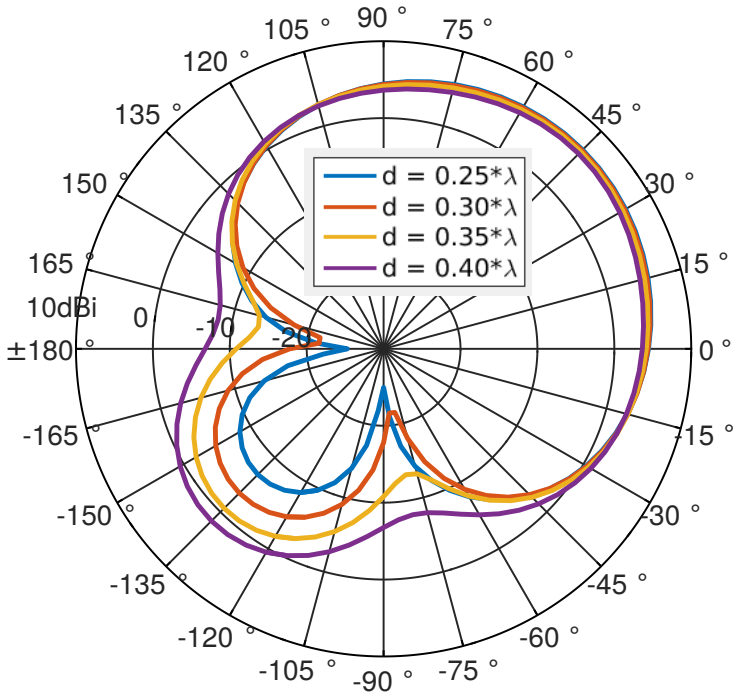

(a) Simulation Results for Array of 4-Element Parasitic - Element Heights of 65 mm at L1 Frequency

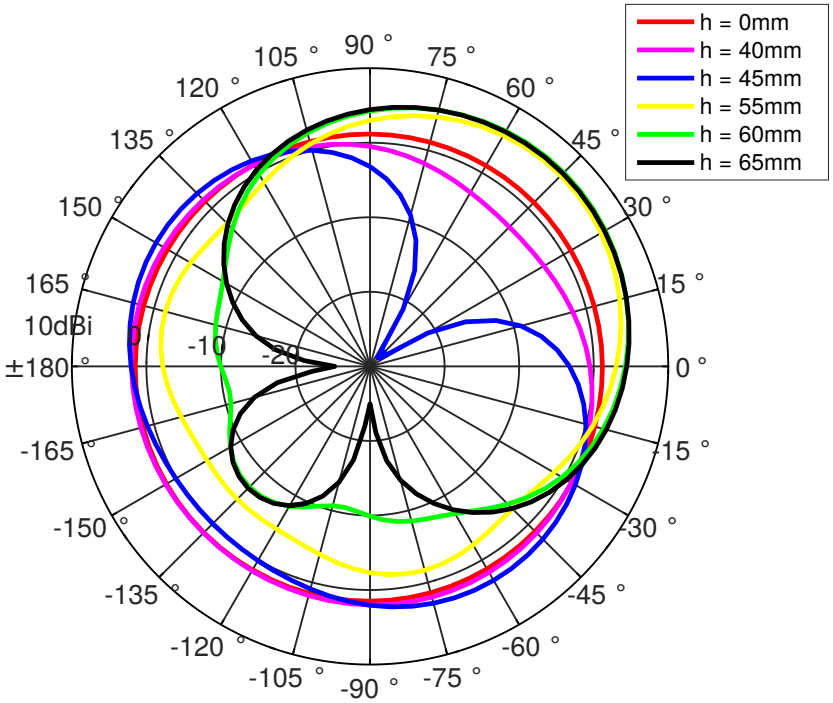

(b) Simulation Results for Array of 4-Element Parasitic Array - Spacing of $\frac{\lambda}{4}$ at L1 Frequency

Figure 4.2: 4-Element Parasitic Array Simulation Results at L1 Frequency (Elements Located at 135°, −135°, and −45°)

After the 4-element parasitic array, simulations were performed with a 16-element parasitic array (Fig. 4.3a). More parasitic elements in the antenna allows for greater control over the specific directions the user can steer the maximum gain and the nulls. Fig. 4.3b shows the radiation patterns created if the height is either $h = 45$ mm or $h = 65$ mm at two different possible setups. From the symmetry of the antenna, it is possible to get the same pattern in 22.5° increments.

Changing spacings between individual parasitic elements and spacings between the parasitic elements and the active monopole could be used for specific purposes. As mentioned above, it was decided to use a $\frac{\lambda}{4}$ spacing for this particular setup because it offers the deepest nulls and lowest backlobe while maintaining symmetry. As discussed in [131], concentric rings of parasitic elements could be utilized to increase the user's control over the radiation pattern of the antenna. Deeper nulls, lower side and back lobes may be achieved by designing a non-uniform structure, however the trade-off would be gaining more control in one azimuthal direction and giving up some control in other azimuthal directions. Also, with a non-uniform structure, the non-recurring expense goes up because more optimization of the system is needed, as well as the recurring expense because that system will need to be re-optimized for different use cases. So with a more specialized setup, the performance of the antenna will go up but at the price of optimization.

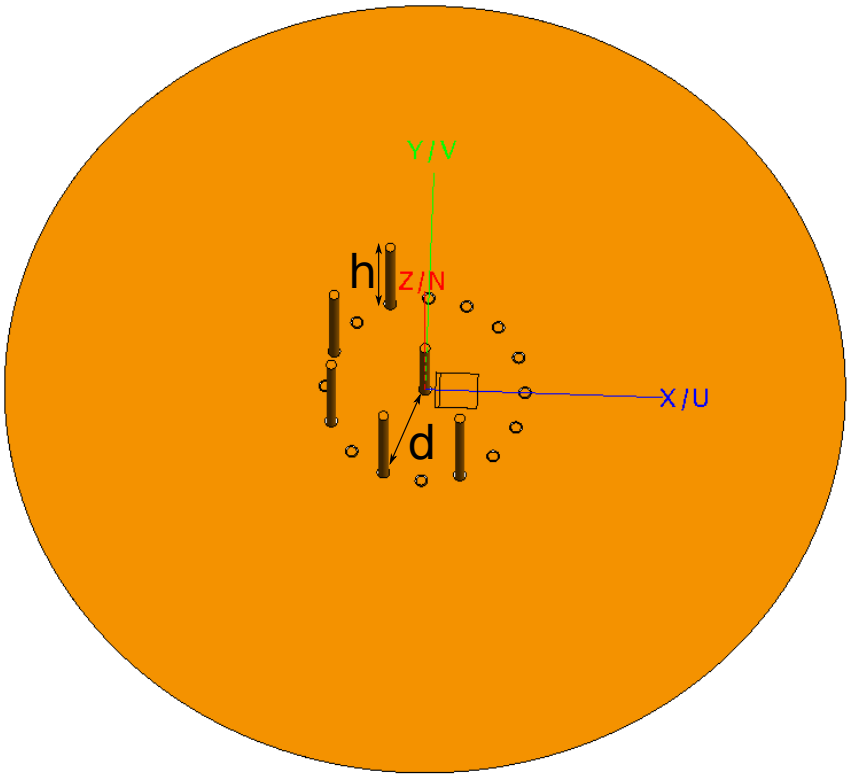

(a) Simulation Model for Array of 16 Parasitic Elements (Center - Driven Element)

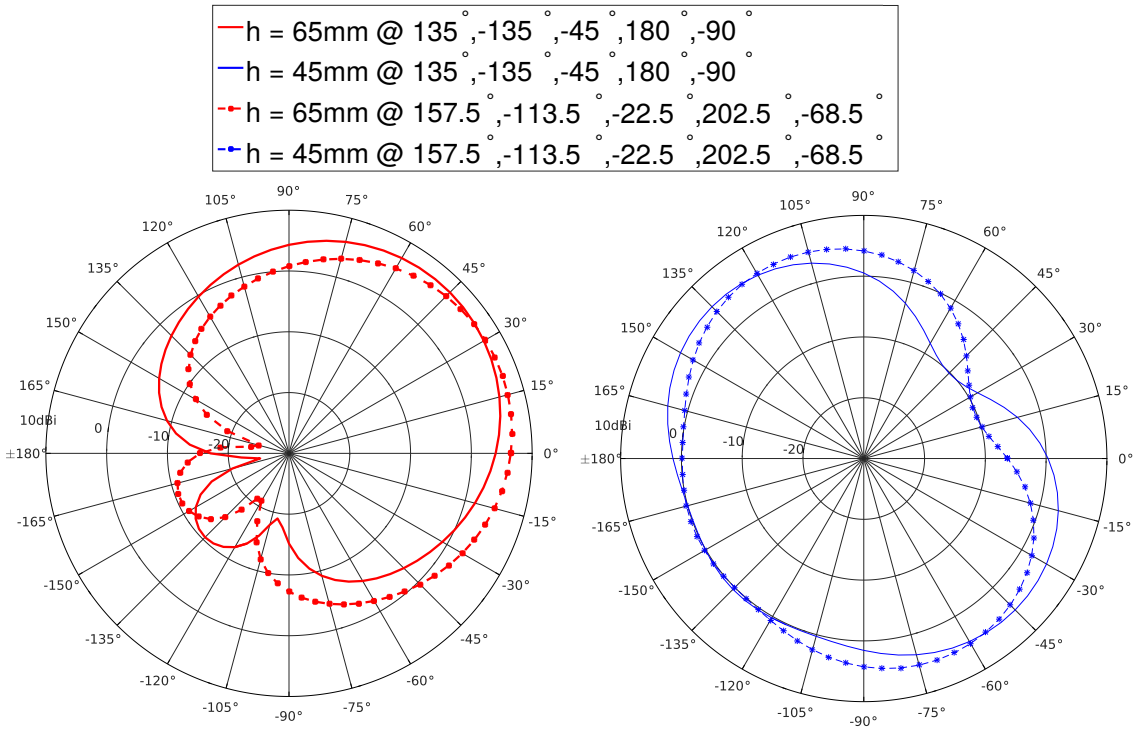

(b) Simulation Results for Array of 16 Parasitic Element Spacing of $\frac{\lambda}{4}$ with Marginal Change in Programmed Pattern Direction

Figure 4.3: 16-Element Parasitic Array at L1 Frequency

4.3 Experimental Framework

A proof-of-concept two-dimensional liquid-metal antenna array was built using oxygen tubing to hold the liquid metal and then was connected to a hex standoff with a rubber band to hold the tubing straight (Fig. 4.4a). To minimize the amount of space used by this antenna, the L2 and L5 frequency bands were combined to use the same parasitic elements. These elements were spaced at $\frac{\lambda}{4}$ where λ corresponds to the arithmetic mean of L2 (1.22760 GHz) and L5 (1.17645 GHz) at L2/L5 (1.20203 GHz). Under the ground plane, the oxygen tubing was connected to a valve that allows the user to decide which element gets injected with liquid metal to become parasitic and also how much to decide between a reflector or director (Fig. 4.4b). The center active element was electrically fed using the offset feed method described in Chapter 3. A syringe was used to inject or retract metal from each of the elements to create the desired effect (director or reflector). The effect of the NaOH, used to counteract the formation of an oxidation layer, must also be accounted. As described in Chapter 3, the NaOH is an electrolyte with a limited (but noticeable) conductivity. As long as this NaOH layer on top of each element is kept minimal, it will have limited effect on the antenna performance.

Since all of these simulations used the offset feed method described in Chapter

3, there is a length of liquid metal below the ground plane before the valve begins. This length of metal has a large effect on the radiation pattern of the antenna. The simulations shown in Figs. 4.5a-4.5c were done with 0 mm, 30 mm and 35 mm of liquid metal below the ground plane at L1, L2 and L5 frequency bands to see the effects. For the same frequency, the length of metal above the ground plane was kept constant. As can be seen from these plots, as the length of metal below the ground plane increases, the radiation pattern changes drastically, and can even change from directing the energy to reflecting the energ, as seen in Fig. 4.5a. In the prototype antenna, 35 mm of excess metal was below the ground plane so this has to be considered when changing the antenna from being a director to a reflector.

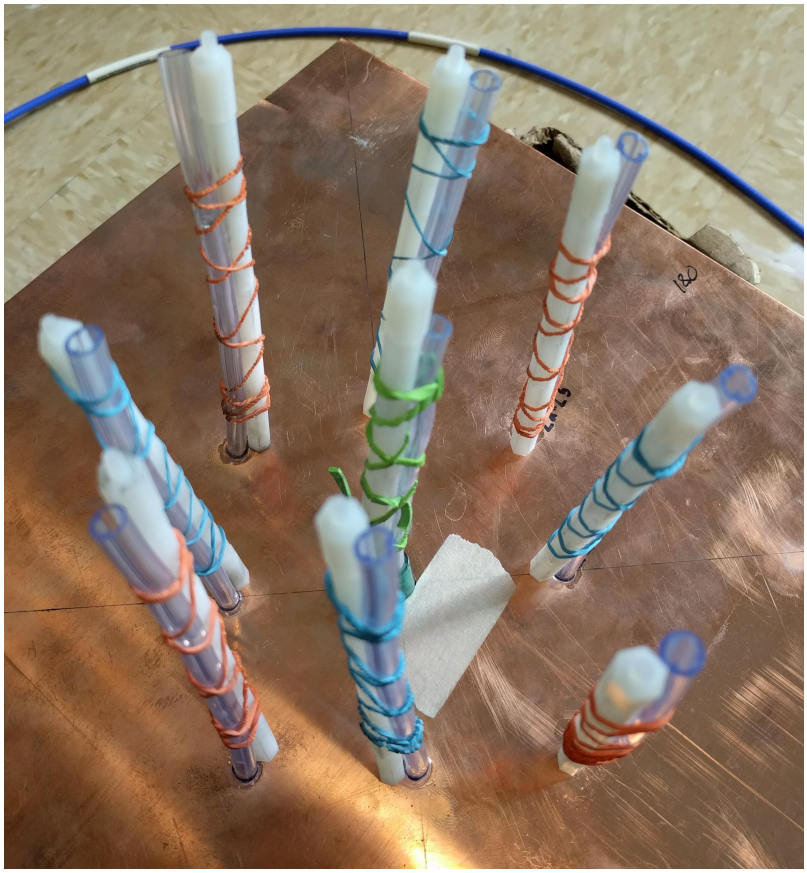

(a) Top View of Four-Element Parasitic Antenna Array (Green Rubber Band - Actively Fed Element; Blue Rubber Band - L1 Parasitic Elements; Orange Rubber Band - L2/L5 Parasitic Elements)

(b) Mechanical and Electrical Feed of Antenna Array

Figure 4.4: Four-Element Parasitic Monopole Array Prototype for L1, L2 and L5 GPS Bands

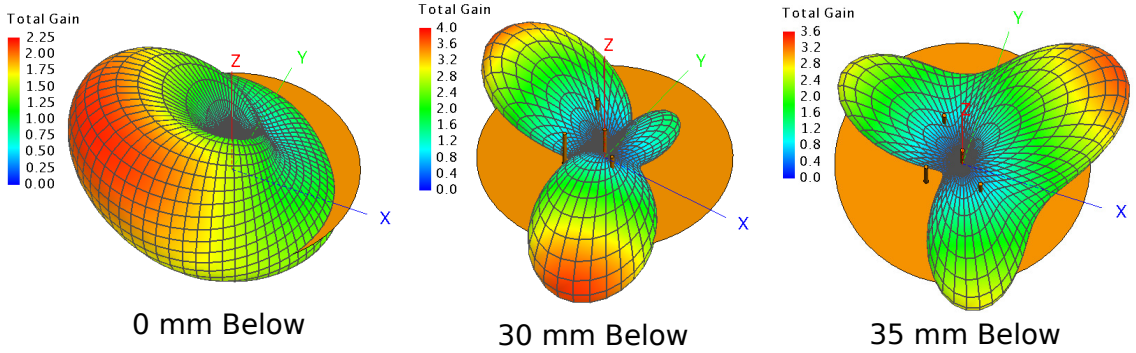

(a) L1 (1.57542 GHz) - Director Height of 50 mm

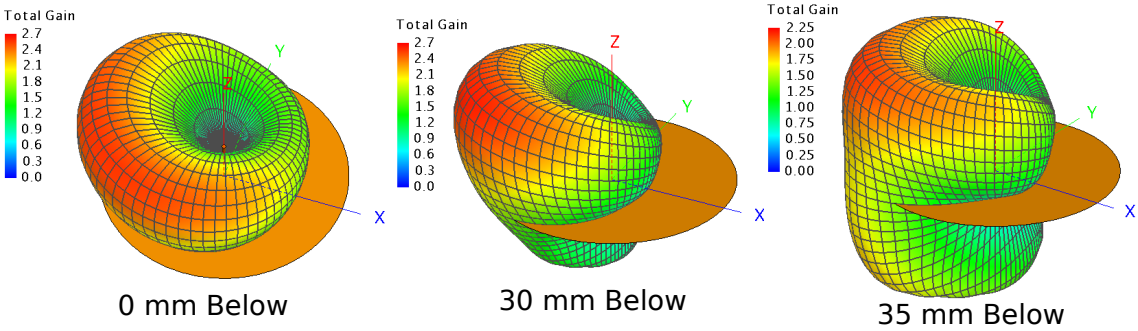

(b) L2 (1.22760 GHz) - Director Height of 60 mm

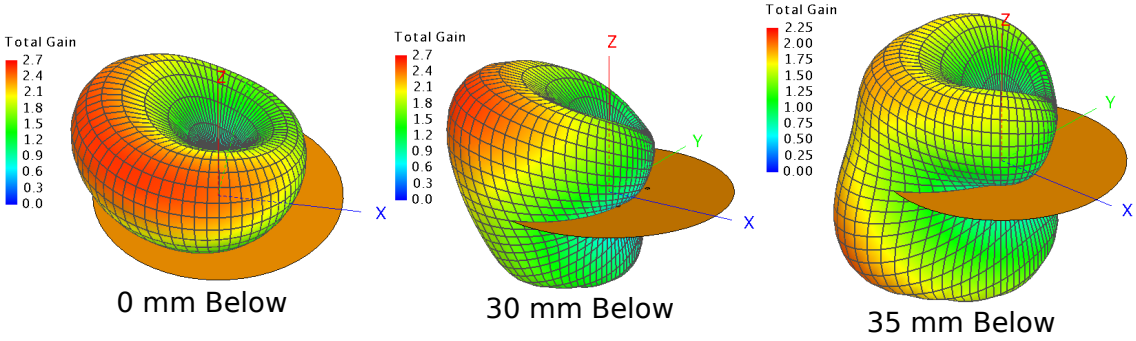

(c) L5 (1.17645 GHz) - Director Height of 65 mm

Figure 4.5: 4-Element Parasitic Array Simulation Results - Effect of Different Below Ground Feed Lengths

4.4 Experimental Results

Figs. 4.6-4.11 display simulation versus experimental measurements. The experimental measurements were taken in 10° steps using a power sensor connected to a log-periodic antenna. Figs. 4.6, 4.8, and 4.10 show that using this antenna as a director does not create a large gain in the direction of the directors, but it does create a large null of about -10 to -20 dBi in the opposite direction according to the simulations. These nulls were seen in the prototype antenna, however the nulls were not as deep as the simulation results, believed partially due to the limitations of the power sensor used for measurements; the noise floor of the sensor was higher than the minimum of the null. As expected, the null created for the L1 frequency is deeper than those for the L2 and L5 frequencies because the parasitic elements are not spaced at exactly $\frac{\lambda}{4}$ for either of the frequencies. Figs. 4.7, 4.9, and 4.11 show that using this antenna as a reflector creates a decent main lobe gain in the desired direction of about $7 - 8$ dBi with a backlobe of around -5 dBi. Experimentally, the height, in millimeters, of the parasitic elements for a director at L1, L2 and L5 frequencies were 35, 45, and 45 respectively and 45, 60, and 60 respectively for a reflector. In the FEKO simulations, the height, in millimeters, of the parasitic elements for a director at L1, L2 and L5 frequencies were around 45, 65, and 70 respectively and around 60, 75, and 85, respectively, for a reflector. This difference is believed to be due

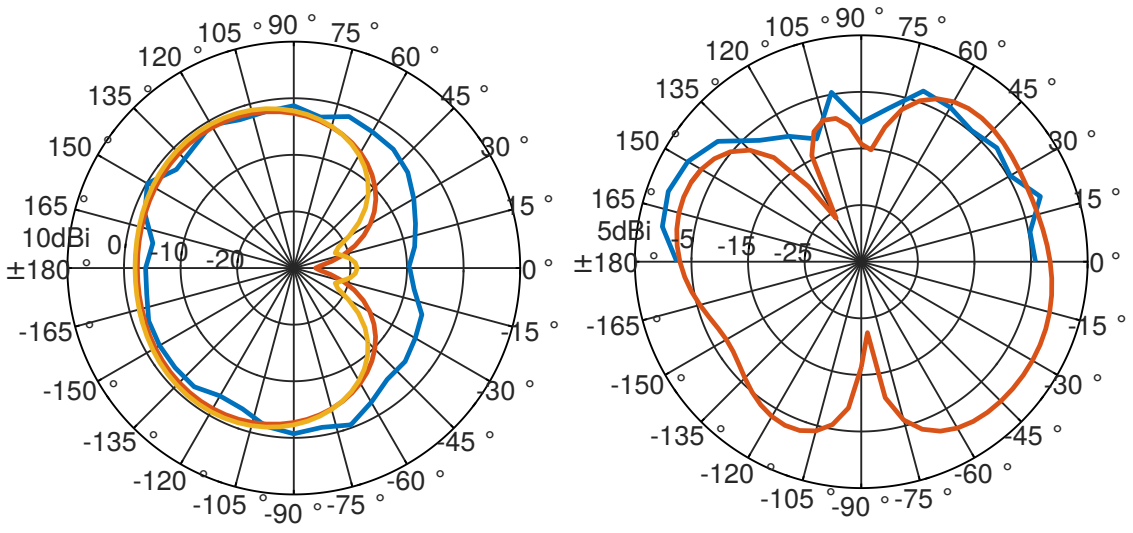

Figure 4.6: Experimental (Blue) vs. Simulation Results for L1 Frequency Director (Left: Azimuth Taken at 0°; Right: Elevation Taken at 0°)

to the conductivity of the liquid metal used in the experiments, however the trend of adjusting the height of the parasitic elements by 10 to 15 mm between director and reflector was seen in all cases. Since the nulls of the experimental antenna are not as deep as those from the simulation, it was difficult to definitely compare the experimental result to one simulation curve. Therefore, the azimuthal plots show multiple simulation curves with different parasitic element heights to find the best match for the experimental results. Fig. 4.12 shows the return loss of the monopole antenna while all the parasitic elements are empty. This figure shows the electrical feed method used matches the monopole very well to 50 Ω. There are two blue curves in the figure because this measurement was taken twice to show repeatability.

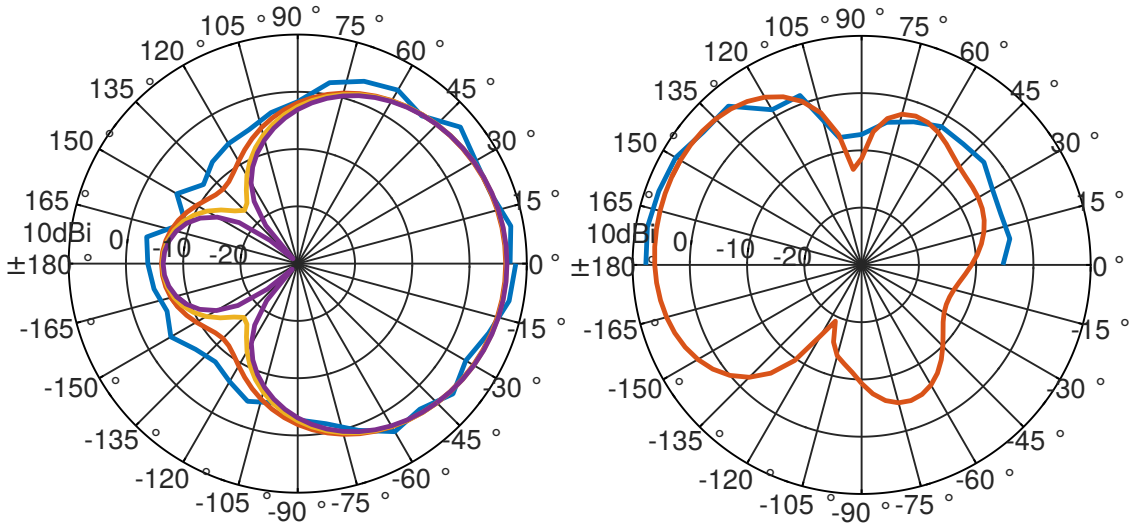

Figure 4.7: Experimental (Blue) vs. Simulation Results for L1 Frequency Reflector (Left: Azimuth Taken at 30°; Right: Elevation Taken at 0°)

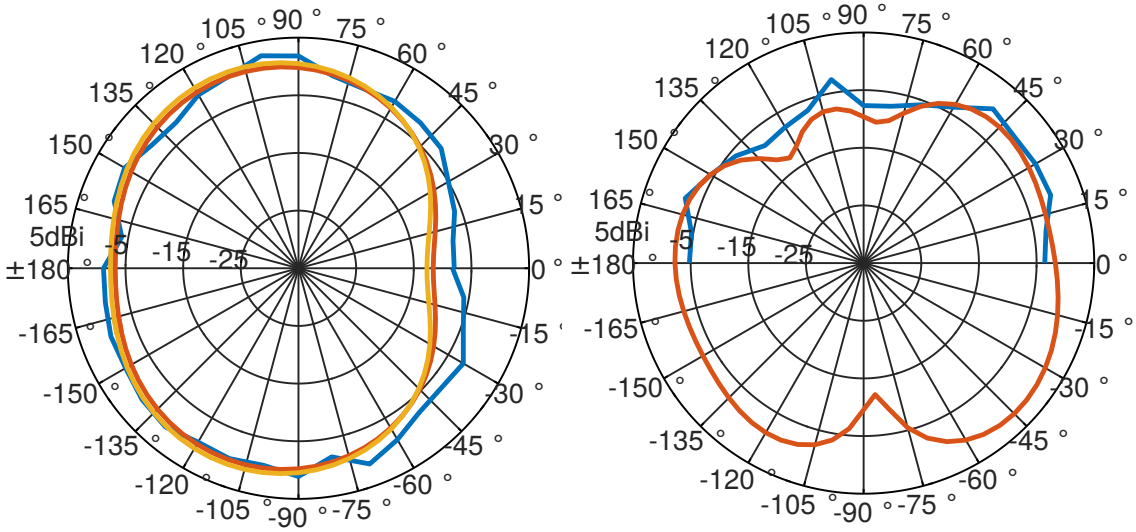

Figure 4.8: Experimental (Blue) vs. Simulation Results for L2 Frequency Director (Left: Azimuth Taken at 0°; Right: Elevation Taken at 0°)

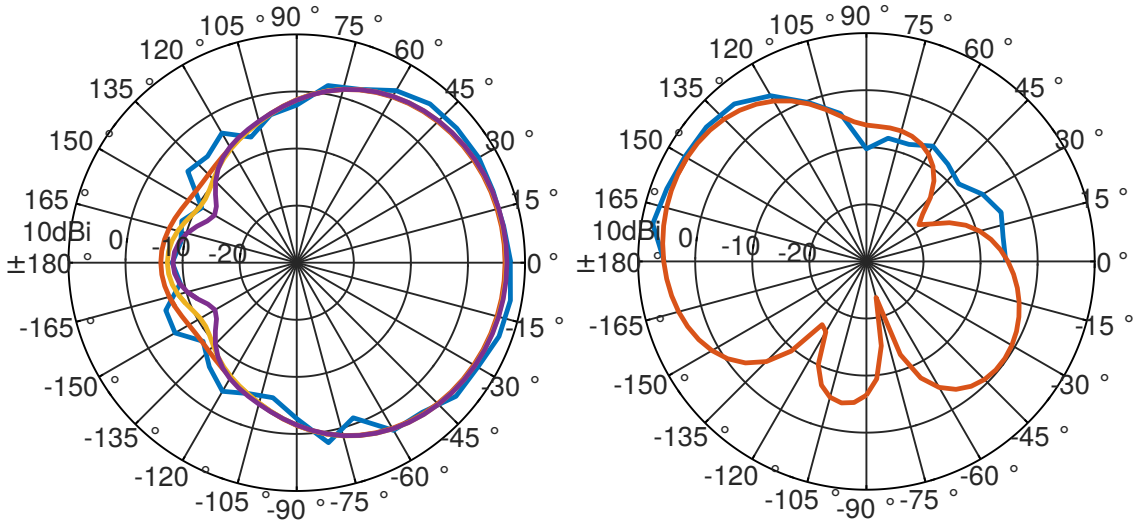

Figure 4.9: Experimental (Blue) vs. Simulation Results for L2 Frequency Reflector (Left: Azimuth Taken at 30°; Right: Elevation Taken at 0°)

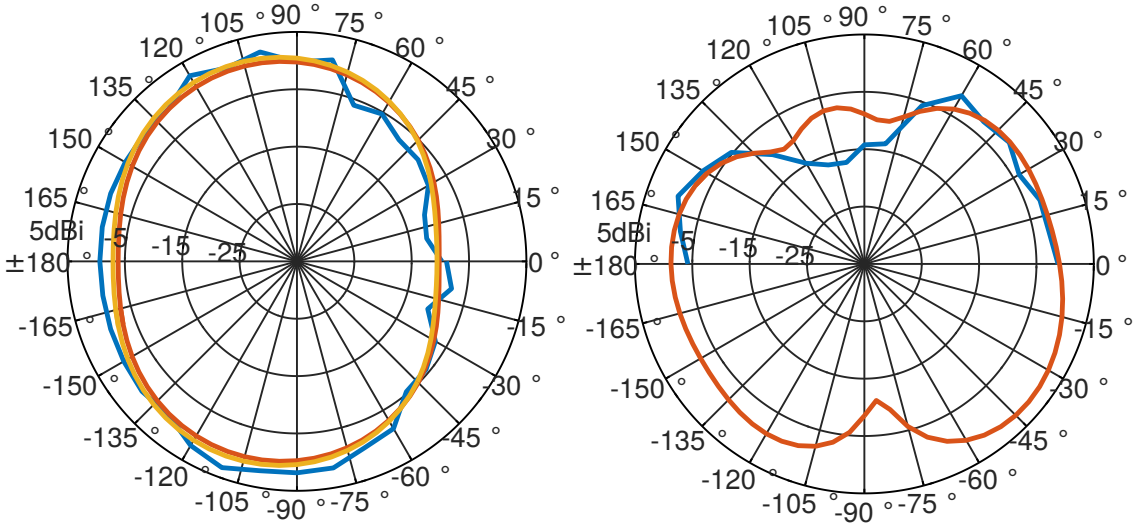

Figure 4.10: Experimental (Blue) vs. Simulation Results for L5 Frequency Director (Left: Azimuth Taken at 0°; Right: Elevation Taken at 0°)

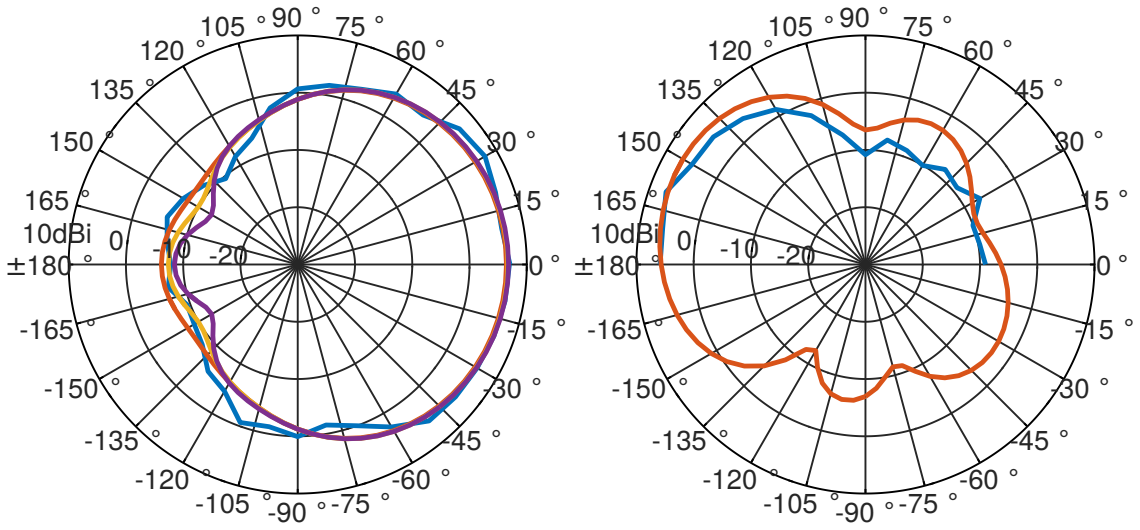

Figure 4.11: Experimental (Blue) vs. Simulation Results for L5 Frequency Reflector (Left: Azimuth Taken at 30°; Right: Elevation Taken at 0°)

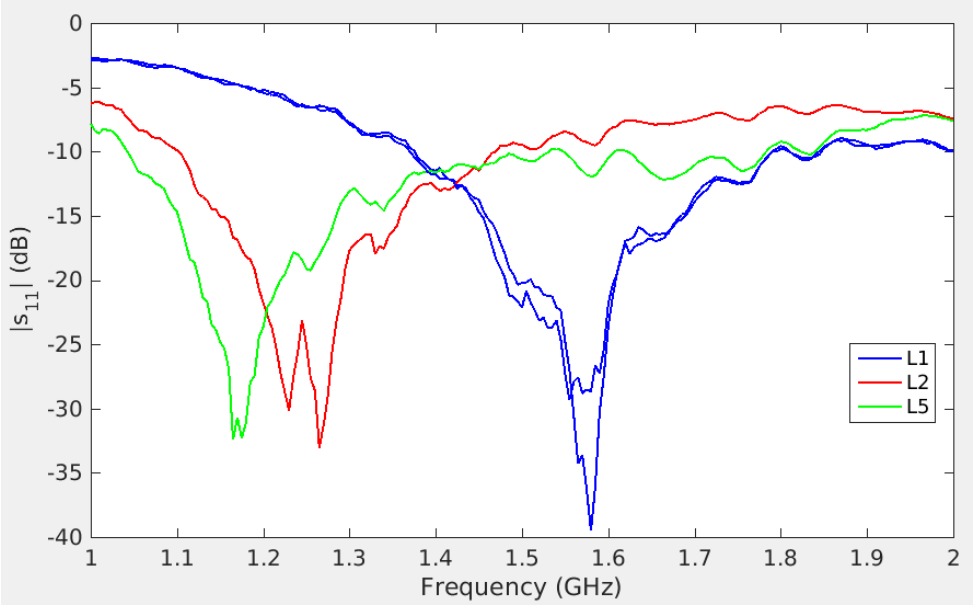

Figure 4.12: Experimental (Blue) vs. Simulation Results for L1 Frequency Director (Left: Azimuth Taken at 0°; Right: Elevation Taken at 0°)

4.5 Applications

One application where this technology could be utilized is in anti-jam Global Navigation Satellite Systems (GNSS), where the simultaneous tracking of multiple satellites benefit from the controlled directonality of an antenna (optionally combined with digital phasing) pattern and nulls. This parasitic element array allows the user control over the direction of the beam and the direction of the nulls. This ability could be used to null out interfering signals for any instantaneously chosen set of direction, and may be adapted over time. Based on the simulations, utilizing the capabilities of liquid metal allow the user greater control over frequency and beam steering than their solid metal counterparts. The more parasitic elements that are added to the array, the finer control the user has in steering the beam. The feed method used for the simulations is the offset feed described in Chapter 3. This feed method allows the most versatility in injecting and retracting the liquid metal from the antenna while still maintaining performance.

4.6 Conclusion

This section described simulations done in FEKO and experimental results for a two dimensional array of parasitic elements. Based on the results, utilizing the

capabilities of liquid metal allow the user greater control over frequency and beam steering than their solid metal counterparts. The more parasitic elements that are added to the array, the finer control the user has in steering the beam. Utilizing the parasitic elements as reflectors gives a larger gain in the desired direction but using them as directors creates a larger null. The feed method used for the simulations is the offset feed described in Chapter 3. This feed method allows the most versatility in injecting and retracting the liquid metal from the antenna while still maintaining performance.

Chapter 5

Helical Antenna

The goal of this chapter is to expand on previously researched Eutectic Gallium-Indium (EGaIn) alloy liquid-metal antennas to create an antenna that can change both polarization and frequency to meet the user's needs. This concept is described through analytical models of helix antennas, simulations performed in FEKO, and measured results of a proof-of-concept dual frequency L-band GPS-focused hardware model. Although ongoing work is being performed to more efficiently feed this proof-of-concept liquid-metal antenna, the overall realized gain of the helix antennas aligned well with theoretical models.

5.1 Introduction

Some work has been done in creating an antenna using liquid metal that can change polarization [136], but dipoles are limited in directionality. The aim of this chapter is to describe a highly directional helical antenna that can change both the polarization and frequency of the antenna by deciding where the liquid metal is injected from a shared reservoir. The two most common methods of creating reconfigurable antennas include the use of microelectromechanical switches (MEMS) or PIN diodes to perform the adaptations. The disadvantage of using these methods are the coupling effects of the unused antenna components if the switches are open and these methods only provide discrete adaptations, while the use of liquid metals can perform continuous adaptations. It has been shown that it is possible to do frequency and/or polarization changes using switches on patch antennas [137,138], but these are all discrete changes, without the ability to continuously adapt to the environment.

Some other work has been done with creating reconfigurable helix antennas including using shape memory alloys [139], creating a deployable helix [140], creating a reconfigurable helix based on an origami structure [141], or using liquid metal embedded in polydimethylsiloxane (PDMS) to allow flexibility [142]. The main difference between the previously researched liquid-metal helix antenna and the

proposed liquid metal helix antenna is the ability to change frequency as well as polarization and retract the metal from the antenna. The helix described in [142], has the liquid metal enclosed in PDMS, which does not allow for the injection or retraction of the metal once set. They use a gear to twist the helix and change it between circular polarizations but the frequency of the helix remains constant.

The National Oceanic and Atmospheric Administration (NOAA) satellites commonly use antennas with circular polarization because they are in constant motion [143]. This motion would cause a linearly polarized satellite antenna to be constantly changing polarization with respect to a linearly polarized ground station antenna. This means the ground station antenna must either be linearly polarized and accept the 3 dB loss along with it or be right hand circularly polarized. While U.S. spacecrafts are RHC polarized, Chinese and Russian satellites vary between right hand and left hand circular polarization [143]. Also, in NASA's Tracking and Data Relay Satellites (TDRS), there is a mix of RHC, LHC and linearly polarized antennas [144]. Therefore an antenna system that can change its polarization can have multiple uses without the cross-polarization losses.

GNSS systems use RHC polarization to combat multipath. This means GPS receivers use either RHC helix antennas or linearly polarized patch antennas when connecting with these satellites. Most inexpensive receivers use a linearly polarized

patch antenna because of lower costs but will have an extra 3 dB loss due to the polarization mismatch loss. Having the ability to switch between polarizations gives the system the capacity to function in many different environments and to be multi-purpose. One of the main benefits of this antenna design is the ability to have two or more antennas within a shared volume, giving the system more control without sacrificing space. This makes a highly adaptable antenna only consume a small amount of space while maintaining the performance of its solid metal counterparts. Manufacturing this type of antenna could be low-cost because antenna can possibly be 3D printed and the same liquid metal used in this antenna can be re-used for any other 3D printed liquid-metal antenna.

This chapter describes the experimental framework of the proof-of-concept helices that were built, including the feed structure used, the pitch angle and circumference of each helix. Some additional work on improving the feed structure is also suggested. Next, experimental results of the proof-of-concept helix are presented and compared with simulation results created in FEKO. Last, some applications of this antenna and how to improve its technical readiness level (TRL) are suggested.

5.2 Background

A helix antenna is a basic traveling wave antenna consisting of a wire wound in a helical shape. The geometry of the antenna is layed out in Fig. 5.1 and the governing equations are listed below (Eqns 5.1-5.9). When the pitch angle $\alpha = 0°$, the helix becomes a loop antenna with N turns; when the pitch angle approaches $\alpha = 90°$, the helix antenna becomes a linear wire antenna. The radiation characteristic of the antenna is dependent on the circumference of the antenna, changing from normal to axial modes (Fig. 5.2). In normal mode, the maximum radiated field is in the direction normal to the helix axis, similar to the radiated field of a dipole antenna. To achieve this mode, the dimensions of the helix must be small compared to the wavelength with $L_w \ll \lambda_0$. To achieve axial mode with circular polarization, the diameter D and the spacing S must be larger compared to the wavelength at $\frac{3}{4}\lambda_0 \leq C \leq \frac{4}{3}\lambda_0$ and a spacing of $S \simeq \frac{\lambda_0}{4}$ [12]. The pitch angle is usually $12° \leq \alpha \leq 14°$ for optimal performance [12] but maintains increased directivity over a larger range of about $5° \leq \alpha \leq 20°$ [13].

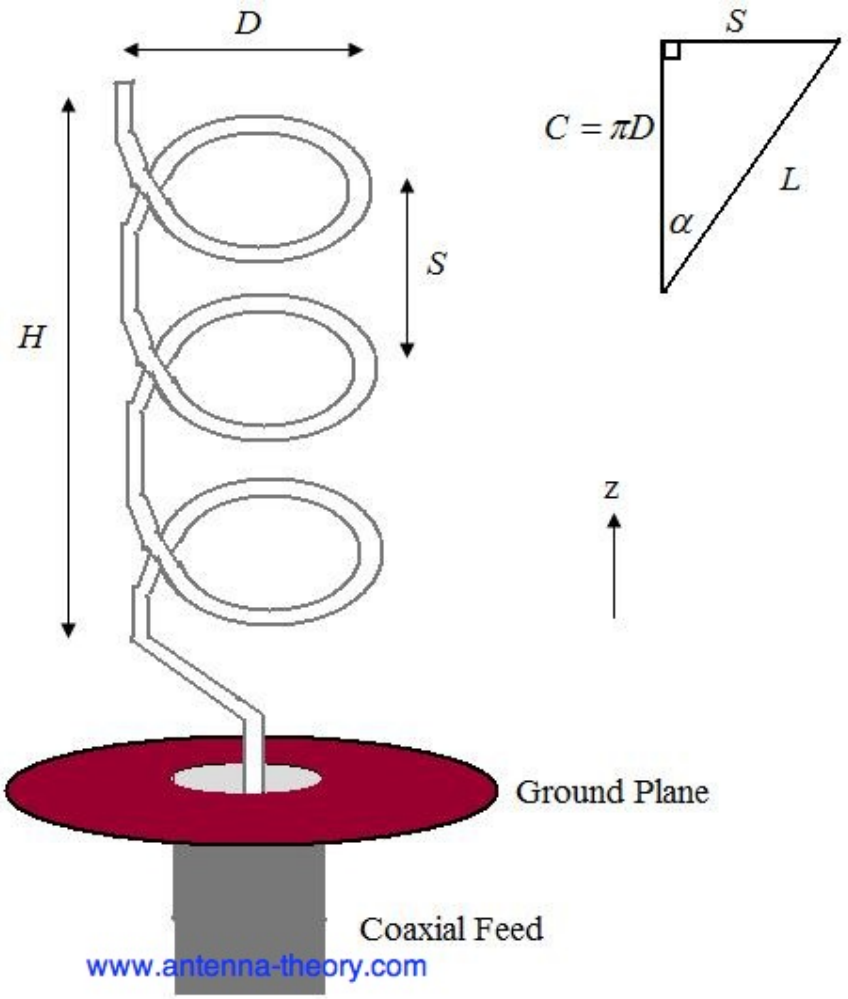

Figure 5.1: Geometry of a Helix Antenna [20]

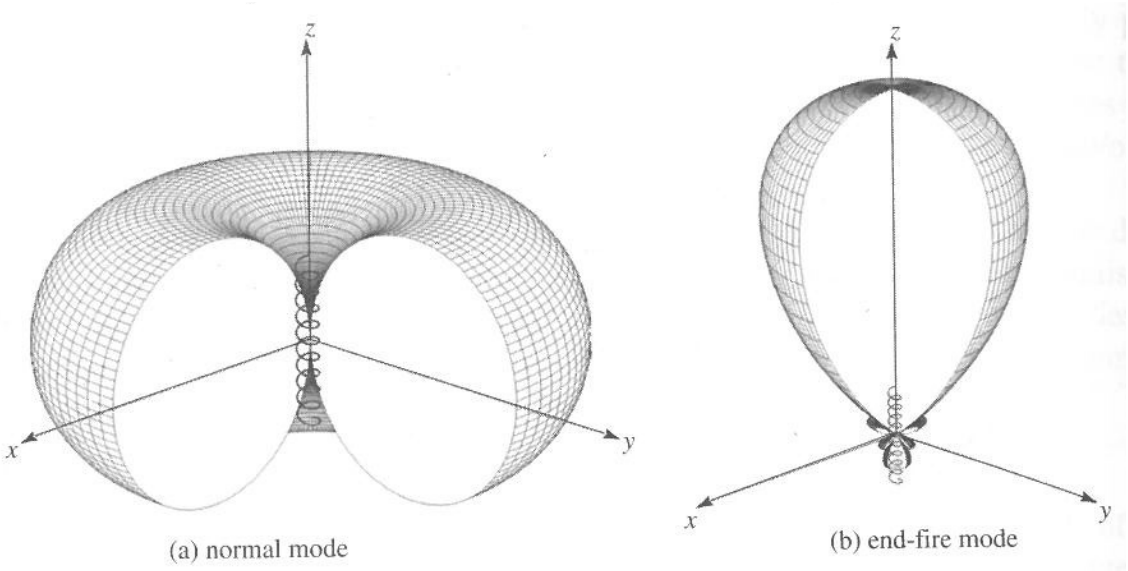

Figure 5.2: Helical Antenna Normal and End-Fire Mode Radiation Patterns [12]

Governing equations:

$$D = \text{ diameter of helix} \tag{5.1}$$

$$C = \text{ circumference of helix } = \pi D \tag{5.2}$$

$$S = \text{ vertical spacing between turns } = C\tan(\alpha) \tag{5.3}$$

$$\alpha = \text{ pitch angle } = \tan^{-1}\left(\frac{S}{C}\right) \tag{5.4}$$

$$L = \text{ length of one turn } = \sqrt{C^2 + S^2} \tag{5.5}$$

$$N = \text{ number of turns} \tag{5.6}$$

$$L_w = \text{ length of helix coil } = NL \tag{5.7}$$

$$h = \text{ height } = \text{ axial length } = NS \tag{5.8}$$

$$d = \text{ diameter of helix conductor} \tag{5.9}$$

Some design equations were also created based on a large number of empirical measurements [12].

$$\text{Input Impedance: } R \simeq 140\frac{C}{\lambda_0} \tag{5.10}$$

$$\text{Half-Power Beamwidth: HPBW (deg)} \simeq \frac{52\lambda_0^{3/2}}{C\sqrt{NS}} \tag{5.11}$$

$$\text{Beamwidth Between Nulls: FNBW (deg)} \simeq \frac{115\lambda_0^{3/2}}{C\sqrt{NS}} \tag{5.12}$$

$$\text{Directivity: } D_0 \simeq 15N\frac{C^2 S}{\lambda_0^3} \tag{5.13}$$

$$\text{Axial Ratio: } AR = \frac{2N+1}{2N} \tag{5.14}$$

Where the axial ratio (AR) is the ratio of the magnitudes of E_θ and E_ϕ. When $AR = 0$, $E_\theta = 0$ and the radiation is linearly polarized horizontally meaning the helix acts a loop. Also, when $AR = \infty$, $E_\phi = 0$ and the radiation is linearly polarized vertically meaning the helix acts a dipole. Lastly, when $AR = 1$, the radiation energy is perfectly circularly polarized with the magnitudes of E_θ and E_ϕ being equal. With a circularly polarized antenna, half the signal is lost when communicating with a linearly polarized antenna (loss of 3 dB). There are also two types of circular polarization, left-handed and right-handed. In right-handed circular polarization, the electric field is rotating clockwise from the point of view of the source and the opposite direction for left-handed circular polarization. If the transmit antenna is left-handed circularly polarized, but the receive antenna is right-handed circularly polarized, theoretically none of the signal will be received by the receive antenna. In reality, most circularly polarized antennas are not perfectly circular, instead having more of an elliptical shape. This means in the case previously described with two opposite circularly polarized antennas for transmit or receive, a high loss of about -20 dB [145–147], but not perfect loss, should be expected. Helical antennas are commonly used for satellite communication because the antenna on the satellite can transmit linearly polarized waves from any orientation and the helix antenna will receive the signal with only a 3 dB loss at all times.

With having the helix antenna be made from liquid metal, this allows the user to be able to change frequency or polarization depending on how the system is designed. Since the main variable behind operating frequency of the helix antenna is the circumference, this mean the antenna system can be designed to have multiple mechanical feeds for liquid metal with concentric circles of helices. This allows the flexibility for the user to decide which helix to inject metal into to change the operating frequency of the system while still keeping everything compact. In this chapter, the primary method of changing frequencies or polarization is by switching mechanical feeds to inject metal into a different helix. Since these helix channels are normally empty unless injected with liquid metal, they do not interfere with each other aside from the small parasitic effects of the electrical feeds. Another method for changing frequencies is to be able to change the helix circumference by expanding the tubing with the liquid metal already inside it. By doing this, the pitch angle or number of turns of the helix will be changed slightly, but this should have minimal effect on the performance of the antenna; the main limiting factor to using this method would be the electrical feed of the antenna. This idea of physically changing the tubing could then be extended further, with a reversal of the coil direction to implement a polarization change.

Simulation work was first performed in FEKO to verify the radiation pattern

of the helix was adequate using the pitch angle, number of turns and the feed method described above. Since the decided pitch angle of 5° is not optimal for a helix, the simulation work showed the gain of the helix was acceptable to start building the proof-of-concept antenna. These simulation results are then compared to experimental results obtained from the proof-of-concept helix antenna that was built.

5.3 Experimental Framework

The terminal impedance of a helix antenna is typically around 100 Ω to 200 Ω [12], with $Z_{in} = 140$ if $C = \lambda_0$ [12]. The most common way to feed a helical antenna is using a quarter-wave stub matching feed to bring the input impedance closer to 50 Ω [12]. The proof-of-concept liquid-metal helix antennas used the same offset feed as the monopole antenna, this time the offset feed acting as part of the quarter wave stub (Fig. 5.3d). To get a perfect match for each of the feeds, more length of metal was needed in-between the SMA pin and the beginning of the helix, but the L-brackets used did not allow for this extra metal. Therefore, the helices are not perfectly matched and the return loss suffers from the mismatch. An RLC matching network could be used in place of the quarter-wave stub to match the impedance of the helix to 50 Ohms. Since a well made helix is generally close to having a purely real input impedance, an L pad with resistors could be used to perform the impedance transformation.

Since the circumference of the helix can be between $\frac{3}{4}\lambda_0 \leq C \leq \frac{4}{3}\lambda_0$, the L2 (1.22760 GHz) and L5 (1.17645 GHz) frequencies were averaged to 1.20203 GHz (L2/L5). One helix was made for L1 and the second helix was made for L2/L5 but was operated at L2 or L5 frequencies separately. The chosen pitch angle for both

the L1 and L2/L5 helix was 5° because this pitch angle allowed for a more compact antenna without sacrificing the gain of the antenna. It was decided to use 5 turns of the helix because this gave the best simulation performance, while still keeping the antenna height minimal. When building the antennas, it was decided to make one of them right hand circularly (RHC) polarized and the other left hand circularly (LHC) polarized. This antenna is designed to be able to have both the L1 and L2/L5 helices have both a RHC and LHC polarized antenna, making the system have four possible antennas within the same volume. This allows the user the ability to not only switch between frequencies but also switch polarization for the need at hand. If a flexible material is used to contain the liquid metal, it would be possible to change the frequency or polarization of the helix antenna by "unrolling" the antenna. This method could be used to change the frequency of the antenna by changing the circumference of the helix. It could also be used to change the polarization if the helix is turned enough to wind the other direction.

The helix itself is also made from the same oxygen tubing as the monopole antennas. At first, two nylon hex standoffs were going to be used to hold the helix in place by zip-tying the tubing to the hex standoff at the correct height. This method did not work and the pressure the tubing exerted on the standoffs prevented them from being glued to the copper ground plane. Instead, to hold the proof-of-concept

helix shape, small (16 oz.) and large (40 oz.) plastic peanut butter jars were used as physical guides because they have the right diameter for a L1 and L2/L5 helix. The top of each jar was removed to allow for easy access from both sides of the jar. Next, the spacing of each turn within the helix was measured out on the jar so it would be easy to hold the tubing in place at the correct heights. Little slits were made in the side of the jars with an X-ACTO knife (one above and one below the tubing) and zip ties were fed through the slits to hold the tubing in place (Fig. 5.3a). Additional adjustments to this proof-of-concept hardware model were made to avoid pinching the tubing at the base of the ground plane, leading to a 20 mm standoff distance from the ground plane. Each of these design elements could be instrumented more precisely for a higher TRL product, with various additive manufacturing techniques being applicable. Figure 5.3c is a good visualization of how to prevent the tubing from pinching using the jar lid, but this is more of a proof-of-concept solution. There are a few ways to fix this issue in a real product, including drilling out part of the ground plane so the tubing can rest at an angle, or increasing the pitch angle of the helix (but this will lead to a less compact antenna). If the antenna is 3D printed using additive manufacturing, this pinching effect would not be an issue.

(a) Side View of Dual Helix Prototype

(b) Top View of Dual Helix Prototype

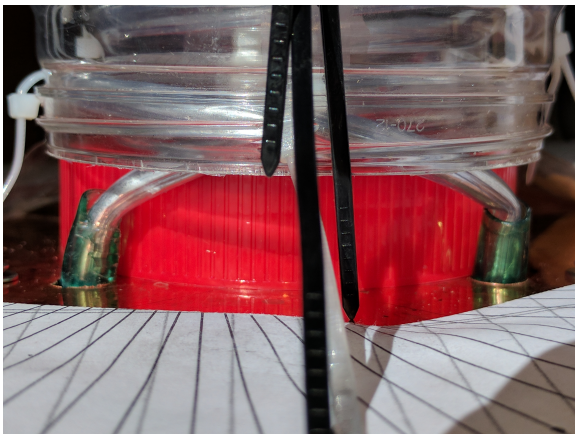

(c) Helix Raised Using Jar Cap to Prevent Tubing from Pinching

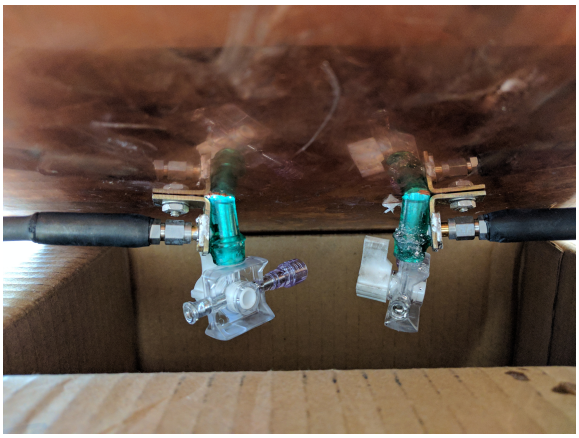

(d) Electrical Feed of Prototype Helix Antenna

Figure 5.3: Prototype Dual Helix

5.4 Experimental Results

As mentioned before, a helix antenna usually uses a quarter wave stub as an impedance converter to match the antenna to the electrical feed. In this case, the excess metal below the ground plane from the feed method used acted as part of this quarter-wave match but was not long enough for the frequencies of interest. Fig. 5.4 displays the return loss of both helix antennas along with the simulation results for the return loss. The L1 helix antenna had a decent return loss of about -10 dB at L1. The L2/L5 helix did not have a great return loss with about -5 dB at L2 and -6 dB at L5. This could be improved by adding a matching circuit to the feed or designing the feed to have a quarter-wave stub that acts as an impedance match. Correctly designing this feed would give the helix a much better return loss and a higher Q (Fig. 5.6). Fig. 5.5 shows the coupling between the two helix antennas if metal is injected into both helices. This shows that there is a coupling between the two antennas of about -20 dB meaning it might be possible to use one helix as transmit and one as receive at the same time.

Figs. 5.7-5.12 show the far field radiation pattern of the proof-of-concept helix antennas using a log-periodic antenna as the test antenna in 10 degree increments. Figs. 5.7-5.9 show the radiation pattern of the helices if only the helix for the desired

frequency is filled with metal. Figs. 5.10-5.12 show the radiation pattern of the helices if both the helices are filled with metal but only the helix appropriate for the desired frequency is electrically fed. Since a helix is inherently circularly polarized, but the experimental data was taken using a linearly polarized antenna, both the vertical (blue) and horizontal (red) polarization data for each helix was taken but changing the orientation of the test antenna. In the plots below, 3 dB was added to the gain of the experimental data to make up for the loss between linear and circular polarization and is displayed using a dashed line. With the 3 dB loss added to the gain of each helix, the liquid-metal helix antennas achieved about 10–11 dB of realized gain.

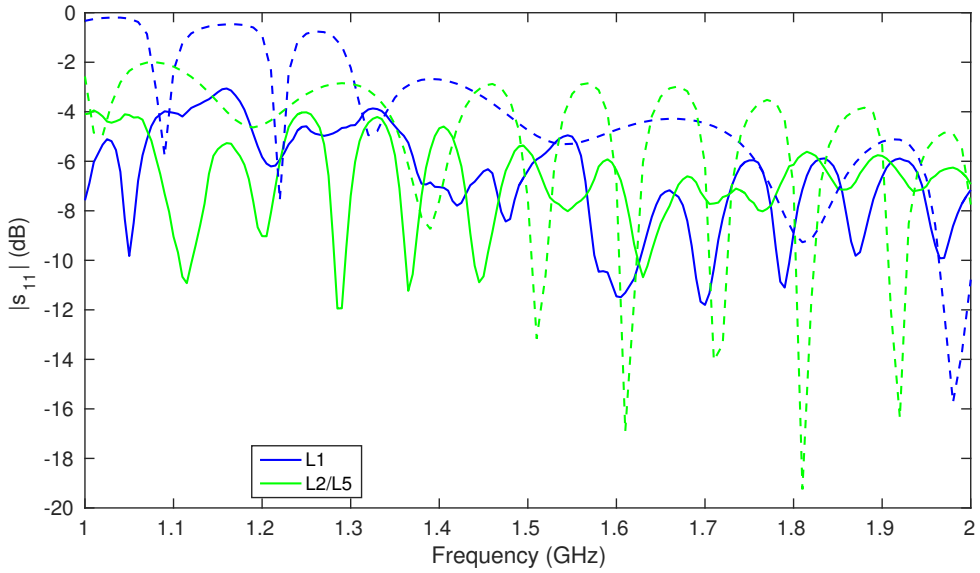

Figure 5.4: Return Loss of Prototype Helix Antenna (Blue: L1; Green: L2/L5) (Dashed Line: Simulation; Solid Line: Experimental)

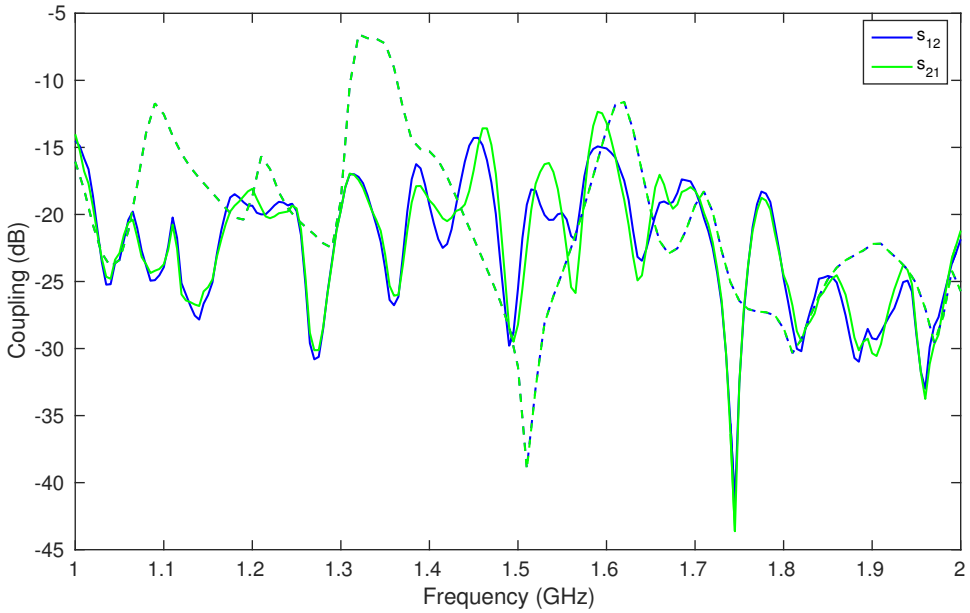

Figure 5.5: Coupling Between Prototype Helix Antennas (Dashed Line: Simulation; Solid Line: Experimental)

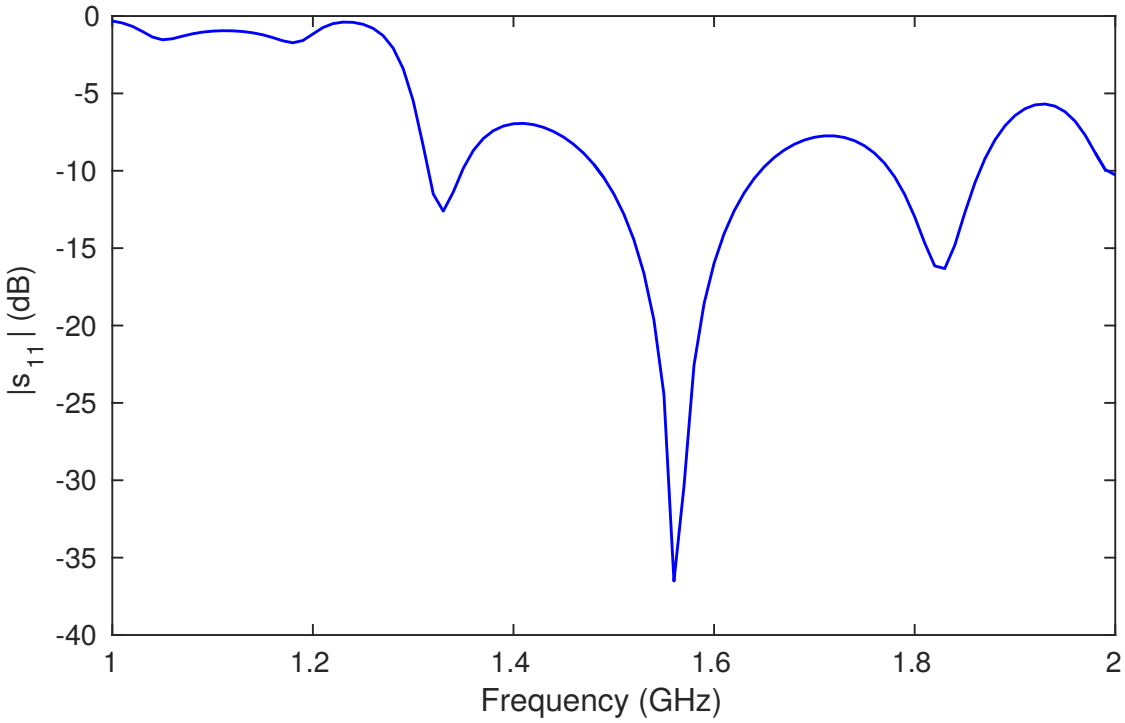

Figure 5.6: Simulated Return Loss of L1 Helix Antenna with Quarter-Wave Stub Feed

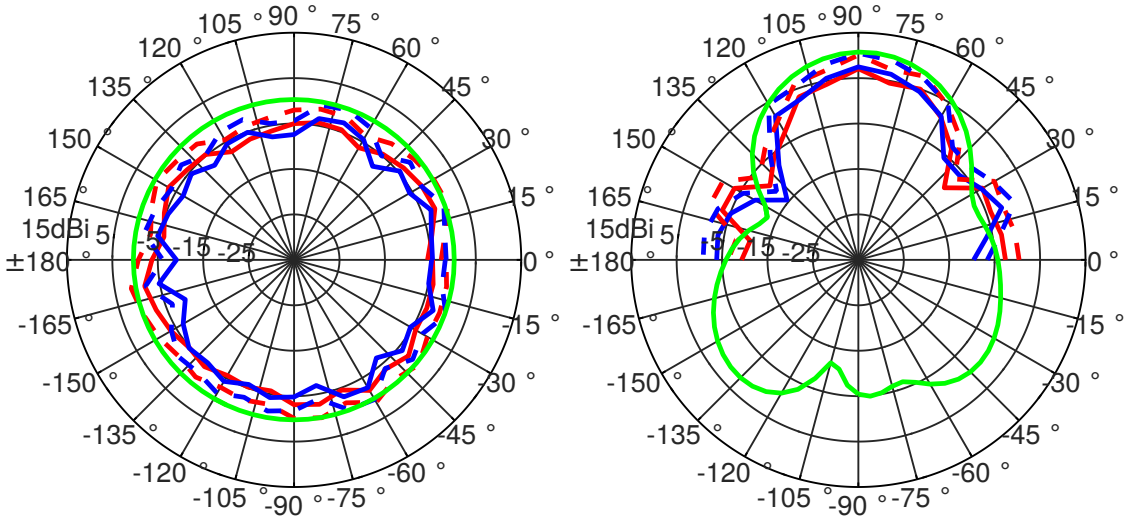

Figure 5.7: L1 Prototype Helix Antenna at L1 Frequency (Left: Azimuth; Right: Elevation) (Green: Simulation; Blue: Vertical Polarization; Red: Horizontal Polarization; Dashed: Assuming 3 dB Loss)

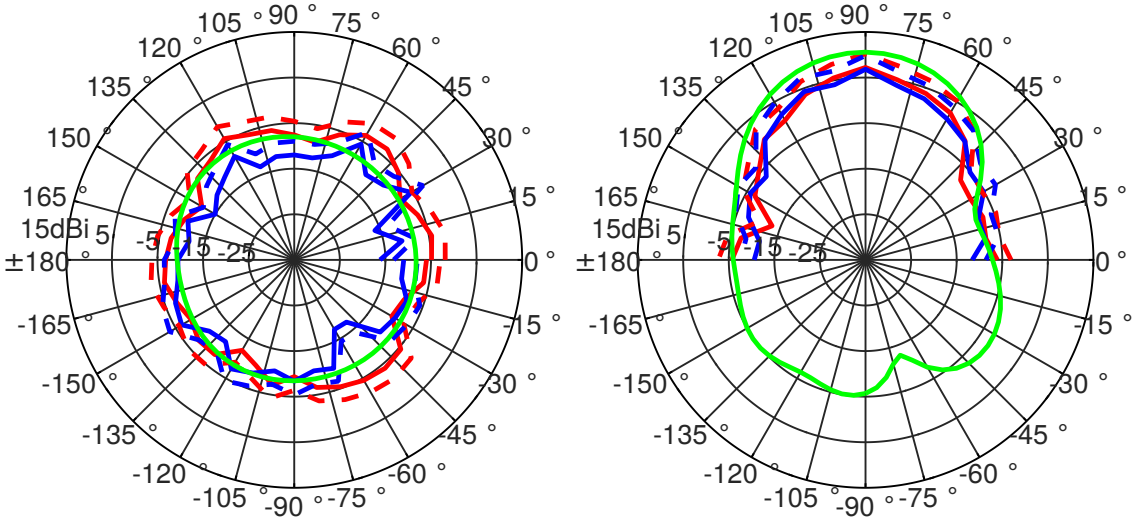

Figure 5.8: L2/L5 Prototype Helix Antenna at L2 Frequency (Left: Azimuth; Right: Elevation) (Green: Simulation; Blue: Vertical Polarization; Red: Horizontal Polarization; Dashed: assuming 3 dB Loss)

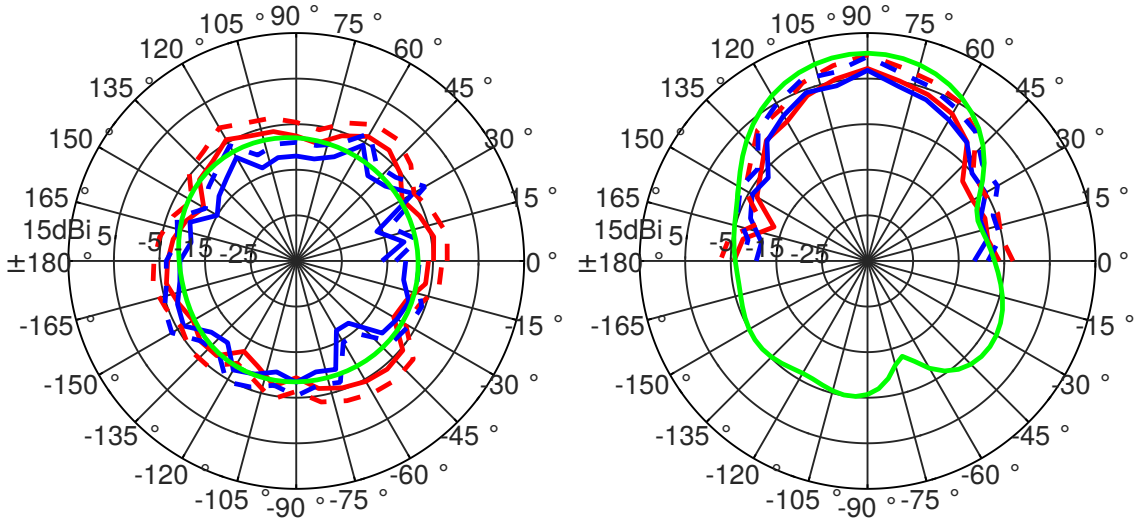

Figure 5.9: L2/L5 Prototype Helix Antenna at L5 Frequency (Left: Azimuth; Right: Elevation) (Green: Simulation; Blue: Vertical Polarization; Red: Horizontal Polarization; Dashed: Assuming 3 dB Loss)

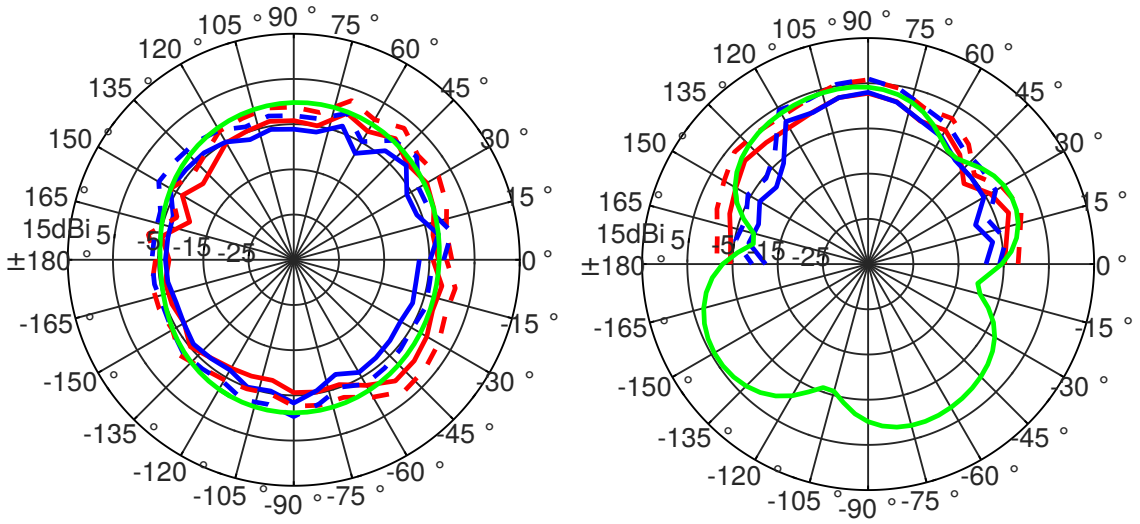

Figure 5.10: Both L1 and L2/L5 prototype Helix Antenna with L1 Helix Run at L1 Frequency (Left: Azimuth; Right: Elevation) (Green: Simulation; Blue: Vertical Polarization; Red: Horizontal Polarization; Dashed: Assuming 3 dB Loss)

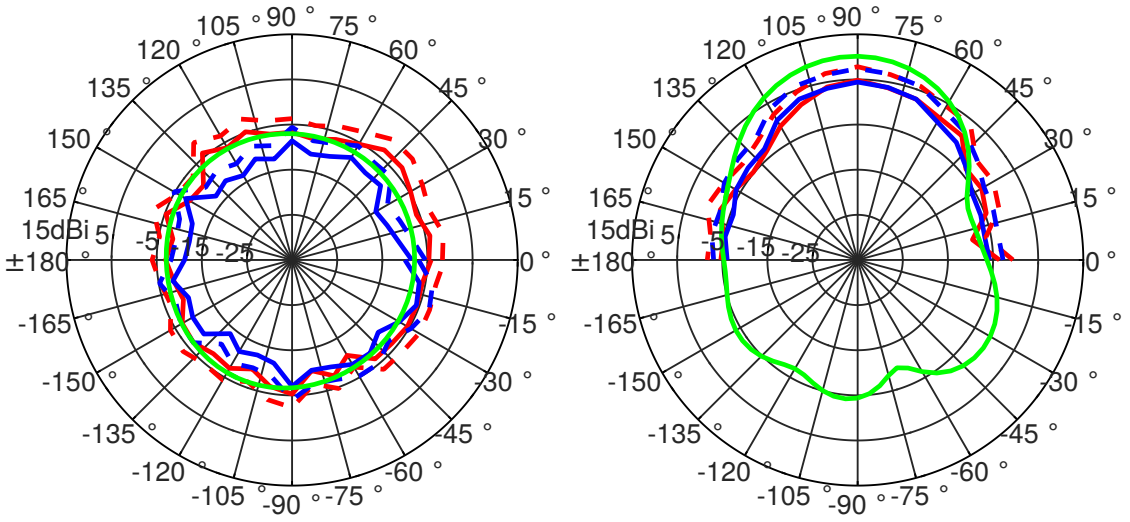

Figure 5.11: Both L1 and L2/L5 Prototype Helix Antenna with L2/L5 Helix Run at L2 Frequency (Left: Azimuth; Right: Elevation) (Green: Simulation; Blue: Vertical Polarization; Red: Horizontal Polarization; Dashed: Assuming 3 dB Loss)

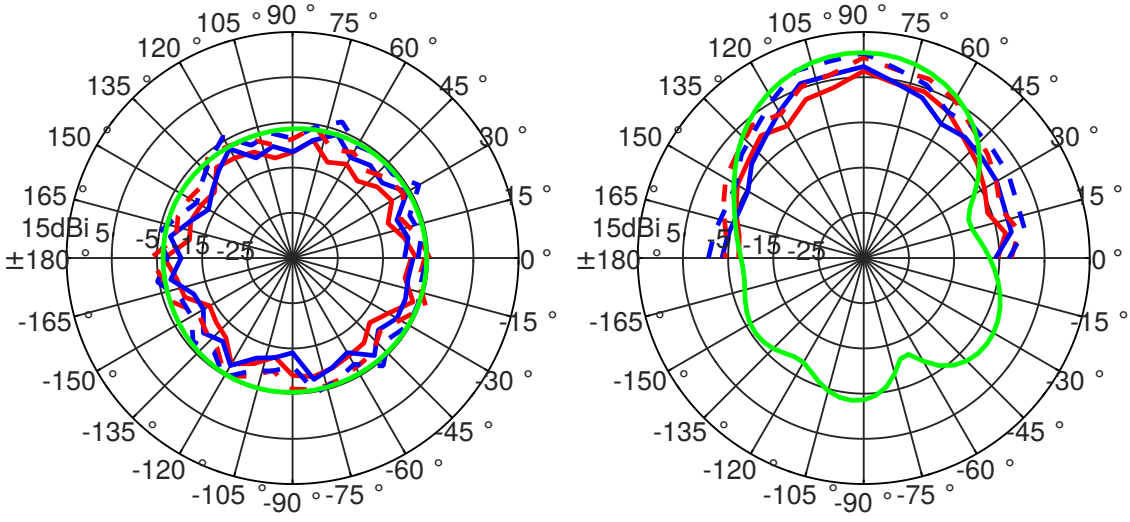

Figure 5.12: Both L1 and L2/L5 Prototype Helix Antenna with L2/L5 Helix Run at L5 Frequency (Left: Azimuth; Right: Elevation) (Green: Simulation; Blue: Vertical Polarization; Red: Horizontal Polarization; Dashed: Assuming 3 dB Loss)

5.5 Applications

Although this proof-of-concept antenna is admittedly low TRL, it does have a number of potential military relevant applications as the technology matures. One of the candidate applications for the proposed liquid-metal antennas is adaptable tactical SATCOM antennas. By enabling changes in polarization, a user may reuse the same antenna independent of orientation to the satellite, "programming" it to match the desired polarization after fielding, and potentially gaining back some portion of the generally accepted 3 dB loss of a linearly polarized receive antenna. Additional work will be needed to construct more robust hardware prototypes, including instrumentation of a rotary hoop structure that enables more easily configurable frequencies for helix antennas.

5.6 Conclusion

This chapter described a directional helical antenna that can change both the polarization and frequency of the antenna by deciding where the liquid metal is injected. The overall gain of the helix antennas was about 11 dB (assuming 3 dB polarization loss in testing), which is decent considering the return loss of the helices was not optimal. With a better feed technique, such as using a matching circuit

or quarter-wave stub, the impedance mismatch of the antenna could be minimized while increasing the Q-factor. Also, the coupling between the two helix antennas was about 20 dB, meaning it might be possible to use them at the same time with one transmitting and the other receiving. Some future work to be done in this area to increase the TRL of this design would be to apply this design to additive manufacturing techniques. By using 3D printing, it is possible to have concentric circles of helical-shaped channels where the user decides which channel to fill with liquid metal to determine polarization and frequency. Another area of future research would be to mount this antenna on a rotary structure so the circumference of the helix could be wound or unwound to create a change in frequency. An adaptable feed would need to be implemented in this case to account for the frequency shifts.

Chapter 6

3D Printed Structures for Liquid-Metal Antenna Array

This chapter describes the simulation of a multi-element two-dimensional antenna array constructed of Eutectic Gallium-Indium (EGaIn) liquid metal components. This aggregate proof-of-concept system validates the use of liquid metal for highly adaptable antenna patterns that are configurable in frequency, directivity, gain or polarization strictly by changing the effective antenna lengths/liquid volume. Moreover, this adaptability is achieved within a single shared space, enabling system-relevant extensions via additive manufacturing and/or modular pre-formed antenna structures. Overall performance of this aggregated adaptive antenna system is shown to closely resemble that of distinct apertures, save for minimal parasitic

effects from the feed structures of non-utilized apertures.

6.1 Introduction

This chapter includes a proof-of-concept model for a 3D printed modular antenna array. Other methods for creating a modular antenna have been created such as with snap-on-buttons [148]. Most modular antenna designs utilize either antenna elements used as the building blocks for an array [149, 150] or a system allowing for interchangeable antennas that share a common feed design [151–153]. These other modular systems, made from solid metal conductors, do not have the benefit of having extra unused antenna components nearby without causing mutual coupling effects. Utilizing liquid metal as the conductor allows the system to have pieces in place that are not used at the moment but do not negatively effect the system performance as a whole, and then can have liquid metal injected into them when the need arises. This gives a liquid-metal modular antenna another degree of freedom over solid metal modular antennas because ususued pieces can be left in place for later use without any interference by retracting the liquid metal from these pieces. Many reconfigurable antennas utilize microelectromechanical system (MEMS)-based switches [61,64,65] or PIN diodes [50,51,55] to create the changes in the antenna. These methods can only create discrete adjustments in the antenna, however, and have a high non-recurring

expense because each antenna must be designed per application. The design cost of creating each of these reconfigurable antennas using switches is much higher than creating the independent modules that can be combined together to create the needed antenna. Moreover, the use of liquid antenna elements enables a continuous range of antenna values, further eliminating discretized lookup tables of allowed values. This suggested antenna array can be designed such that individual antenna pieces can be added or removed to fit the situation. The mechanical expense of designing the 3D model is higher than other antenna systems, but the expense of the system as a whole is lower because of the design cost of a single aggregate system with the parasitic always there. This type of modular system could be expanded to include much more complex antenna array systems once the appropriate feed is designed and the 3D CAD model is designed for printing.

This chapter first describes a modular antenna array consisting of four helix antennas, a monopole and eight parasitic elements that allow for high frequency adaptation, directivity/radiation pattern control and polarization changes. This system is designed to operate at all three GPS frequencies (L1, L2, and L5) and may have the ability to simultaneously receive at multiple bands at the same time with minimal coupling between elements. GPS frequencies were chosen for this antenna design because of the need to track satellites at known ephemeris as well as limiting

polarization mismatch between the satellite and ground antenna. This antenna system also has the ability to function as an anti-jam antenna because as well as being able to steer the main beam, it can steer nulls towards any unwanted or interfering signal. Next, simulation results performed in FEKO are described, showing the degradation of the antenna system compared to the individual components. Last, some applications and future work is discussed on how to mature this design into realizable hardware.

6.2 Antenna Array

Fig. 6.1 and Fig. 6.2 describe the setup of the antenna array. Around the edges are directors for the monopole at $\frac{\lambda}{4}L1$ (red) and $\frac{\lambda}{4}(L2/L5)$ (green). L2/L5 is defined as the arithmatic mean of the L2 (1.2276 GHz) and L5 (1.17645 GHz) GPS bands at 1.20203 GHz. The outer ring is comprised two helix antennas (one RHC polarization, one LHC polarization) optimized for the L2/L5 (black) frequency. It was decided to optimize this antenna for this frequency because it can function reasonably well at either L2 or L5 depending on the demand. The inner circle is comprised of two helix antennas optimized for the L1 (yellow) frequency band. Last, the blue cylinder in the center, is a monopole antenna that can function at any of the three bands depending on the amount of liquid metal injected, and therefore its height, into the

antenna. Each of the antennas uses the offset feed method described in Chapter 3. This antenna setup allows the user high adaptability in the polarization, frequency and directionality of the antenna all within the same shared volume.

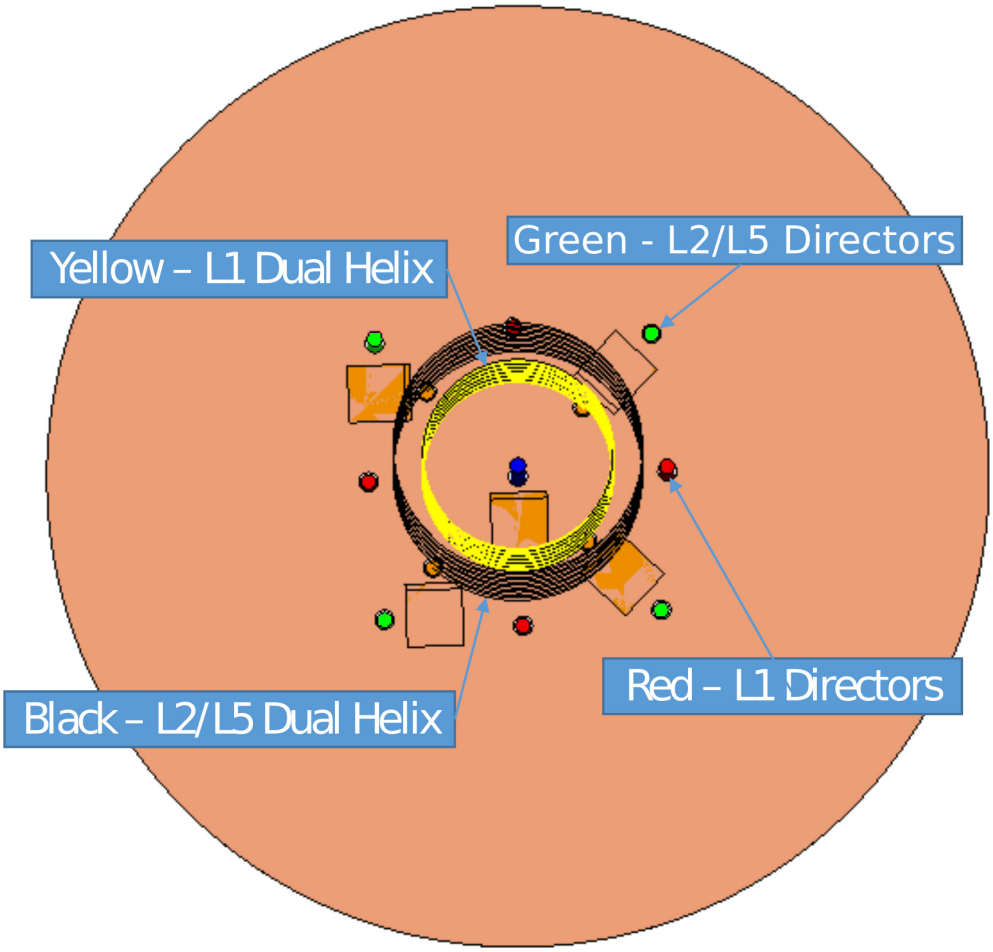

Figure 6.1: Simulation Model for Antenna Array - Top View

Fig. 6.3 displays a comparison of the antenna radiation pattern with the possible

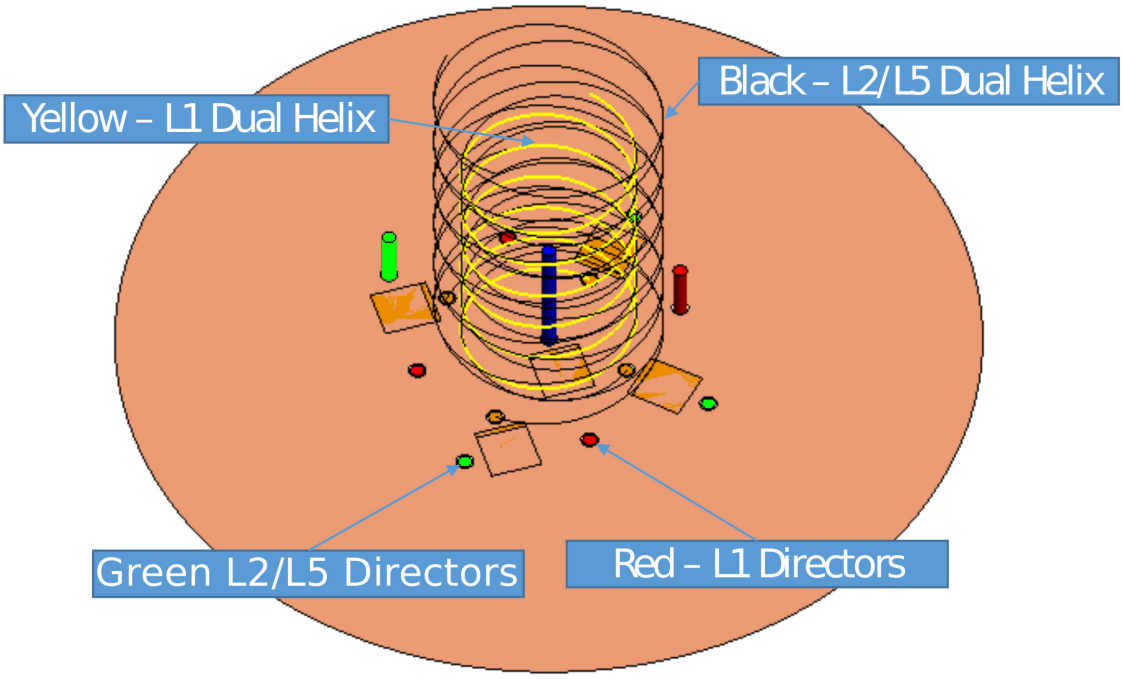

Figure 6.2: Simulation Model for Antenna Array - Side View

coupling factors of nearby non-active feeds and multiple holes in the ground plane to the antenna radiation pattern of the single antenna by itself. The antennas in the figure all display the degraded version of the antenna; the non-degraded version of the antenna does not have the holes in the ground plane nor the stubs of inert material below the ground plane for the antenna to couple onto. As we can see from these simulation results, there is not a large change between the full model with degradation from nearby residual feeds and the performance of the stand-alone

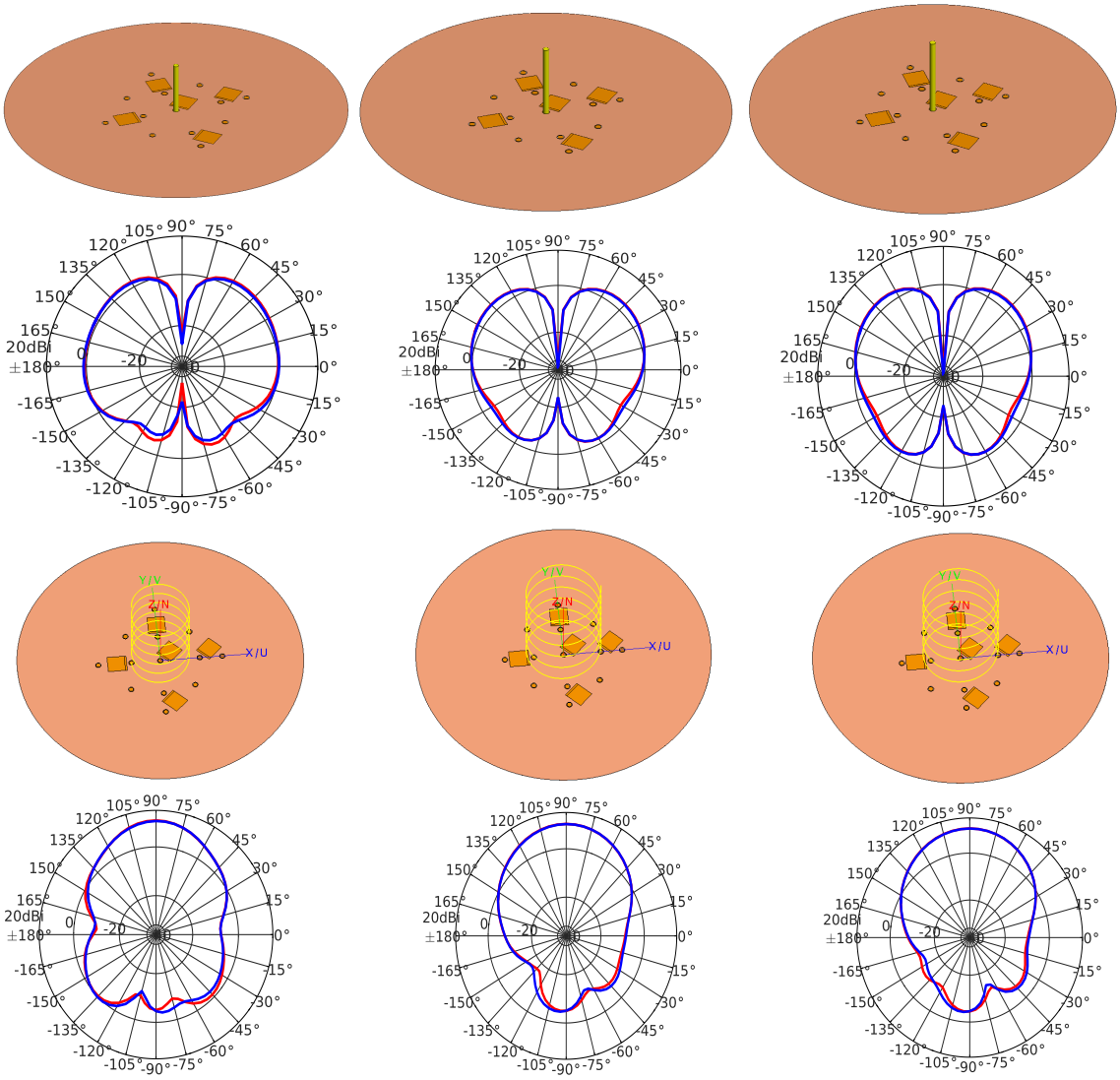

Figure 6.3: Simulation Degradation Results - From Left to Right (L1 Monopole, L2 Monopole, L5 Monopole, L1 Helix, L2 Helix, L5 Helix); Blue: Without Degradation; Red: With Degradation

antenna. Along with these radiation patterns, the directors can be used to control the direction of maximum gain or the nulls of the monopole antenna as described

in Chatper 4. By using a more complex passive element array, it is possible to have even more control over the directionality and nulls of the center monopole antenna [131].

Fig. 6.4 shows a simple diagram of the 3D printed model in which there is a monopole and four helix antennas (RHC and LHC polarization for each frequency). This 3D printed structure will allow a modular design in which the user can add or remove sections of the antenna at will depending on the need or space restraint. Not shown in this model are the directors for the monopole that could also be added in select locations. These directors could be printed using the same model as the center active monopole element for simplicity. Each piece of the antenna can be separated from the others, allowing the user to decide which type of antenna is needed. A locking mechanism could then be used to "lock" the antenna into place on top of the ground plane. Each of the pieces of the antenna are designed to fit snugly into each other to minimize space constraints and prevent extraneous movement. Fig. 6.5 and Fig. 6.6 show a 3D diagram of the antenna built in the CAD software 123D Design. Fig. 6.5 shows the outline of each of the objects, where the helix shape inside each cylinder is clearly visible. An additively manufactured 3D clear plastic model of this compact antenna is currently being built to validate these simulation results with realistic proof-of-concept hardware measurements. Fig. 6.7 and Fig. 6.8 show the 3D

printed antenna structure that was additively printed by the AOE 3D print lab at Virginia Tech.

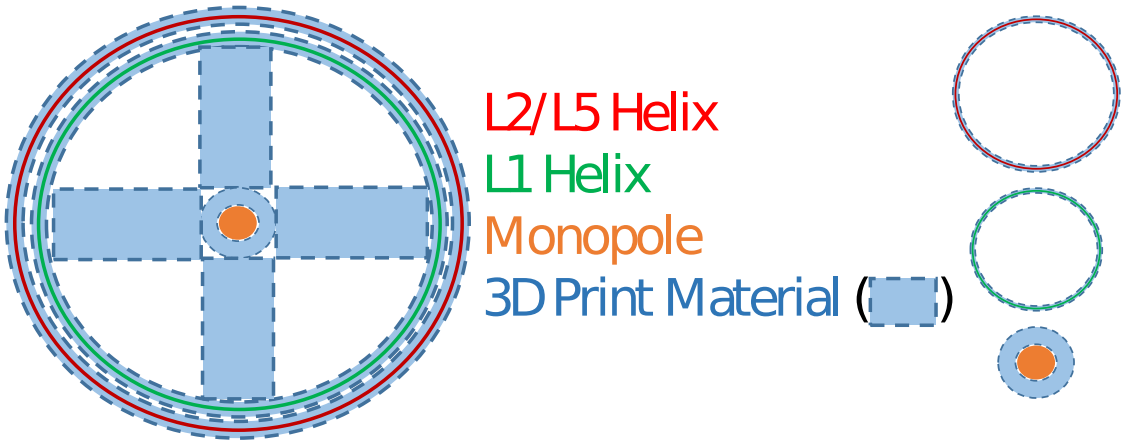

Figure 6.4: Simple Model of 3D Printed Antenna (Left) and Disassembled Individual Antenna Parts (Right)

6.3 Applications

This is a modular, complex antenna system with clear applications to systems such as GPS and GNSS. It is a compact system that gives the user real-time control over the frequency, polarization, and beam direction of the antenna. This could be used to mitigate losses due to polarization mismatch, or to steer the antenna beam away from outside interference, or to track satellites. Also, each of the modular antenna components can be assembled similar to LEGO® blocks, and modified mission to

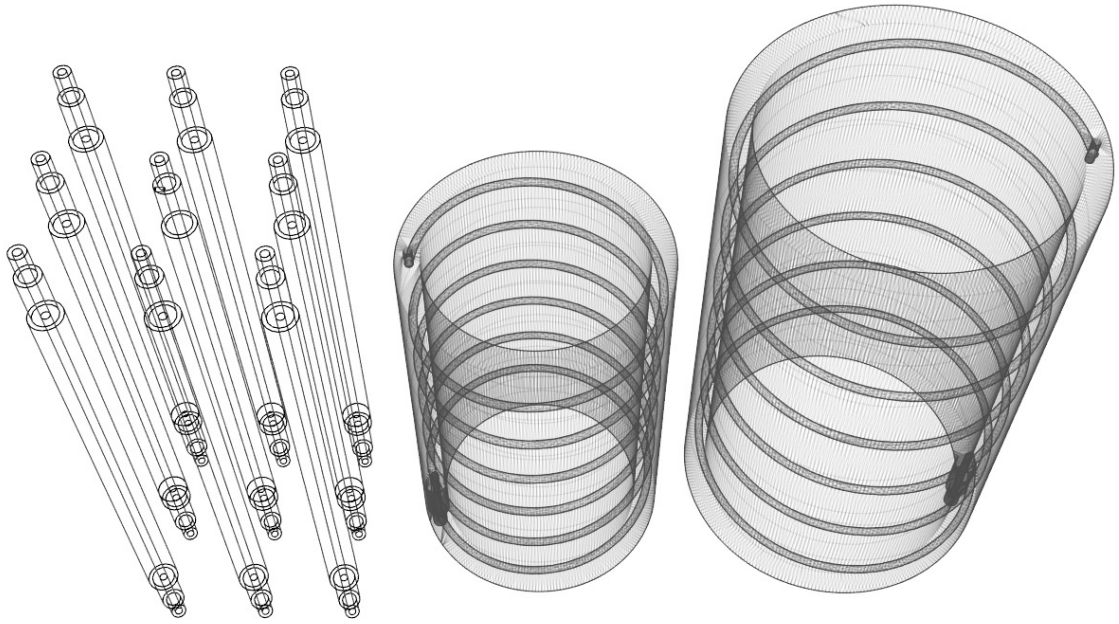

Figure 6.5: CAD Model of 3D Printed Antenna - Outline View

mission, to ensure the user has flexibility in how they use it. GPS frequencies were used for the proof-of-concept model described above, however this technology is not limited to these frequencies. This modular antenna system can be applied to a wide range of frequency bands as long as the mechanical structure is designed to handle the necessary frequency and the feed structure for the antenna is properly designed.

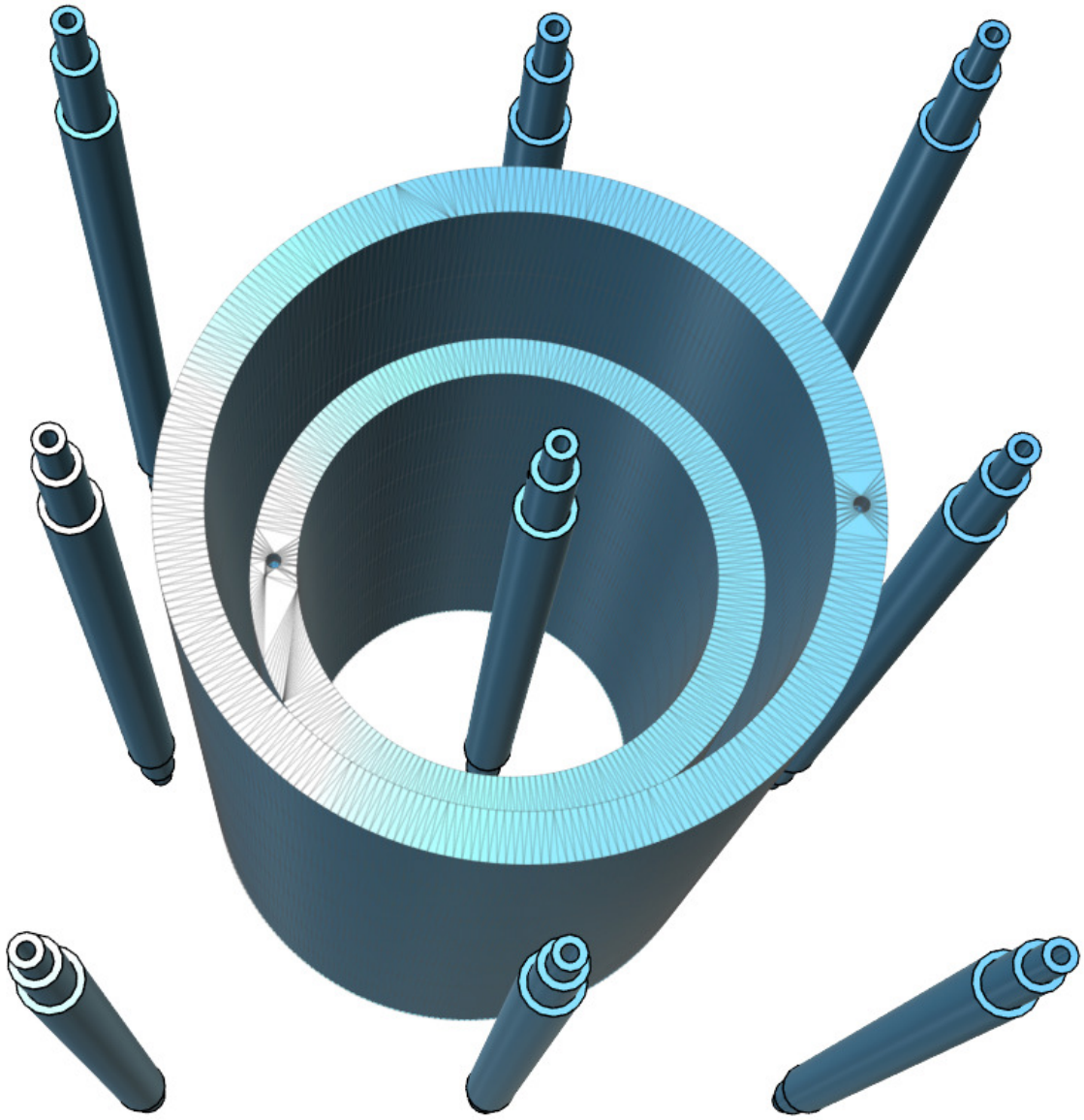

Figure 6.6: CAD Model of 3D Printed Antenna - Solid View

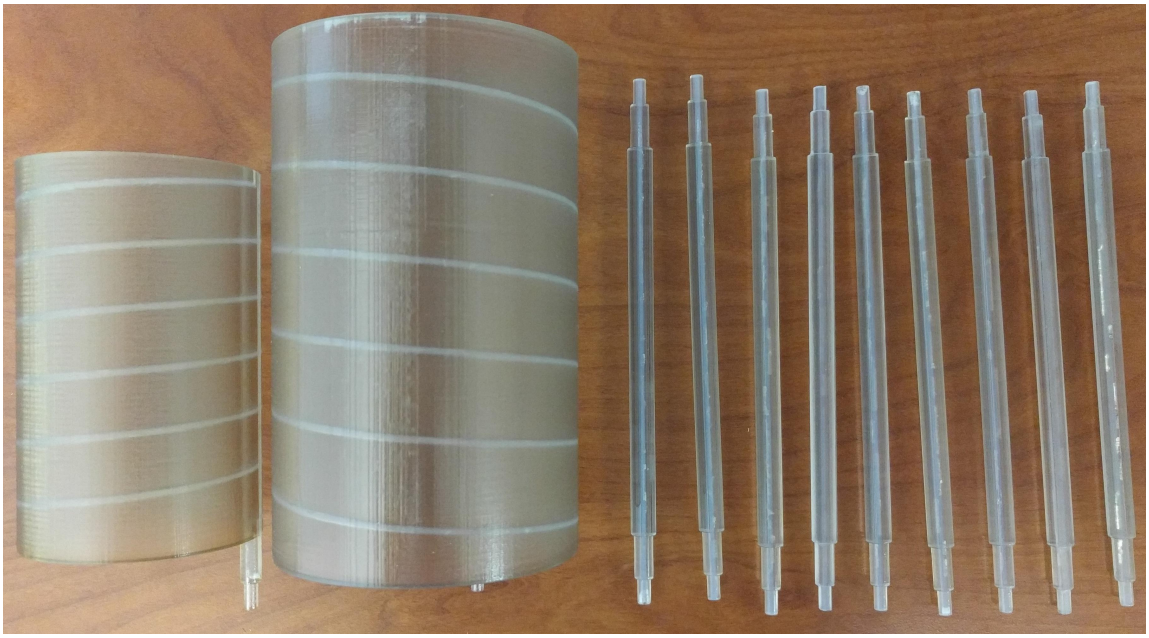

Figure 6.7: 3D Printed Antenna Structure - Separate

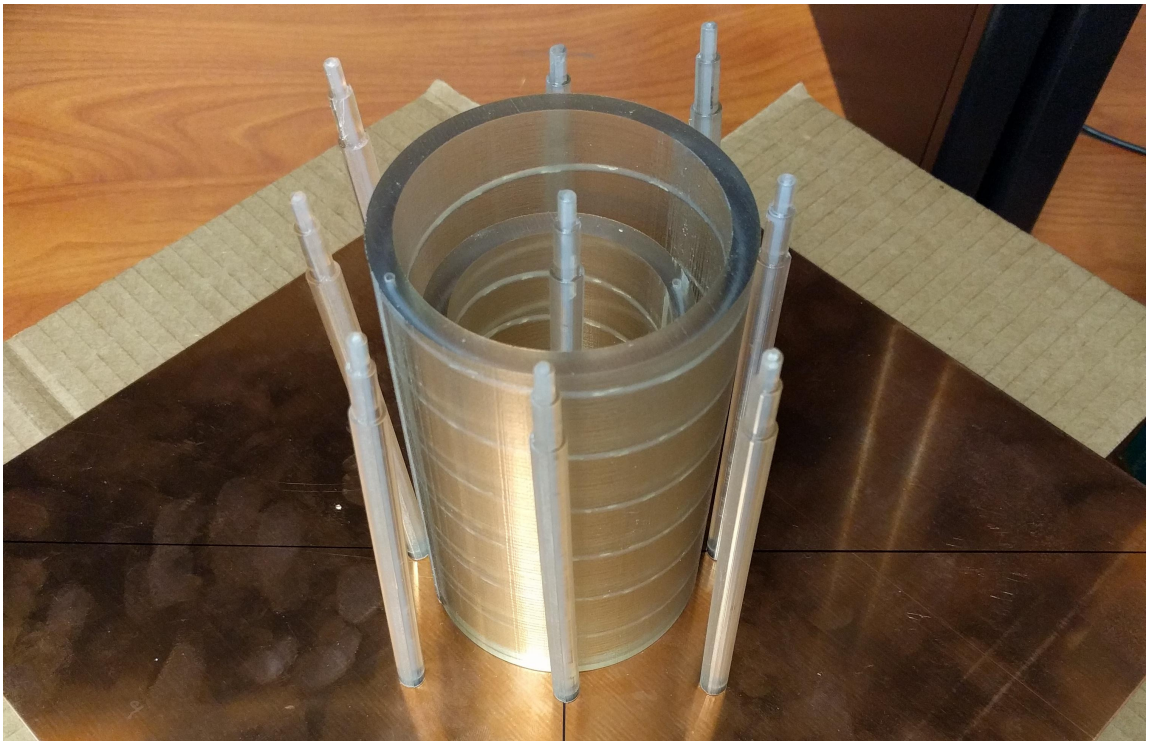

Figure 6.8: 3D Printed Antenna Structure - Combined

6.4 Conclusion

This chapter proposed a new antenna design comprised of many different antenna elements to be used for liquid-metal antenna applications. This design can be 3D printed for reproducibility and also creates a modular antenna giving the user more control over the frequency, gain and polarization of the antenna. This type of modular antenna is an improvement to other modular antenna techniques because individual pieces of the antenna can be left in place without having a negative effect on the overall performance of the system as long as the liquid metal is retracted from the unused piece. Therefore this modular antenna requires fewer adjustments to what pieces are added or subtracted from the system as situations arise, while maintaining the ability to be broken down or disassembled when necessary. As shown from the FEKO simulations the patterns are minimally degraded from the residual feed infrastructure of the other nearby antennas, making this complex antenna system a very good trade. Near-term hardware measurements will be performed to further validate these simulations.

Chapter 7

Current and Future Work

This chapter introduces suggestions to expand the work described in the previous chapters and thoughts of how to move forward with the work to increase its TRL.

7.1 Other Feed Methods

Some more work can be done on improving the monopole feed method while maintaining the ability to easily mechanically inject the liquid metal. One such feed could be the gamma match feed (Fig. 7.1a) because, in conjunction with a variable capacitor, this feed method can be highly adaptable. It was decided to not build this antenna because of the inability to receive a decent result from simulations. One of the issues with this feed method is the need to use a variable capacitor to offset the

inductance created from the gamma rod. Also, there is a minimum height for the antenna using this feed method depending on the feed height of the gamma match to the monopole. Another feed method that was considered was feeding a small coax cable through a hole in the tubing and into the center of the liquid-metal antenna (Fig. 7.1b). Since the metal is liquid, this allows the ability to directly inject the energy into the center of the metal. The problem with this feed method was figuring out a way to ground the outer conductor of the coax cable. When the coax cable is submerged in the liquid metal, we could not figure out a good way to connect the outer conductor to the ground plane without also grounding the liquid metal in the process.

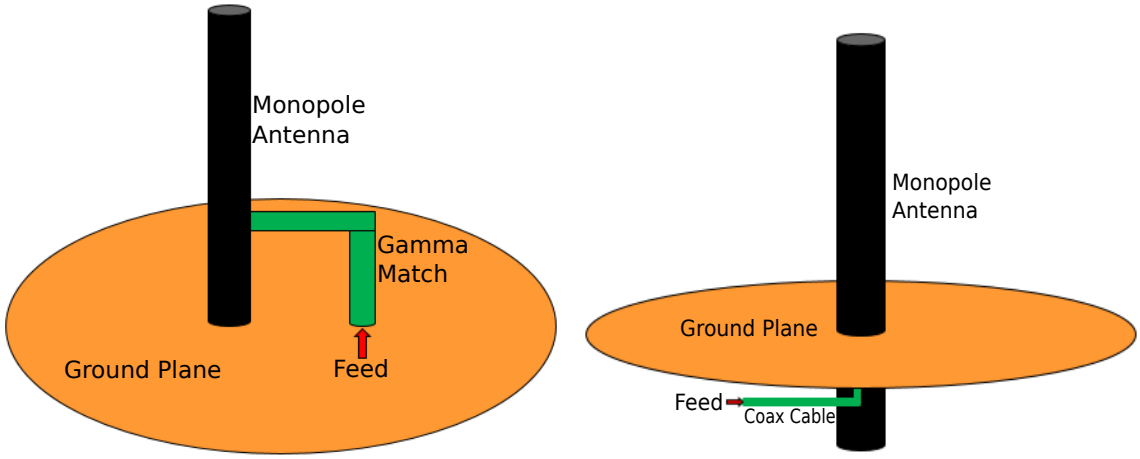

(a) Simple Model of Gamma Match Feed **(b)** Simple Model of Direct Coax Cable Feed

Figure 7.1: Simple Models of Other Proposed Feed Methods

7.2 Reservoir System and Improving Current Offset Feed

The next step for these antennas is to make an array with a common reservoir that can feed liquid metal to each of the antennas. Current research is being done by undergraduates at Virginia Tech Hume Center to use PC water cooling pumps to use water and/or air pressure to in turn push the liquid metal stored in a compressible pouch. The next step in this would be to switch out the PC water cooling pump with a smaller micropump [154] or use electromagnetic pumps. Electromagnetic pumps are currently used to pump liquid metal when liquid metal is used in coolant systems.

For this reservoir system, the offset feed below the ground plane would mechanically be the simplest to implement a reservoir. A modification to the offset feed would make the antennas perform better at the higher frequencies. For the monopole, one option might be to put the SMA pin above the ground plane instead of having the offset feed below the ground plane; this would lower the amount of metal that is radiating down below the ground plane. Having the L-bracket and SMA connector above the ground plane will slightly skew the radiation pattern, but the option of higher frequencies could outweigh this effect depending on the application. Another option would be to minimize the amount of metal below the

ground plane by using a more low-profile L-bracket and improving on the valve system used (Fig. 7.2a). With a stronger soldering iron, it would be possible to solder the SMA connector directly to the ground plane instead of needing an L-bracket to make the connection. For the parasitic elements of the array, it would be better to minimize the amount of metal below the ground plane as well, focusing the energy above the ground plane in the desired direction. This could be done by using different valves or changing them out for switches instead. Last, for the helix antenna, improving the feed method to be a quarter-wave in length below the ground would be beneficial in improving the match between the 50 Ω coax cable and the helical antenna (Fig. 7.2b). The matching network could also be done by integrating a matching circuit into the feed. Since a helix antenna is generally almost purely resistive, a resistor network, such as an L pad, can transform the input impedance of the helix to match the source.

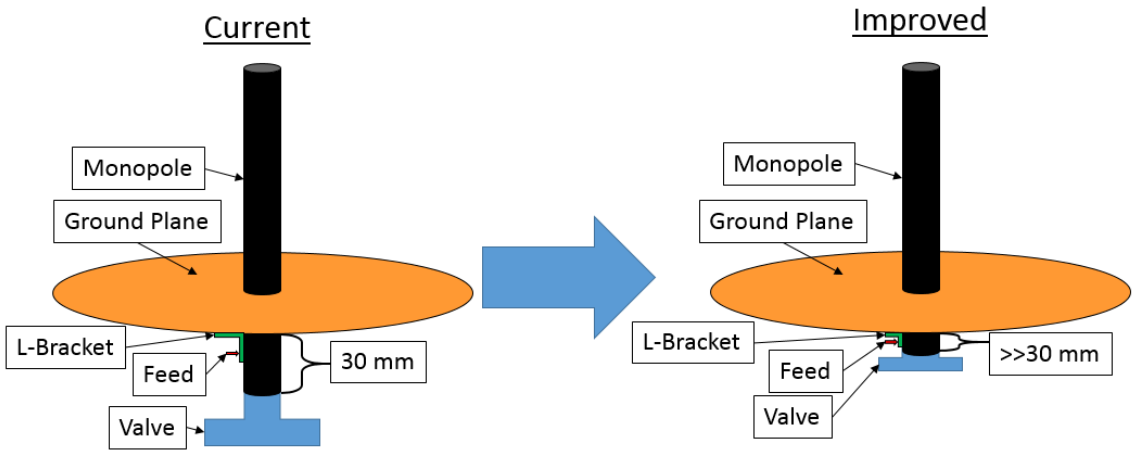

(a) Simple Model of Improved Monopole Feed

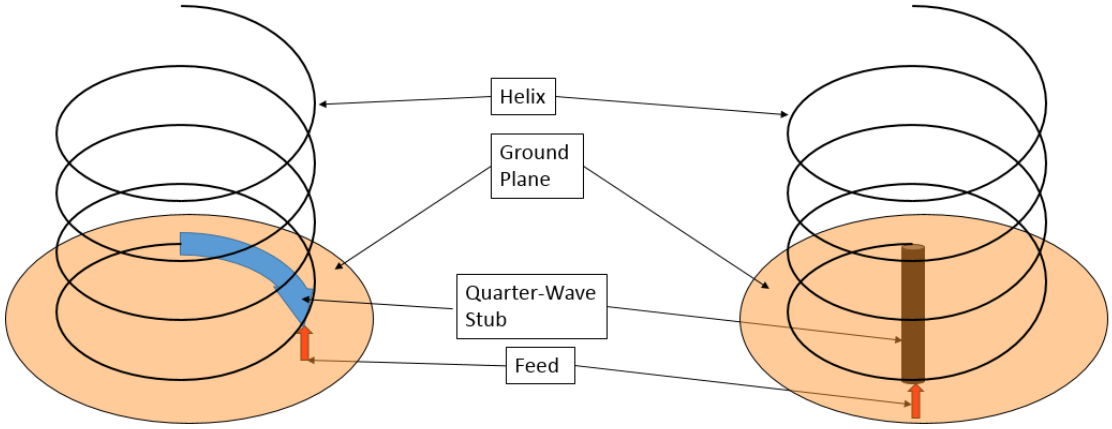

(b) Simple Model of Improved Helix Feed

Figure 7.2: Simple Models of Suggested Improvements to the Feed Methods for Monopole and Helix Antennas

7.3 Other Antenna Designs

Other antenna designs utilizing the liquid-metal conductor were also considered as possibilities including:

- Pixel Array Antenna [155, 156]
- Choke Ring Ground Plane Antenna - change to accept or reject multipath signals [157]
- Spiral/Conical antenna (appear/disappear; raise/lower; change radius) [158]
- Franklin Antenna
- Fractal or Nature-Inspired Antennas
- Phased array fed reflectors (PAFR)
- implement in GATR inflatable antenna
- Slotted waveguide

Using liquid metal in pixel array antennas can create a new degree of freedom with this antenna type (Fig. 7.3). The user can decide if he wants each pixel of the antenna to be individually mechanically fed liquid metal and/or electrically fed or if

just sections of the array are connected. Unlike the MEMS version of this antenna, using liquid metal adds the freedom to make the individual pixels appear/disappear by injecting or retracting the metal. A network of valves can be used to connect the pixels between each other to either connect individual pixels together or to allow for a single injection location and then with the use of the valves, decide which pixels the liquid metal fill.

Another possible antenna design would be a choke ring ground plane antenna where the choke rings are made from liquid metals (Fig. 7.4). This allows the system the ability to either raise or lower the choke rings depending on the situation. When the choke rings are raised, the antenna will reject multi-path and low-angle signals, while when the choke rings are lowered, these low-angle signals are received by the antenna. This type of antenna could also be designed to mitigate multi-path at multiple different frequency bands. One of the difficulties of this type of antenna is obtaining high rejection at multiple frequencies, but by designing rings at different locations and combining this with liquid metal, these rings could be raised and lowered when necessary.

With a flexible antenna form, it is possible to transform an antenna from a circle, to a helix, to a cone, to a spiral or anything in-between (Fig. 7.5). By using tubing or some other flexible container for the liquid metal with the end attached to a glass

rod or some other type of RF invisible material, it would be possible for the user to change the antenna shape between many different forms. By pulling or pushing on the rod, the antenna can change from a circle to a helix or from a spiral to a cone; by twisting the rod, the antenna can change from a helix or a spiral or back. The difficult part of this antenna would be designing a feed that would be efficient at each antenna shape.

Liquid metals could also be applied to phased array technologies to reduce costs and power consumption of the system. Currently, phased arrays require phase shifters to achieve the necessary constructive or destructive interference to perform the beam steering. By utilizing liquid metals, the beam steering could be caused by changes in the physical elements of the array to cause the necessary interference patterns. For example, in a dipole array, certain dipoles could be made longer than the typical $\frac{\lambda}{2}$ length and other shorter to cause different phase changes along those elements. This type of technique is commonly seen in Yagi-Uda antennas. If this same technique was applied to a phased array, the individual element lengths could be adjusted instead of using a phase shifter. This could reduce the complexity of the system and also reduce the amount of hardware needed to run a phased array antenna. Also, this could reduce the overall power consumption of the system because less hardware, and therefore less losses, are introduced.

The GATR inflatable antenna is an inflatable dish antenna for SATCOM. This antenna system offers high portability, ease of set up, low cost and high reliability. This same concept could be applied to liquid-metal antenna technology. If the system was to have two membranes, one to hold the liquid metal and a second to shape the antenna, a more compact antenna may be achieved. This type of system could use air pressure in the second membrane to squeeze the liquid metal into forming the shape of interest and force the metal into any pattern that is desired.

Liquid metal could also be applied to waveguide technology to create a waveguide that can change cutoff frequency (Eqns. 7.1-7.2). By changing the physical dimensions of the waveguide, the cutoff frequency could be adjusted and also the modes the waveguide supports could be changed. Furthermore, this could be applied to slotted waveguide antennas because the slots in the waveguide could be moved or adjusted.

$$f_c = \frac{1}{2a\sqrt{\mu\epsilon}} = \frac{c}{2a} \qquad \text{Rectangular} \qquad (7.1)$$

$$f_c = \frac{1.8412}{2\pi a\sqrt{\mu\epsilon}} = \frac{1.8412c}{2\pi a} \qquad \text{Circular} \qquad (7.2)$$

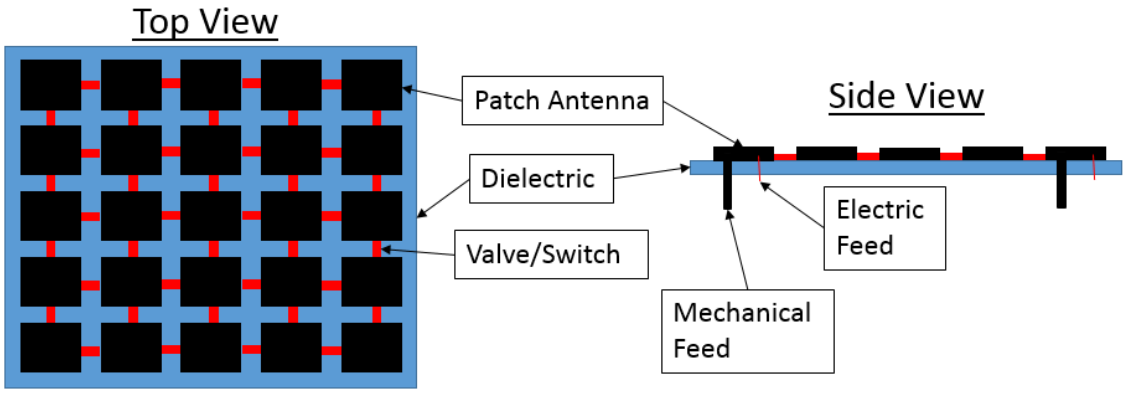

Figure 7.3: Simple Model of Pixel Antenna

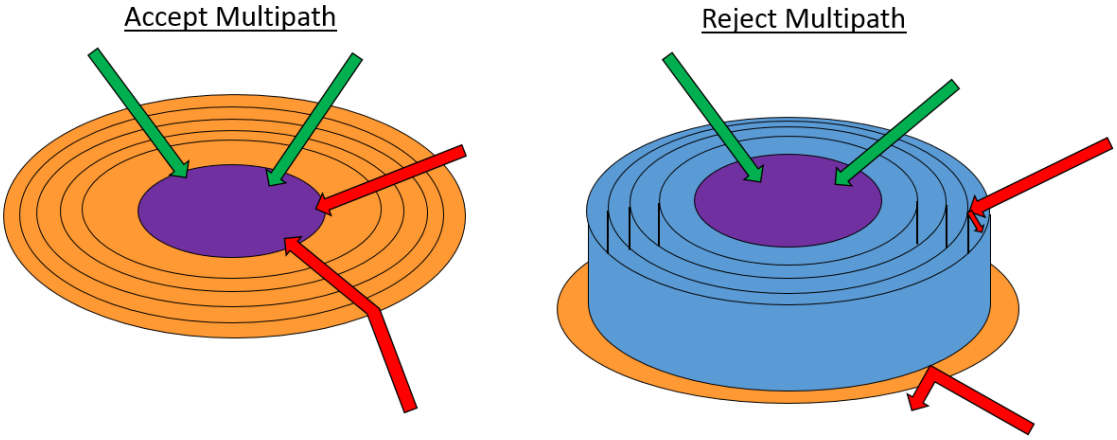

Figure 7.4: Simple Model of Choke Ring Antenna

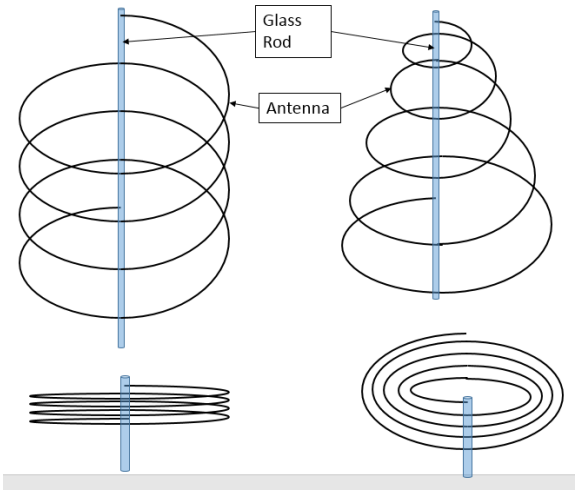

Figure 7.5: Simple Model of a Twisting Helix/Spiral/Cone/Circle Antenna

7.4 Other Research

Table 7.1: Other Areas of Future Research

Experiment	**Objective**
Doping EGaIn	Change conductivity of the metal alloy
Venturi Pump	Create vacuum to prevent oxidation layer from forming
Electromagnetic Pump	Pump liquid metal
Genetic Algorithm [159, 160]	Create and optimize new antenna designs for liquid metal use
Operate antenna near freezing point	Liquid metal has higher conductivity at lower temperatures while still liquid [115–117]
Anechoic chamber	More accurate, more precise, and higher resolution antenna radiation pattern measurements
Test gain of monopole with constant EGaIn height & varying NaOH height	Analyze the effect of NaOH on antenna performance
Use water or oil slip layer inside of tubing [161]	Prevent the EGaIn from wetting the inside of the tubing
Analyze power handing capability [93]	Use as high power emitters (electronic attack antennas)
Metastable phases [111] [1]	Possible meta-stable states with lower freezing point for use in a broader range of situations

[1] Metastable phases may be useful in SATCOM or colder environments because they allow for alloys with a much lower eutectic temperature.

Table 7.1 includes some other areas of research to explore and improve on this technology. In the following experiments, it is assumed that the liquid-metal alloy is already available to the researcher.

Doping the EGaIn with other metals will allow the user to exercise greater control over the conductivity of the alloy. Tweaking the conductivity would be useful to minimize Ohmic losses and create a more efficient antenna. The resources required to complete this experiment would include the dopant materials and a method for testing the conductivity of the modified alloy. This experiment is predicted to take one month or more to complete depending on how many different dopant metals are used.

Another area to explore would be to use a venturi pump or similar device to create a vacuum, would be useful in preventing the oxidation layer from forming over the liquid-metal alloy. Preventing the oxidation layer would decrease the surface tension of the alloy and prevent that alloy from wetting. This vacuum would also remove the need for using NaOH on top of the antenna to corrode the oxidation layer. Using this method would require the antenna/liquid metal to be encased in a closed system to maintain the vacuum. To create this experiment, the experimenter would need both a method of creating the vacuum and a sealed system for the liquid-metal alloy. It is estimated that this experiment would take about two weeks if the venturi pump

can create a strong enough vacuum, more time would be needed to create a stronger vacuum.

Electromagnetic pumps are currently being used to move liquid metal or any other electrically conductive liquid. This type of pump is commonly used to pump liquid metal through cooling systems [162] but could be applied to the liquid-metal antenna application. This could be used along with the reservoir system previously described to pump the liquid metal into the appropriate channels. For this experiment, the required materials are the electromagnetic pump, the common reservoir, and a valve system for deciding the path the liquid metal will take. If the reservoir system and valve system is already created, it is estimated to take a week or two to integrate the electromagnetic pump. If the reservoir system is not already created, this experiment could take three or four months.

Genetic algorithms are very powerful tools that could be used to create new antenna designs for specific desired radiation patterns. A specific set of parameters would need to be selected before creating the genetic algorithm to ensure quick and accurate results. This method could be combined with a rapid prototyping 3D printer to quickly print the required antenna and then attach it to a reservoir system with a pump. This system could be used to rapidly prototype and deploy a specific antenna design. Starting from scratch with the code, this experiment could take a year or so

to create a versatile, efficient algorithm.

If the liquid-metal alloy was operated at near its freezing point (15.5°C), while still remaining liquid, the conductivity of the alloy is higher. This will lead to a more efficient antenna due to less Ohmic losses. To run this experiment would be a method for creating a temperature controlled environment would be needed. It is estimated this experiment would take six months to create a system capable of accurately controlling the alloy temperature.

A fine-tuned, accurate testing set-up would be necessary for comparison solutions and noticing slight differences in performance. An anechoic chamber is room designed to absorb the reflections of electromagnetic waves. This makes it very useful in testing antenna patterns because there will be no interference from extraneous sources or reflections. Also, many anechoic chambers can do automated antenna measurements, which can measure the radiation pattern of the antenna at a much higher azimuthal and elevation resolution with finer precision and accuracy than in a lab bench setting. If the experimenter has access to an anechoic chamber already, it would only take a few days to run the antenna measurements.

Testing the gain of the monopole antenna with constant EGaIn height and varying NaOH heights would create a better understanding of how the NaOH electrolyte on top of the antenna effects the real-world performance of the antenna. This effect could

then be minimized by accounting for it in the overall antenna system. The required materials for this would be the NaOH and a system for measuring the performance of the antenna, such as an anechoic chamber. Testing the monopole antennas with different NaOH heights would take a week or two to complete by hand (with the method described in this thesis) or a few days with an anechoic chamber.

Other possibilities for preventing the oxidation layer from wetting the inside of the tubing would be to use a water or oil slip layer inside of tubing. In [161], it was shown that a water slip layer could be used to prevent the oxidation layer from whetting the channel walls, however the presence of water changes composition of the oxide. The water makes the oxide less passivating, which could have negative effects on the antenna performance; this also deceases the pressure required to inject the liquid metal. Using a layer of oil instead of water on the inside of the tubing might be a possible alternative to prevent the oxide layer from sticking. As described in [114], a layer of paraffin can be used to prevent the oxide layer from wetting glass. To complete this experiment, either a water or oil slip layer should be used inside the tubing and subsequent testing on the effect of this slip layer on the performance of the antenna should be performed. This experiment would take two months to create the slip layer and then test the antenna to determine if there are any adverse effects on the antenna created with the slip layer.

The power handing capability should be tested to find out if this type of antenna could be used to as a high power emitter for the purpose of electronic warfare. In [93], the author claims higher current densities are possible with liquid metals than with solid metal. This could be due to the high thermal conductivity of liquid metals, allowing for more heat to be safely transferred to the air through convection. To perform this experiment, a measure of the thermal properties of the antenna versus input power is necessary.

As described in [111], there are metastable phases of Ga-In that could be used to create an alloy with a lower freezing point. Also, gallium is known to be able to be supercooled to a much lower temperature than its freezing point (as far down as 12K in droplet form), while remaining liquid [163, 164]. This could be useful in SATCOM or colder environments in which deployable antennas are commonly used. Creating these metastable states would take as estimated two months and another four months or so to integrate it into an antenna system.

7.5 Application Work

Additional work on the structure needs to be researched to improve the TRL of this technology.

- better/smaller pumps needed (especially for police vest)
- better/smaller switching or valve system needed
  - much smaller valves to integrate into system
  - better valve structure will allow more control over the flow
- smaller tubing for easier integration or have 3D printed structure
  - use microfluidic printer (Example: Dolomite Fluidic Factory 3D Printer [165])

Adding a temperature controlled environment around the antenna element would allow the system to maintain a liquid state of the alloy (Fig. 7.6). As seen in Appendix A.1, the liquid form of gallium has a higher conductivity and therefore will introduce less Ohmic losses. This type of system might also be able to be used as a meltable, space deployable antenna.

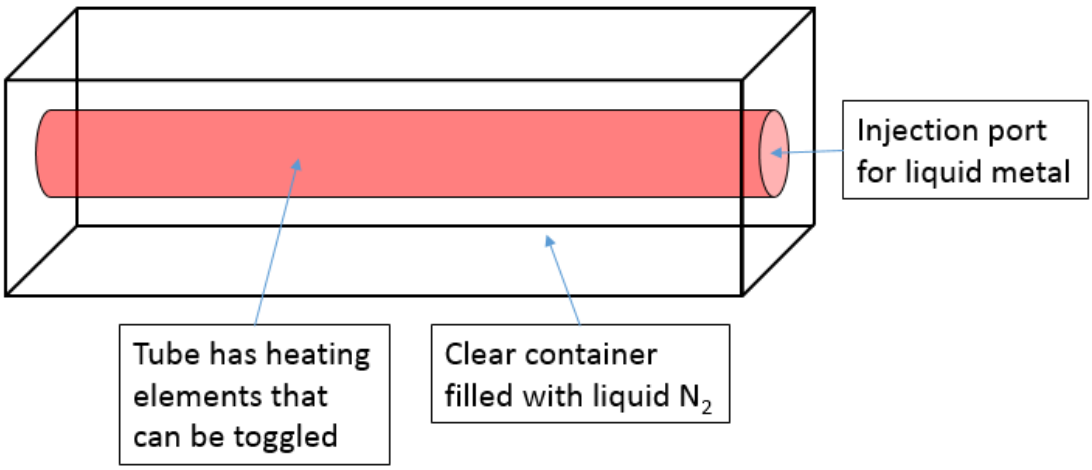

Figure 7.6: Simple Model of Heated Element

Chapter 8

Conclusions and Contributions

This work expanded upon reconfigurable antenna technology by utilizing physical adaptions possible with a liquid-metal alloy. Three distinct proof-of-concept antennas were built and tested then compared to simulations performed in FEKO. The analysis of these results showed using liquid-metal EGaIn as the main conductor did not have a negative impact on the overall performance of the antennas.

In Chapter 3, mechanical and electrical feeds were examined to allow for the liquid metal to be injected and retracted while maintaining acceptable performance. Two of these feed methods had not been previously researched for liquid-metal monopole antennas. Then in Chapter 4, a two-dimensional parasitic monopole array was built which allowed for both frequency changes and directivity control. A linear parasitic

monopole array had previously been studied; this work expanded upon that idea to create a two-dimensional array that gives the user more control over the main beam direction. Next, in Chapter 5, a dual-helix antenna was introduced which gives the user control over frequency and polarization. Utilizing liquid metal to create a helix with this structure had not previously been researched. Last, in Chapter 6, a combination of these three antennas was created and additively manufactured to create a modular antenna. This modular antenna gives the user the option to decide which individual pieces of the antenna are needed and has the ability to exercise control over frequency, polarization and directivity. This type of additive printed structure had not previously been used for liquid-metal antenna technology.

More research is needed to improve the TRL of this technology but given the positive results of this work, this field looks very promising for creating a highly reconfigurable antenna. A better valve structure and pumping mechanism is the first step in creating a more efficient and more robust antenna system. By adding these features, computerization of the antenna adjustments can be made so the antenna can react without the need of human input. This capability would be very useful in a wide range of military and commercial situations.

Appendix A

A.1 Conductivities [1–3]

Table A.1: Conductivities of Common Metals

Conductor	Conductivity (S/m)	Symbol
Aluminum	3.816×10^7	Al
Brass	2.564×10^7	CuZn
Bronze	1.00×10^7	CuSn + Other
Chromium	3.846×10^7	Cr
Copper	5.813×10^7	Cu
EGaIn	3.4×10^6	GaIn
Gallium	2.227×10^6 @ 30°C 3.858×10^6 @ 30°C	Ga (solid) Ga (liquid)
Gold	4.098×10^7	Au
Indium	1.12×10^7 @ 20°C 6.875×10^6 @ 150°C	In (solid) In (liquid)
Iron	1.03×10^7	Fe
Mercury	1.04×10^6	Hg
Lead	4.56×10^6	Pb
Nickel	1.449×10^7	Ni
Platinum	9.52×10^6	Pt
Sea water	$3 - 5$	NaCl in H_2O (solution)
Silver	6.1×10^7	Ag
Tungsten	1.825×10^7	W
Zinc	1.67×10^7	Zn

A.2 Physical Constants

Table A.2: Common Physical Constants

Permitivity of Free Space	$\epsilon_0 = 8.854 \times 10^{-12}$ F/m $\approx 10^{-9}/36\pi$ F/m
Permeability of Free Space	$\mu_0 = 1.26 \times 10^{-6}$ H/m $\approx 4\pi \times 10^{-7}$ H/m
Velocity of Light in Free Space	$c = \frac{1}{\sqrt{\mu_0 \epsilon_0}} = 2.997925 \times 10^8$ m/s
Intrinsic Impedance of Free Space	$\eta_0 = \sqrt{\frac{\mu_0}{\epsilon_0}} = 367.73\ \Omega \approx 120\pi\ \Omega$

A.3 Frequency Band Designations

Table A.3: RF Frequency Band Designations

Frequency	Band Designation	Typical λ	Use Examples
$3 - 30$ kHz	VLF (Very Low)	100 km − 10 km	Sonar
$30 - 300$ kHz	LF (Low)	10 km − 1 km	Radio Beacons
300 kHz − 3 MHz	MF (Medium)	1 km − 100 m	AM Radio
$3 - 30$ MHz	HF (High)	100 m − 10 m	Short Wave Radio, CB Radio
$30 - 300$ MHz	VHF (Very High)	10 m − 1 m	Television, FM Radio, Mobile Radio
300 MHz − 3 GHz	UHF (Ultra High)	1 m − 100 mm	SATCOM, Radar, GPS
$3 - 30$ GHz	SHF (Super High)	100 mm − 10 mm	Radar, Microwave Links, Mobile, SATCOM
$30 - 300$ GHz	EHF (Extra High)	10 mm − 1 mm	
$1 - 2$ GHz	L	30 cm − 15 cm	GPS, GSM, GNSS
$2 - 4$ GHz	S	15 cm − 7.5 cm	WiFi
$4 - 8$ GHz	C	75 mm − 37.5 mm	SATCOM, Terrestrial Microwave Links
$8 - 12$ GHz	X	37.5 mm − 25 mm	Radar
$12 - 18$ GHz	Ku	25 mm − 16.66 mm	SATCOM, Radar
$18 - 27$ GHz	K	16.66 mm − 11.1 mm	Amateur radio
$27 - 40$ GHz	Ka	11.1 mm − 7.5 mm	NASA DSN coms
$40 - 300$ GHz		7.5 mm − 1 mm	

Appendix B

B.1 Basic Antenna Theory

B.1.1 Input Impedance

The input impedance is described by the ratio of the voltage to current at a pair of terminals. Impedance matching is the process of changing the impedance of a loaded device to match the impedance of the source. This method minimizes reflections due to impedance mismatches.

For an antenna, the input impedance is described as

$$Z_L = R_{loss} + R_{rad} + jX_a = R_a + jX_a \tag{B.1}$$

where

- R_{loss} is the loss resistance of the antenna
- R_{rad} is the radiation resistance of the antenna

- $R_a = R_{loss} + R_{rad}$ is the total resistance of the antenna
- X_a is the reactance of the antenna

B.1.2 Return Loss

Return loss (also called s_{11} or reflection coefficient Γ) is one of the scattering parameters that defines the ratio of power incident power (P_I) to the reflected power (P_R). This is due to a mismatch between the transmission line and the device or antenna.

$$\Gamma = \frac{Z_L - Z_0}{Z_L + Z_0} = s_{11} \tag{B.2}$$

where Z_L is the input impedance of the antenna and Z_0 is the characteristic impedance. Expressed in dB, the return loss is

$$\text{RL (dB)} = 10 \log_{10} \left(\frac{P_I}{P_R} \right) = -20 \log |\Gamma| \tag{B.3}$$

Another way to describe the reflected power of an antenna is with the voltage standing wave ratio (VSWR).

$$\text{VSWR} = \frac{1 + |\Gamma|}{1 - |\Gamma|} \tag{B.4}$$

B.1.3 Efficiency

Antenna efficiency is defined by not only the reflection efficiency of the antenna, but also the conduction and dielectric efficiencies.

$$e_0 = e_r e_c e_d = e_r e_{cd} \tag{B.5}$$

where

- e_0 is the total efficiency of the antenna
- e_r is the reflection efficiency of the antenna $(1 - |\Gamma|^2)$
- e_c is the conduction efficiency due to the finite conductivity of the materials
- e_d is the dielectric efficiency due to conductivity of nearby dielectric materials
- $e_{cd} = e_c e_d = \epsilon_e$ is the called radiation efficiency of the antenna

The radiation efficiency is also defined as the ratio of total radiated power to the total input power to the antenna. Due to losses, the input power to the antenna can be described as the radiated power plus the loss power from mismatching, ohmic heating, etc.

$$\epsilon_e = \frac{P_{rad}}{P_{in}} = \frac{P_{rad}}{P_{rad} + P_{loss}} \tag{B.6}$$

B.1.4 Field Regions

The space around the antenna are split into three distinct regions: the reactive near-field, the radiating near-field and the far field regions (Fig. B.1)

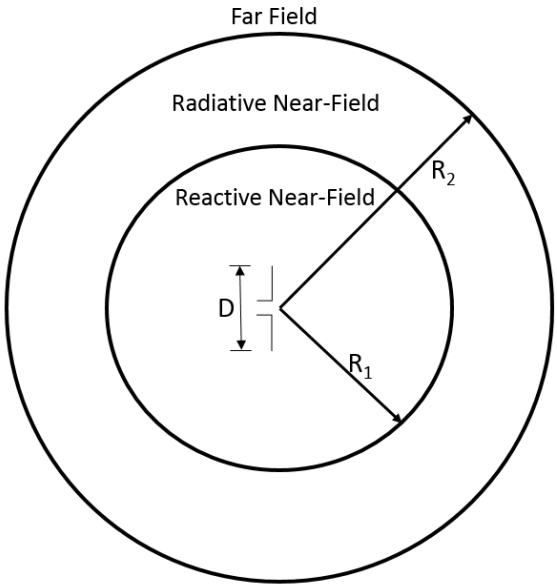

Figure B.1: Antenna Field Regions

The reactive near-field is the field directly surrounding the antenna with a boundary defined as

$$R < 0.62\sqrt{D^3/\lambda} \tag{B.7}$$

The radiating near field is the space between the reactive near field and the far field, defined as

$$0.62\sqrt{D^3/\lambda} \ll R < 2D^2/\lambda \tag{B.8}$$

Last, the far field is the space beyond the reactive near field at

$$2D^2/\lambda \ll R \tag{B.9}$$

B.1.5 Radiation Pattern

The radiation pattern of the antenna is the variation of the power radiated by an antenna as a function of θ and ϕ in spherical coordinates.

B.1.6 Directivity and Gain

Directivity is a measure of how directional the antenna's radiated power is. If an antenna was to transmit power equally in all directions, the antenna would be called ideally isotropic and would have a directivity of one (0 dB). Gain is more commonly used, which is related to the directivity through Eqn. B.11. The gain is often quoted in dBi, which is the gain of the antenna to the gain of an ideal isotropic radiator.

$$D = \frac{1}{\frac{1}{4\pi}\int_0^{2\pi}\int_0^{\pi}|F(\theta,\phi)|^2 sin(\theta)d\theta d\phi} \tag{B.10}$$

where $F(\theta,\phi)$ is the antenna's normalized radiation pattern in spherical coordinates.

From this, the gain can be determined from

$$G = e_0 D \tag{B.11}$$

Fig. B.2 displays the IEEE standard flow chart of gain, realized gain, directivity, and the conversion between them.

B.1.7 Beamwidth and Sidelobes

There are two main ways to describe the beamwidth of an antenna. The first is the half power beamwidth (HPBW), which is the angular separation in which the radiation pattern decreases by -3 dB from the peak of the main beam. The other type of beamwidth is the null to null beamwidth, which is the angular separation where the radiation pattern decreases from the maximum of the main beam to $-\infty$ dB.

An approximation for the 3 dB beamwidth of an antenna is

$$\theta_{3\text{dB}} = \frac{75\lambda}{D} \tag{B.12}$$

where D is the dimension of the antenna.

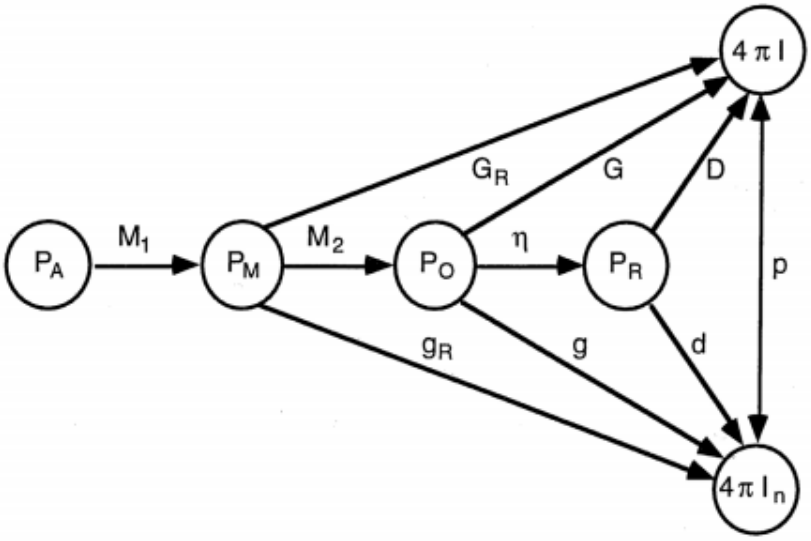

P_A = power available from the generator
P_M = power to matched transmission line
P_O = power accepted by the antenna
P_R = power radiated by the antenna
I = radiation intensity
I_n = partial radiation intensity†
M_1 = impedance mismatch factor 1
M_2 = impedance mismatch factor 2

η = radiation efficiency
G_R = realized gain
G = gain
D = directivity
g_R = partial realized gain
g = partial gain
d = partial directivity
p = polarization efficiency

†All partial quantities correspond to a specified polarization, n.

Figure B.2: IEEE Definition of Gain and Directivity. Reprinted with permission from IEEE. Copyright IEEE 2013. All rights reserved. [21]

An approximation for antenna beamwidth compared to gain:

$$G \approx \frac{26,000}{\theta_A \theta_B} \approx \frac{26,000}{\theta_B^2} \tag{B.13}$$

where θ_A and θ_B are the beamwidths of the antenna. If the beam is circular, $\theta_A = \theta_B$.

Sidelobes are smaller beams that are away from the main beam. These sidelobes are generally radiation in undesired directions that cannot be completely eliminated but can be minimized. The sidelobe level is a description of the maximum value of the sidelobes away from the main antenna beam. Back lobes refer to sidelobes that are directly behind the main beam of the antenna.

B.1.8 Polarization

The polarization of an antenna is the orientation of the electric field with respect to the Earth's surface. The most general case of polarization is elliptical in which the magnitude of the E and H fields vary over time. Two special cases of polarization are linear and circular polarization. Linear polarization occurs when the electric field vector is confined to a specific plane along the direction of propagation. If this plane is oriented vertically, it is considered vertically polarized. Circular polarization occurs when the electric field has a constant magnitude but its direction rotates with time at a steady rate perpendicular to the direction of the wave. Depending on the direction of rotation of the electric field in reference to the direction of the wave, circular polarization can be defined as left-hand circular or right-hand circularly polarized. Table B.1 lays out the ideal losses to be expected between two antennas with specific polarizations. the equations for polarization mismatch loss are listed in

[166]. In practice, it is more common to have some response from the antennas even if their waves are cross-polarized.

Table B.1: Power Loss from Polarization Mismatch

	Vertical	Horizontal	LHCP	RHCP
Vertical	0 dB	$-\infty$ dB	-3 dB	-3 dB
Horizontal	$-\infty$ dB	0 dB	-3 dB	-3 dB
LHCP	-3 dB	-3 dB	0 dB	$-\infty$ dB
RHCP	-3 dB	-3 dB	$-\infty$ dB	0 dB

B.1.9 Bandwidth and Quality Factor (Q-Factor) [1]

The bandwidth is defined as the range of frequencies at which the antenna can properly radiate energy. Depending on the application of the antenna, a large or small bandwidth is desired.

$$BW = \Delta\omega \tag{B.14}$$

The fractional bandwidth is a measure of how wideband an antenna is, defined as

$$FBW = \frac{\omega_2 - \omega_1}{\omega_c} = \frac{\Delta\omega}{\omega_c} \tag{B.15}$$

It is usually quoted as a percentage, with a higher percentage meaning the antenna is more wideband.

The quality factor of the antenna is a measure of the loss of a resonant circuit.

Therefore the higher the Q-factor, the lower the loss and the lower the bandwidth.

$$\begin{aligned} Q &= \omega \frac{(\text{average energy stored})}{(\text{energy loss/second})} \\ &= \omega \frac{W_m + W_e}{P_l} \end{aligned} \tag{B.16}$$

where W_m is the average magnetic energy stored and W_e is the average electric energy stored in the device. At resonance, $W_e = W_m$, so this simplifies to

$$Q = \omega_0 \frac{2W_m}{P_l} = \frac{\omega_0 L}{R} = \frac{1}{\omega_0 RC} \tag{B.17}$$

The fractional bandwidth is inversely proportional to the quality factor of the antenna

$$FWB = \frac{\Delta\omega}{\omega_c} = \frac{1}{Q} \tag{B.18}$$

B.1.9.1 Impedance Bandwidth

Impedance bandwidth is the frequency span in which some requirement for the return loss is satisfied. In other words, the impedance bandwidth is the frequency range from f_1 to f_2 in which the reflection coefficient is below some accepted value (e.g. $s_{11} < -3$ dB).

B.1.9.2 Radiation Pattern Bandwidth

Radiation pattern bandwidth is the frequency range in which some requirement for the gain of the antenna is satisfied. For example, the radiation pattern bandwidth is the frequency range at which the gain of the antenna is within 3 dB of the maximum gain of the antenna.

Appendix C

C.1 Skin Depth Derivation [4]

In conductors, a parameter known as skin depth is a measure of how deep electrical conduction takes place from the surface of the conductor. For DC (0 Hz) frequency, the cross-sectional area of a wire determines the resistance per unit length of the wire. At RF frequencies, the effect of the conductor thickness on its conductance is not-linear.

Starting with Maxwell's equations in linear media,

$$\nabla \bullet \vec{E} = \frac{\rho}{\epsilon} \tag{C.1}$$

$$\nabla \bullet \vec{B} = 0 \tag{C.2}$$

$$\nabla \times \vec{E} = -\frac{\delta \vec{B}}{\delta t} \tag{C.3}$$

$$\nabla \times \vec{B} = \mu \vec{J} + \mu\epsilon \frac{\delta \vec{E}}{\delta t} \tag{C.4}$$

Within a conductor of finite conductivity σ, Ohm's law can be written as

$$\vec{J} = \sigma \vec{E} \tag{C.5}$$

and with no surface charge ($\rho = 0$), Maxwell's equations can be re-written as

$$\nabla \bullet \vec{E} = 0 \tag{C.6}$$

$$\nabla \bullet \vec{B} = 0 \tag{C.7}$$

$$\nabla \times \vec{E} = -\frac{\delta \vec{B}}{\delta t} \tag{C.8}$$

$$\nabla \times \vec{B} = \mu\sigma\vec{E} + \mu\epsilon\frac{\delta \vec{E}}{\delta t} \tag{C.9}$$

Take the curl of Eqn. C.8.

$$\nabla \times (\nabla \times \vec{E}) = \nabla(\nabla \bullet \vec{E}) - \nabla^2\vec{E} \tag{C.10}$$

$$= -\nabla \times \frac{\delta \vec{B}}{\delta t} \tag{C.11}$$

$$= -\mu\epsilon\frac{\delta^2\vec{E}}{\delta t^2} - \mu\sigma\frac{\delta \vec{E}}{\delta t} \tag{C.12}$$

Since $\nabla \bullet \vec{E} = 0$ we get

$$\nabla^2\vec{E} = \mu\epsilon\frac{\delta^2\vec{E}}{\delta t^2} + \mu\sigma\frac{\delta \vec{E}}{\delta t} \tag{C.13}$$

Using a similar method on Eqn. C.9 gives

$$\nabla^2 \vec{B} = \mu\epsilon \frac{\delta^2 \vec{B}}{\delta t^2} + \mu\sigma \frac{\delta \vec{B}}{\delta t} \tag{C.14}$$

This solution is the wave equation with an additional first derivative. These equations have a similar solution to the ordinary wave equation. For a plane wave traveling in the z direction, we have

$$E(\vec{z}, t) = E_0 e^{i(kz - \omega t)} \tag{C.15}$$

$$B(\vec{z}, t) = B_0 e^{i(kz - \omega t)} \tag{C.16}$$

Substituting Eqn. C.15 into Eqn. C.13 and canceling some terms gives us

$$\vec{k}^2 = \omega^2 \mu\epsilon + i\omega\mu\sigma \tag{C.17}$$

Since the wave vector $\vec{k}$ is complex, that means the resulting wave has an oscillatory and exponentially decaying factor. Simplifying $\vec{k}$ gives

$$\vec{k} = \frac{1}{2}\sqrt{2\sqrt{\omega^4\mu^2\epsilon^2 + \omega^2\mu^2\sigma^2} + 2\omega^2\mu\epsilon} + \frac{1}{2}i\sqrt{2\sqrt{\omega^4\mu^2\epsilon^2 + \omega^2\mu^2\sigma^2} - 2\omega^2\mu\epsilon} \tag{C.18}$$

$$= \frac{\omega\sqrt{\mu\epsilon}}{\sqrt{2}}\sqrt{\sqrt{1 + \left(\frac{\sigma}{\epsilon\omega}\right)^2} + 1} + i\frac{\omega\sqrt{\mu\epsilon}}{\sqrt{2}}\sqrt{\sqrt{1 + \left(\frac{\sigma}{\epsilon\mu}\right)^2} - 1} \tag{C.19}$$

$$= k + i\kappa \tag{C.20}$$

The wave is then given by

$$E(\vec{z},t) = E_0 e^{-\kappa z} e^{i(kz-\omega t)} \tag{C.21}$$

$$B(\vec{z},t) = B_0 e^{-\kappa z} e^{i(kz-\omega t)} \tag{C.22}$$

Therefore, the skin depth (δ) is defined as

$$\delta = \frac{1}{\kappa} = \frac{1}{\omega}\left[\frac{\mu\epsilon}{2}\left(\sqrt{1+\left(\frac{\sigma}{\epsilon\omega}\right)^2}-1\right)\right]^{-\frac{1}{2}} \tag{C.23}$$

Assuming a perfect conductor , so $\chi = 0$

$$\epsilon = \epsilon_0(1+\chi) = \epsilon_0 \tag{C.24}$$

Also assuming $\mu = \mu_0$ and $\frac{\sigma}{\epsilon\omega} >> 1$ (assuming good conductor), a good approximation of the skin depth can be written as

$$\delta = \frac{1}{\omega}\sqrt{\frac{2\omega}{\mu_0\sigma}} = \sqrt{\frac{2}{\omega\mu_0\sigma}} \tag{C.25}$$

C.2 Antenna Radiation Efficiency using the Wheeler Cap Method Derivation [5–10]

C.2.1 Constant Power Loss Method

For electrically short antennas ($L < \frac{\lambda}{10}$), the power lost in resistance (R_{loss}) is about the same with or without the wheeler cap because the radiation resistance is so small (Eqn. C.26). With the assumption of constant power loss, we can make use of the s_{11} magnitude measurements with the cap on and off.

$$R_{rad} = 160\pi^2 \left(\frac{L}{\lambda}\right)^2 \tag{C.26}$$

The radiation efficiency is defined as the ratio of the radiated power to the input power of an antenna

$$\epsilon_e = \frac{P_{rad}}{P_{in}} = \frac{P_{rad}}{P_{rad} + P_{loss}} \tag{C.27}$$

where

ϵ_e is the efficiency of the antenna

P_{rad} is the radiating power of the antenna

P_{in} is the input power to the antenna

P_{loss} is the power lost in the antenna

Assuming the antenna has an identical current distribution, Eqn. C.27 can be re-written as

$$\epsilon_e = \frac{I^2 R_{rad}}{I^2 R_{rad} + I^2 R_{loss}} = \frac{R_{rad}}{R_{rad} + R_{loss}} \tag{C.28}$$

where

R_{rad} is the radiation resistance

R_{loss} is the loss resistance

I is input current

From here we can find the resistances of the antenna to the reflection coefficient. The reflection coefficient is easily obtained using a vector network analyzer in the form of the return loss (s_{11}).

$$\Gamma_{FS} = Re\left|\frac{(R_{rad} + R_{loss}) - R_0}{(R_{rad} + R_{loss}) + R_0}\right| \tag{C.29}$$

$$\Gamma_{WC} = Re\left|\frac{R_{loss} - R_0}{R_{loss} + R_0}\right| \tag{C.30}$$

where

Γ_{FS} is the reflection coefficient measurement without the Wheeler cap (free

space)

Γ_{WC} is the reflection coefficient measurement with the Wheeler cap

R_0 is the characteristic resistance

Eqn. C.30 can be re-written as

$$R_{loss} = \left(\frac{1+\Gamma_{WC}}{1-\Gamma_{WC}}\right) R_0 \tag{C.31}$$

Substituting Eqn. C.31 into Eqn. C.29 gives

$$R_{rad} = \frac{2(\Gamma_{FS}+\Gamma_{WC})}{(1+\Gamma_{WC})(1-\Gamma_{FS})} R_0 \tag{C.32}$$

Next, substituting Eqn. C.31 and Eqn. C.32 into Eqn. C.27 gives

$$\epsilon_e = \frac{R_{rad}}{R_{rad}+R_{loss}} = 1 - \frac{(1-\Gamma_{FS})(1+\Gamma_{WC})}{(1+\Gamma_{FS})(1-\Gamma_{WC})} \tag{C.33}$$

Assuming the power of loss resistance is constant, the loss power and input power are given by

$$P_{loss} = (1-\Gamma_{WC}^2)P_0 \tag{C.34}$$

$$P_{in} = P_{rad} + P_{loss} = (1-\Gamma_{FS}^2)P_0 \tag{C.35}$$

After substituting these power equations in, we get a radiation efficiency from the power ratio of

$$\epsilon_e = \frac{P_{rad}}{P_{rad} + P_{loss}} = \frac{(1 - \Gamma_{FS}^2) - (1 - \Gamma_{WC}^2)}{1 - \Gamma_{FS}^2} = \frac{\Gamma_{WC}^2 - \Gamma_{FS}^2}{1 - \Gamma_{FS}^2} \tag{C.36}$$

C.2.2 Constant Loss Resistor Method

As the antenna becomes longer, the radiation resistance increases and the assumption of constant power loss is invalid. So, a method of efficiency that makes use of R_{rad} and R_{loss} is preferred. Therefore, we start with the resistance ratio instead of the power ratio:

$$\epsilon_e = \frac{R_{rad}}{R_{rad} + R_{loss}} \tag{C.37}$$

Here, the key assumption is R_{loss}, rather than P_{loss}, remains constant with or without the wheeler cap in place. With the Wheeler cap on, the radiation resistance is zero and the antenna reflection coefficient is $s_{11_{WC}}$.

$$s_{11_{WC}} = \frac{R_{loss} - R_s}{R_{loss} + R_s} \tag{C.38}$$

And with the Wheeler cap off, the reflection coefficient is $s_{11_{FS}}$.

$$s_{11_{FS}} = \frac{R_{loss} - R_s}{R_{loss} + R_s} \tag{C.39}$$

Eqns. C.38 and C.39 are transposed to become

$$\frac{R_{loss}}{R_s} = \frac{1 + s_{11_{WC}}}{1 - s_{11_{WC}}} \tag{C.40}$$

$$\frac{(R_{rad} + R_{loss})}{R_s} = \frac{1 + s_{11_{FS}}}{1 - s_{11_{FS}}} \tag{C.41}$$

and then combined to have an efficiency equation of

$$\epsilon_e = \frac{R_{rad}}{R_{rad} + R_{loss}} = \frac{\frac{1+s_{11_{FS}}}{1-s_{11_{FS}}} - \frac{1+s_{11_{WC}}}{1-s_{11_{WC}}}}{\frac{1+s_{11_{FS}}}{1-s_{11_{FS}}}} \tag{C.42}$$

$$\epsilon_e = 1 - \frac{(1 - s_{11_{FS}})(1 + s_{11_{WC}})}{(1 + s_{11_{FS}})(1 - s_{11_{WC}})} \tag{C.43}$$

Eqn. C.43 is more accurate than Eqn. C.36 regardless of R_{rad}, however Eqn. C.43 must have all-real s_{11} measurements, which may or may not be the same as the minimum of $|s_{11}|$.

C.3 Monopole Far Field, Input Impedance, Radiation Resistance, Directivity [11–14]

At some far-field point from the antenna, the numerical directivity $d(\theta, \phi)$ is defined as the ratio of its radiated power density $s(\theta, \phi)$ to an ideal isotropic antenna.

$$d(\theta, \phi) = \frac{s(\theta, \phi)}{\frac{1}{4\pi} \int_0^{2\pi} \int_0^{\pi} s(\theta, \phi) \sin(\theta) d\theta d\phi} \tag{C.44}$$

For a monopole, with a uniform pattern in the azimuthal direction, this reduces to

$$d(\theta) = \frac{2s(\theta)}{\int_0^{\pi} s(\theta) \sin(\theta) d\theta} \tag{C.45}$$

where

$s(\theta) = \frac{1}{2}\sqrt{\frac{\mu_0}{\epsilon_0}}|H_\phi|^2 = \frac{1}{2}\sqrt{\frac{\epsilon_0}{\mu_0}}|E_\theta|^2$

H_ϕ, E_θ are the far-field electric and magnetic field intensities

$\sqrt{\frac{\mu_0}{\epsilon_0}}$ is the free space wave impedance $= 120\pi\ \Omega \approx 377\ \Omega$

From the numerical directivity, the directivity $D(\theta, \phi)$ of the antenna can be found

$$D(\theta, \phi) = 10 \log_{10} d(\theta, \phi)(\text{dBi}) \tag{C.46}$$

with a maximum directivity at $\theta = \frac{\pi}{2}$.

The directivity is related to the gain of the antenna through

$$G \text{ (dB)} = D \text{ (dB)} - \epsilon_R \text{ (dB)} \tag{C.47}$$

where

ϵ_R is the efficiency of the antenna.

And antenna efficiency is

$$\epsilon_e = \frac{P_{radiated}}{P_{input}} \tag{C.48}$$

The total time-averaged radiated power P_{total} of the antenna is given by

$$\begin{aligned} P_{total} &= \int_0^{2\pi} \int_0^{\pi} s(\theta, \phi) r^2 \sin(\theta) d\theta d\phi \\ &= 2\pi r^2 \int_0^{\pi} s(\theta) \sin(\theta) d\theta \end{aligned} \tag{C.49}$$

The antenna radiation resistance R_{rad} is given by

$$R_{rad} = \frac{2P_{total}}{|I(z=0)|^2} \tag{C.50}$$

The input impedance of the antenna is defined as

$$Z_{in} = R_{in} + jX_{in} \tag{C.51}$$

where

$$R_{in} = R_{rad} + R_{ohmic} \tag{C.52}$$

Assuming the ground plane and the antenna element both have infinite conductivity

$$R_{ohmic} = 0$$

$$\therefore \; R_{in} = R_{rad} \tag{C.53}$$

The generic exact form of the E and H fields are

$$H_\phi = \frac{jI(0)}{4\pi\rho\sin(kh)}\left[\exp(-jkr_0) - \cos(kh)\exp(-jkr) - \left(\frac{jz}{r}\right)\sin(kh)\times\exp(-jkr)\right] \tag{C.54}$$

$$\begin{aligned} E_\rho &= \frac{jI(0)\eta}{4\pi\rho\sin(kh)}\left\{\frac{(z-h)\exp(-jkr_0)}{r_0} - \frac{z}{r}\cos(kh)\exp(-jkr) + \sin(kh)\frac{\partial}{\partial z}\left[\frac{z}{kr}\exp(-jkr)\right]\right\} \\ &= \frac{jI(0)\eta}{4\pi\rho\sin(kh)}\left\{\frac{(z-h)\exp(-jkr_0)}{r_0} - \frac{z}{r}\cos(kh)\exp(-jkr)\right. \\ &\qquad \left. + \sin(kh)\exp(-jkr)\left(\frac{1}{kr} - \frac{z^2}{kr^3} - \frac{jz^2}{r^2}\right)\right\} \end{aligned} \tag{C.55}$$

$$\begin{aligned} E_z &= \frac{-jI(0)\eta}{4\pi\sin(kh)}\left\{\frac{\exp(-jkr_0)}{r_0} - \cos(kh)\frac{\exp(-jkr)}{r} + \sin(kh)\frac{\partial}{\partial z}\left[\frac{\exp(-jkr)}{kr}\right]\right\} \\ &= \frac{-jI(0)\eta}{4\pi\sin(kh)}\left[\frac{\exp(-jkr_0)}{r_0} - \cos(kh)\frac{\exp(-jkr)}{r} - z\sin(kh)\exp(-jkr)\left(\frac{j}{r^2} + \frac{1}{kr^3}\right)\right] \end{aligned} \tag{C.56}$$

where

$$r_0 = [\rho^2 + (z-h)^2]^{1/2}$$

$$r = (\rho^2 + z^2)^{1/2}$$

When in the far field, these can be approximated to

$$H_\phi = \frac{jI(0)\exp(-jkr)}{4\pi r \sin(\theta)\sin(kh)}\left[\exp(jkh\cos(\theta)) - \cos(kh) - j\cos(\theta)\sin(kh)\right] \quad \text{(C.57)}$$

$$E_\rho = \frac{jI(0)\eta\cos(\theta)\exp(-jkr)}{4\pi r \sin(\theta)\sin(kh)}\left[\exp(jkh\cos(\theta)) - j\cos(\theta)\sin(kh)\right] \quad \text{(C.58)}$$

$$E_z = \frac{-jI(0)\eta\exp(-jkr)}{4\pi r \sin(kh)}\left[\exp(jkh\cos(\theta)) - j\cos(\theta)\sin(kh)\right] \quad \text{(C.59)}$$

For an infinitely large ground plane, the current along the monopole is assumed to be

$$I(z) = I_0\frac{sin[k(h-z)]}{\sin(kh)} \quad 0 \le z \le h \quad \text{(C.60)}$$

where

h is the monopole height

$k = \frac{2\pi}{\lambda}$ is the wave number

$I_0 = I(z=0) = I(0)$ is the current magnitude at position $z = 0$

Now, the exact closed-form expression for H and E are given as

$$H_\phi = \begin{cases} \frac{jI(0)}{4\pi\rho\sin(kh)}\left[\exp(-jkR_1) + \exp(-jkR_2) - 2\cos(kh)\exp(-jkr)\right], & z \geq 0 \\ 0, & z < 0 \end{cases} \tag{C.61}$$

$$E_\rho = \begin{cases} \frac{j\eta I(0)}{4\pi\rho\sin(kh)}\left[\frac{(z-h)\exp(-jkR_1)}{R_1} + \frac{(z+h)\exp(-jkR_2)}{R_2} - 2z\cos(kh)\frac{-jkr}{r}\right], & z \geq 0 \\ 0, & z < 0 \end{cases} \tag{C.62}$$

$$E_z = \begin{cases} \frac{-j\eta I(0)}{4\pi\sin(kh)}\left[\frac{-jkR_1}{R_1} + \frac{-jkR_2}{R_2} - 2\cos(kh)\frac{-jkr}{r}\right], & z \geq 0 \\ 0, & z < 0 \end{cases} \tag{C.63}$$

where

$$\eta = \frac{k}{w\epsilon_0} = \sqrt{\frac{\mu_0}{\epsilon_0}} = 120\pi\ \Omega$$

$$R_1 = \sqrt{\rho^2 + (z-h)^2}$$

$$R_2 = \sqrt{\rho^2 + (z+h)^2}$$

The far field region, defined as the region satisfying the conditions

$$h \ll r \tag{C.64}$$

$$kr \gg 1 \tag{C.65}$$

$$\frac{kh^2}{2r} \ll 2\pi \tag{C.66}$$

Simplifies the E and H fields to $H = \hat{u_\phi} H_\phi$ and $E = \hat{u_\theta} E_\theta = \hat{u_\theta} \eta H_\theta$ where $\hat{u}$ is the respective unit vector:

$$H_\phi = \begin{cases} \frac{jI(0)\exp(-jkr)}{2\pi r \sin(\theta)\sin(kh)} \left[\frac{\cos(kh\cos(\theta)) - \cos(kh)}{\sin(\theta)}\right], & 0 \leq \theta \leq \frac{\pi}{2} \\ 0, & \frac{\pi}{2} < \theta \leq \pi \end{cases} \tag{C.67}$$

With these fields, the time-averaged Poynting vector can be defined as

$$S = \frac{1}{2}(E \times H) = \frac{1}{2}(\hat{u_\theta} E_\theta \times \hat{u_\phi} H_\phi) = \hat{u_r} s(\theta) \tag{C.68}$$

where $s(\theta)$ is the time-averaged radiated power density given by

$$s(\theta) = \frac{\eta}{2}|H_\phi|^2 = \frac{\eta|I(0)|^2}{8\pi^2 r^2 \sin^2(kh)}\left[\frac{\cos(kh\cos(\theta)) - \cos(kh)}{\sin(\theta)}\right]^2, \qquad 0 \le \theta \le \frac{\pi}{2} \tag{C.69}$$

$$= 0, \qquad \frac{\pi}{2} < \theta \le \pi \tag{C.70}$$

Therefore, the radiation resistance of an infinitely thin element is given by

$$R_{rad} = \frac{\eta}{4\pi \sin^2(kh)}\{\mathrm{Cin}(2kh) + \frac{1}{2}\sin(2kh)\left[\mathrm{Si}(4kh) - 2\mathrm{Si}(2kh)\right] \tag{C.71}$$

$$+ \frac{1}{2}\cos(2kh)\left[2\mathrm{Cin}(2kh) - \mathrm{Cin}(4kh)\right]\} \tag{C.72}$$

where $\mathrm{Cin}(z)$ is the modified cosine integral:

$$\int_0^z \frac{dt}{t}\left(1 - \cos(t)\right) \tag{C.73}$$

and $\mathrm{Si}(x)$ is the sine integral:

$$\int_0^x \frac{\sin(t)}{t} \tag{C.74}$$

The numerical directivity can now be simplified to

$$d(\theta) = \frac{4}{B}\left[\frac{\cos(kh\cos(\theta)) - \cos(kh)}{\sin(\theta)}\right]^2 \tag{C.75}$$

where

$$B = \mathrm{Cin}(2kh) + \frac{1}{2}\sin(2kh)\left[\mathrm{Si}(4kh) - 2\mathrm{Si}(2kh)\right] + \frac{1}{2}\cos(2kh)\left[2\mathrm{Cin}(2kh) - \mathrm{Cin}(4kh)\right]$$

Also, the input reactance of the antenna for thin elements is given by

$$\begin{aligned} X_{in} = & \frac{\eta}{4\pi\sin^2(kh)}\Bigg\{\mathrm{Si}(2kh) + \cos(2kh)\left[\mathrm{Si}(2kh) - \frac{1}{2}\mathrm{Si}(4kh)\right] \\ & - \sin(2kh)\left[ln\left(\frac{h}{b}\right) - \mathrm{Cin}(2kh) + \frac{1}{2}\mathrm{Cin}(4kh) + \frac{1}{2}\mathrm{Cin}\left(\frac{kb^2}{h}\right)\right]\Bigg\} \end{aligned} \tag{C.76}$$

For a quater-wave monopole ($h = \frac{\lambda}{4}$; $kh = \frac{\pi}{2}$), Eqns. C.72 and C.75 simplify to

$$R_{rad} = \frac{\eta}{4\pi}\frac{\mathrm{Cin}(2\pi)}{2} = 36.54\Omega \tag{C.77}$$

$$d(\theta) = \frac{4\cos^2\left[\frac{\pi}{2}\cos(\theta)\right]}{\sin^2(\theta)}\frac{2}{\mathrm{Cin}(2\pi)}, \quad kh = \frac{\pi}{2} \tag{C.78}$$

$$X_{in} = 21.2576\Omega \tag{C.79}$$

With the peak directivity at $\theta = \frac{\pi}{2}$, $d(\frac{\pi}{2}) = 3.2818 \therefore D(\frac{\pi}{2}) = 10\log_{10}(d(\frac{\pi}{2})) = 5.1612$ dBi. This follows image theory that a quarter-wave monopole will have half the input impedance and twice the directivity of a half-wave dipole.

$$Z_{mono} = \frac{V_{mono}}{I_{mono}} = \frac{\frac{1}{2}V_{dipole}}{I_{dipole}} = \frac{1}{2}Z_{dipole} \tag{C.80}$$

$$D_{mono} = \frac{U_m}{\frac{1}{2}\frac{P}{4\pi}} = 2\frac{U_m}{\frac{P}{4\pi}} = 2\frac{U_m}{U_{avg}} = 2D_{dipole} \tag{C.81}$$

where

U_m is the maximum radiation intensity in free space

As shown in [11], the radiation resistance and directivity are dependent on the radius of the ground plane; with a large ($ka > 30$ radians) ground plane rather than an infinite one, the input impedance can be found as

$$Z_{in} - Z_{\infty} = \frac{-j\eta \exp(j2ka)}{4\pi ka} \left[\frac{1-\cos(kh)}{\sin(kh)}\right]^2 \times \left\{1 + \frac{\exp\left[j(2ka + \frac{3\pi}{4})\right]}{\sqrt{4\pi ka}}\right\}^{-1} \quad \text{(C.82)}$$

where

Z_{in} is the input impedance for an element on a ground plane of radius ka rad

Z_{∞} is the input impedance for an element on a ground plane of radius $ka = \infty$ radians

which can be approximated by

$$R_{in} - R_{\infty} \approx \left[\frac{1-\cos(kh)}{\sin(kh)}^2 \frac{\sin(2ka)}{4\pi ka}\right] \quad \text{(C.83)}$$

$$X_{in} - X_{\infty} \approx \left[\frac{1-\cos(kh)}{\sin(kh)}^2 \frac{\cos(2ka)}{4\pi ka}\right] \quad \text{(C.84)}$$

Appendix D

Bi-Directional Coupler Analysis [1]

A directional coupler is a four-port device that isolates one port from the input port and one port from the output port. The four ports include an "input" port where the signal is injected, a "through" port where the signal exits, a "coupled" port where a fraction of the input signal appears, an "isolated" port that is cut off from the input port. Normally for a directional coupler the isolated port is terminated with a matched load, however in this case the isolated port is utilized because it couples with the output port just as the coupled port couples with the input port. Fig. D.1 shows a basic schematic for a directional coupler with port 1 being the input port, port 2 being the through port, port 3 being the coupled port and port 4 being the isolated port. In an ideal directional coupler, all ports are matched, the circuit is lossless and the power into port 1 will only appear in ports 2 and 3. In actuality, some of the power leaks into port 4, leading to a directivity of the device.

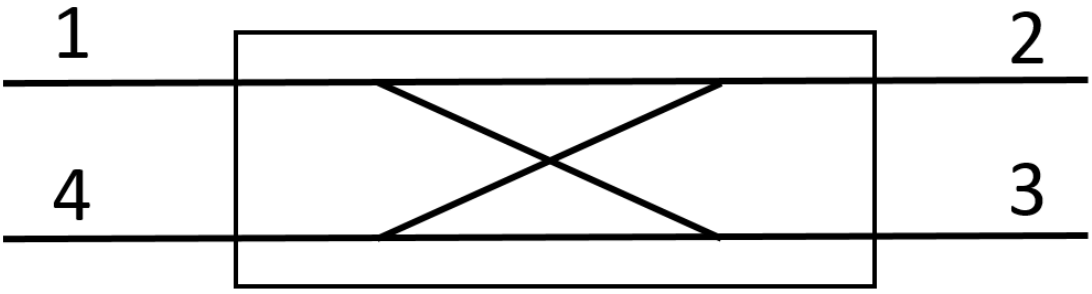

Figure D.1: Generic Directional Coupler Schematic

$$\text{Insertion Loss (IL)} = 10\log\left(\frac{P_1}{P_2}\right) = -20\log(|s_{21}|) \tag{D.1}$$

$$\text{Isolation (I)} = 10\log\left(\frac{P_1}{P_4}\right) = -20\log(|s_{41}|) \tag{D.2}$$

$$\text{Coupling (C)} = 10\log\left(\frac{P_1}{P_3}\right) = -20\log(|s_{31}|) \tag{D.3}$$

$$\text{Directivity (D)} = 10\log\left(\frac{P_3}{P_4}\right) = 20\log\left(\frac{|s_{31}|}{|s_{41}|}\right) \tag{D.4}$$

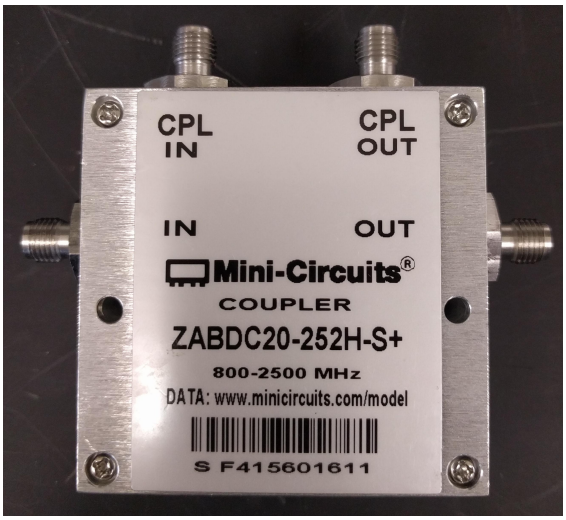

Figure D.2: Picture of Bi-directional Coupler

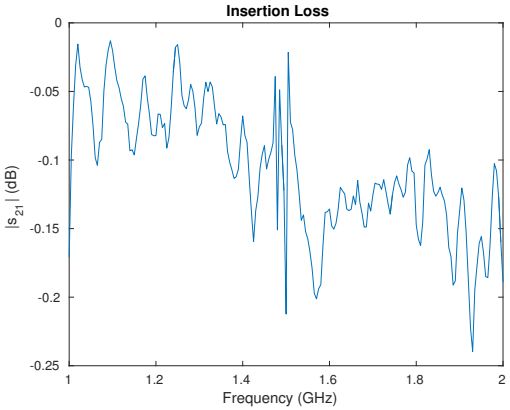

Figure D.3: Bi-directional Coupler: Insertion Loss (dB)

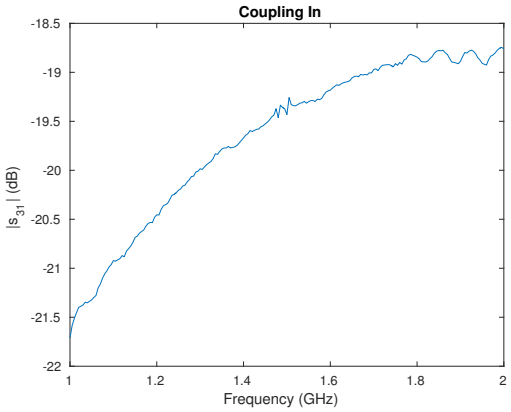

Figure D.4: Bi-directional Coupler: Couple-In Port (dB)

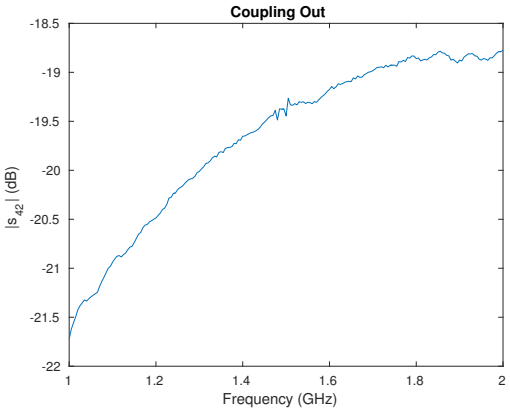

Figure D.5: Bi-directional Coupler: Couple-Out Port (dB)

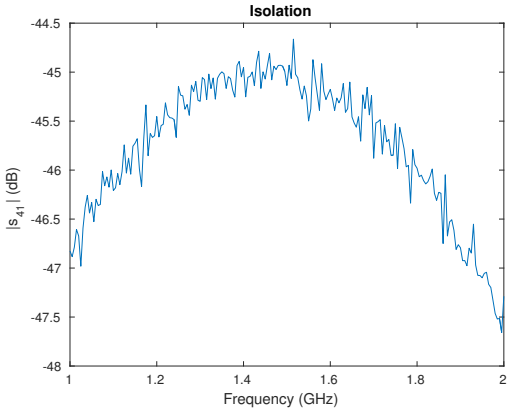

Figure D.6: Bi-directional Coupler: Isolation (dB)

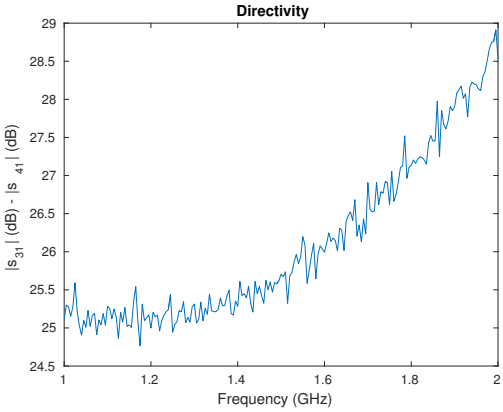

Figure D.7: Bi-directional Coupler: Directivity (dB)

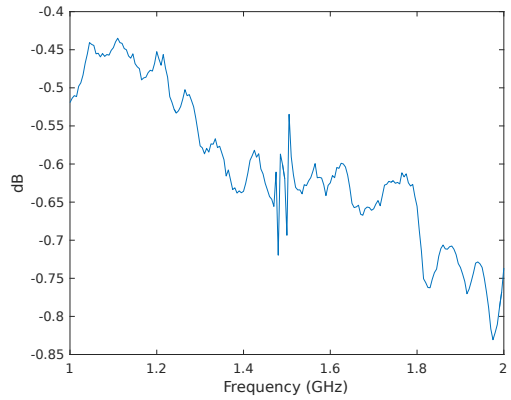

Figure D.8: Two Meter Coaxial Cable Loss (dB)

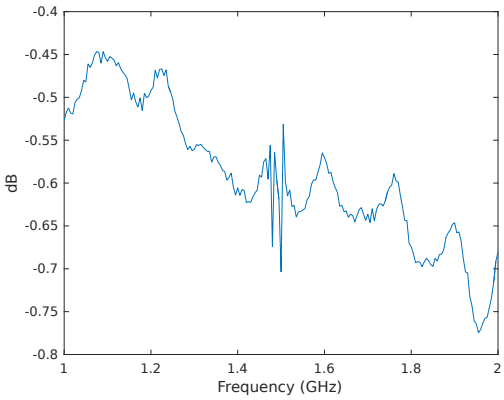

Figure D.9: One Meter Coaxial Cable Loss (dB)

Appendix E

Monopole Impedance Measurements

In this section, two other methods of displaying the antenna impedance are presented. Figures E.1a-E.3c show Smith Chart representations of the normalized impedance. Smith Charts are a great tool in visualizing the antenna input impedance as a function of frequency. The Smith Charts in this section were all normalized to a characteristic impedance of $Z_0 = 50\ \Omega$. Figures E.4a-E.6c display linear plots of the real and imaginary components of the antenna input impedance with and without the Wheeler Cap in place.

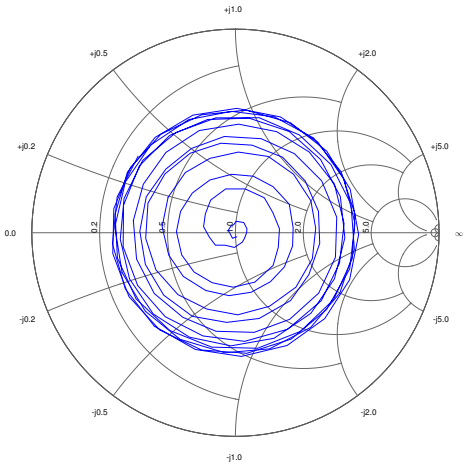

(a) Bottom-Fed Monopole Antenna Input Impedance at 1 GHz

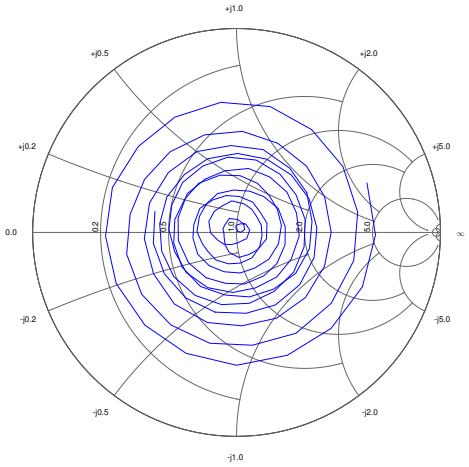

(b) Bottom-Fed Monopole Antenna Input Impedance at 1.5 GHz

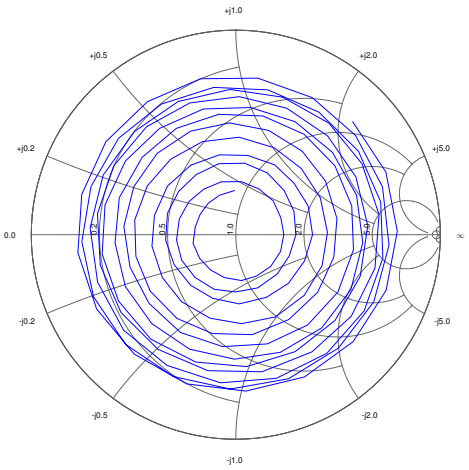

(c) Bottom-Fed Monopole Antenna Input Impedance at 2 GHz

Figure E.1: Bottom Fed Monopole Antenna - Input Impedance

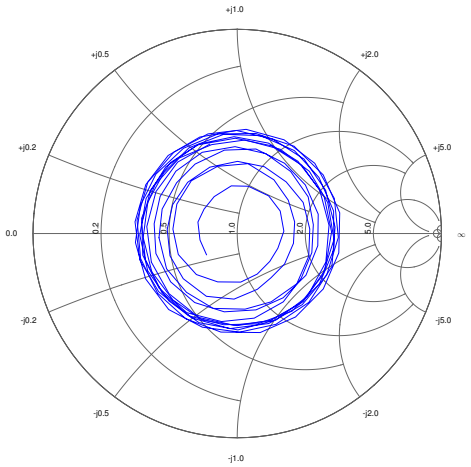

(a) Bottom-Fed with Injection Stub Monopole Antenna Input Impedance at 1 GHz

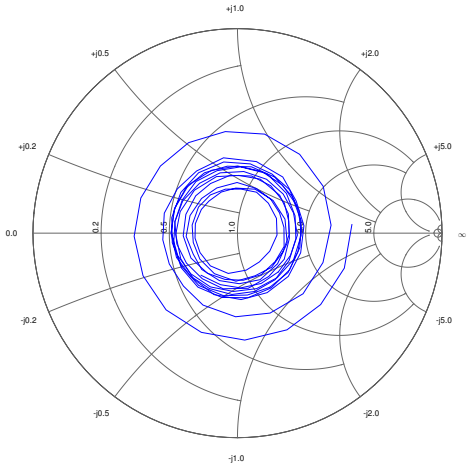

(b) Bottom-Fed with Injection Stub Monopole Antenna Input Impedance at 1.5 GHz

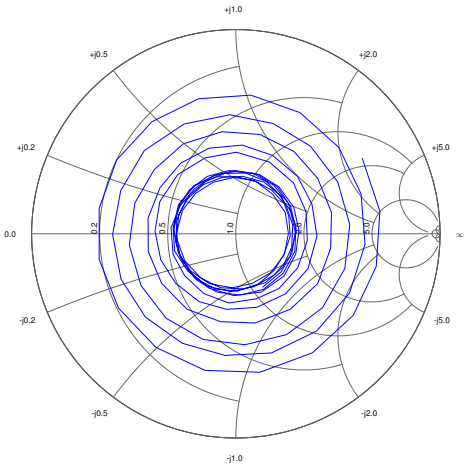

(c) Bottom-Fed with Injection Stub Monopole Antenna Input Impedance at 2 GHz

Figure E.2: Bottom-Fed with Injection Stub Monopole Antenna - Input Impedance

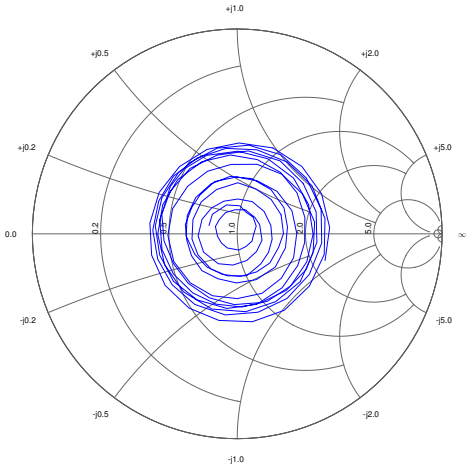

(a) Offset-Fed Monopole Antenna Input Impedance at 1 GHz

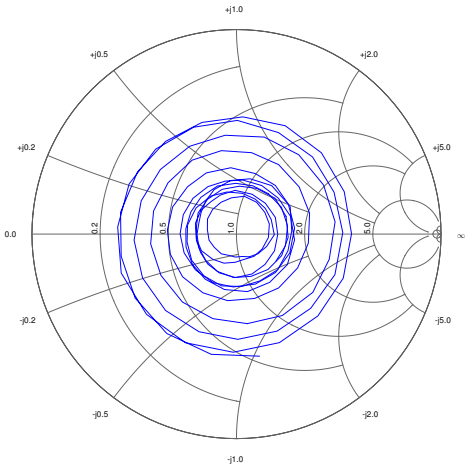

(b) Offset-Fed Monopole Antenna Input Impedance at 1.5 GHz

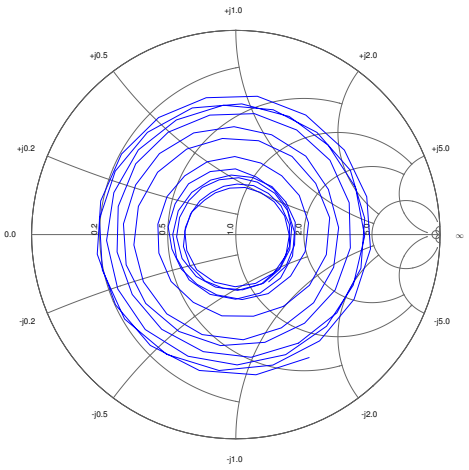

(c) Offset-Fed Monopole Antenna Input Impedance at 2 GHz

Figure E.3: Offset-Fed Monopole Antenna - Input Impedance

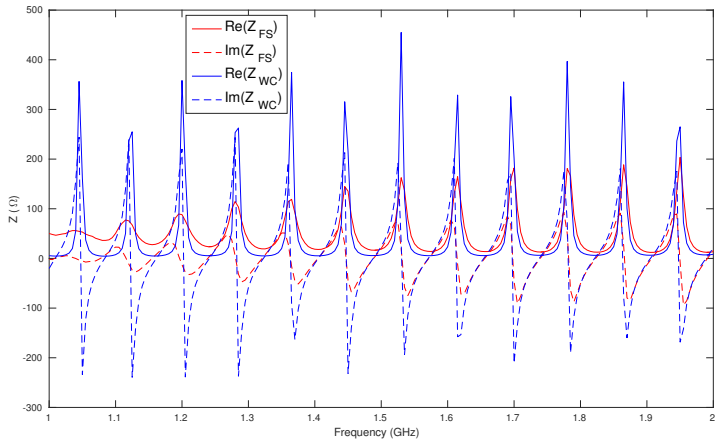

(a) Bottom-Fed Monopole Antenna Input Impedance at 1 GHz

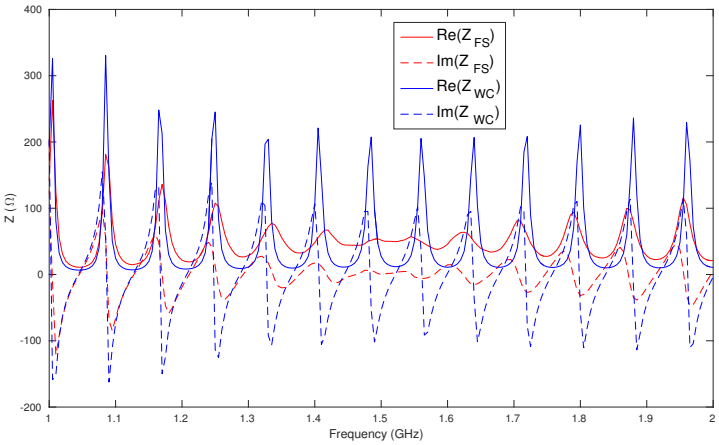

(b) Bottom-Fed Monopole Antenna Input Impedance at 1.5 GHz

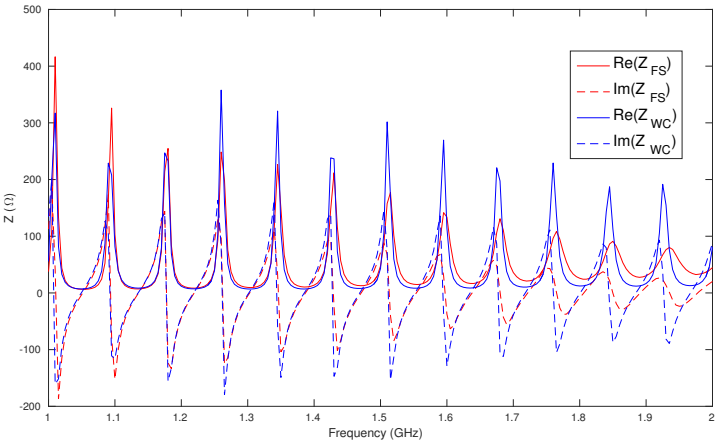

(c) Bottom-Fed Monopole Antenna Input Impedance at 2 GHz

Figure E.4: Bottom-Fed Monopole Antenna - Input Impedance

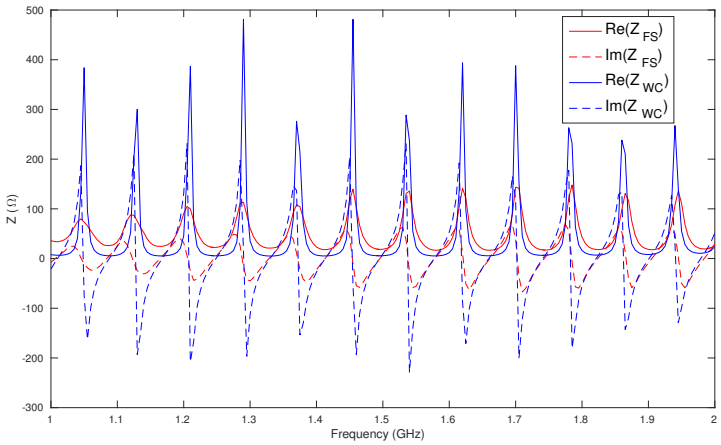

(a) Bottom-Fed with Injection Stub Monopole Antenna Input Impedance at 1 GHz

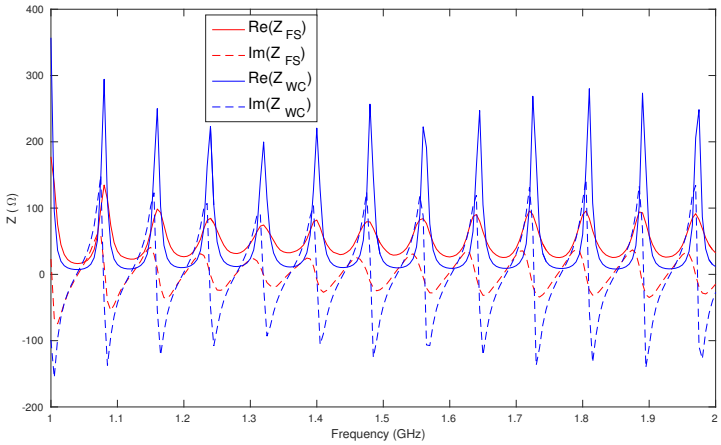

(b) Bottom-Fed with Injection Stub Monopole Antenna Input Impedance at 1.5 GHz

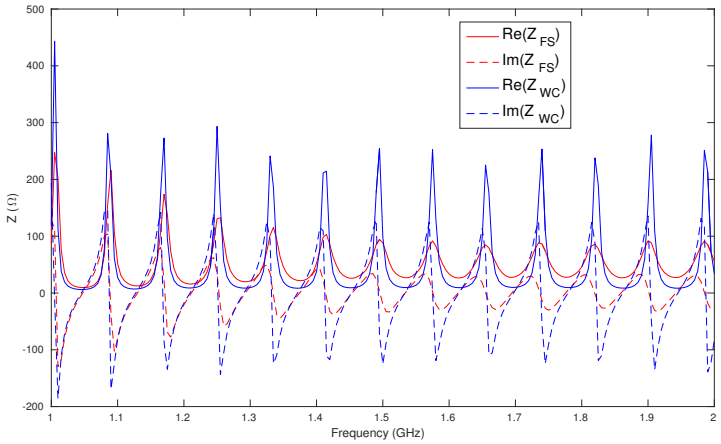

(c) Bottom-Fed with Injection Stub Monopole Antenna Input Impedance at 2 GHz

Figure E.5: Bottom-Fed with Injection Stub Monopole Antenna - Input Impedance

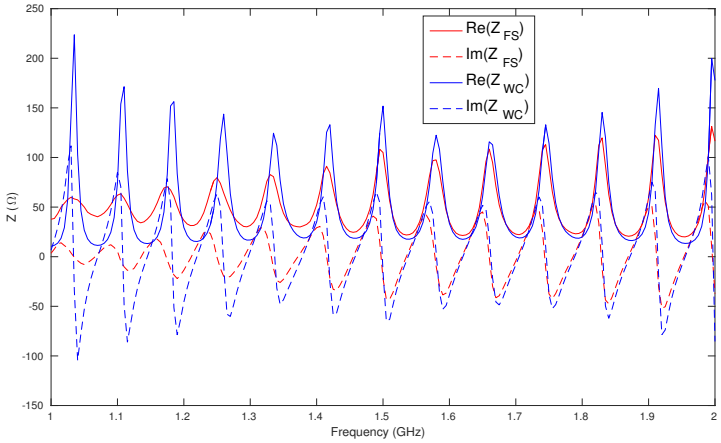

(a) Offset-Fed Monopole Antenna Input Impedance at 1 GHz

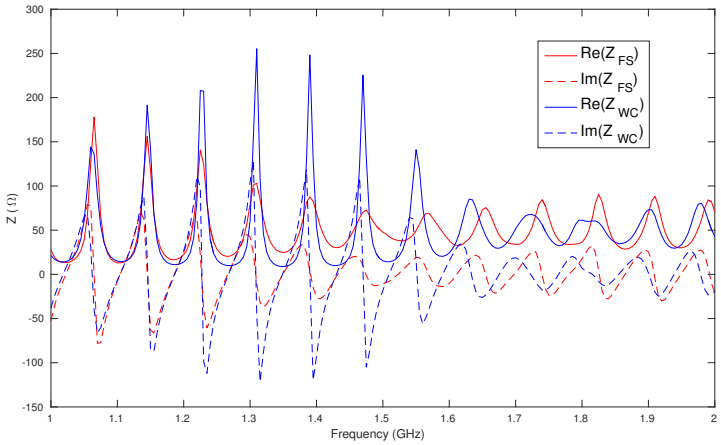

(b) Offset-Fed Monopole Antenna Input Impedance at 1.5 GHz

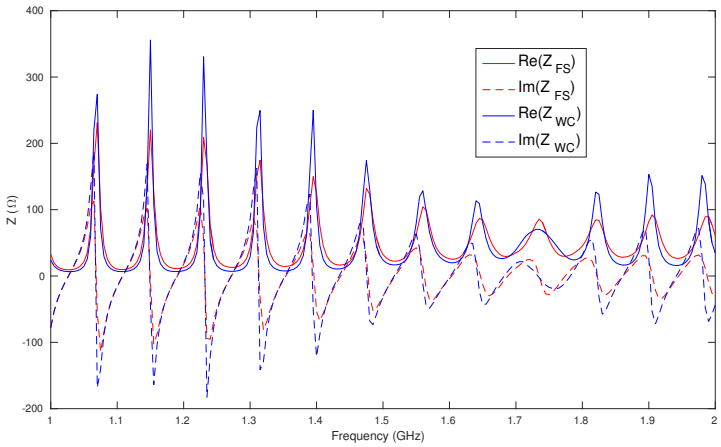

(c) Offset-Fed Monopole Antenna Input Impedance at 2 GHz

Figure E.6: Offset-Fed Monopole Antenna - Input Impedance

Appendix F

FEKO Limitations & Assumptions

Some assumptions were needed to be made when doing the FEKO simulations of the described antennas. The tutorials for FEKO all make a dipole or monopole antenna using a wire geometry, but this assumes the antenna is made from a very thin wire. Therefore, to correctly model the size of the inner diameter of the tubing used to build the prototype antennas, a cylinder geometry was used to model the antenna. Using a cylinder instead of a wire for the antenna meant that the port feed became a thin wire connected to a thick cylinder. An edge feed was also tested, but the return loss when using this feed type was not acceptable. Another assumption made was with the helix antenna. FEKO provides a helix geometry, but this geometry is also made from a thin wire. This means that a thick helix cannot be modeled effectively in FEKO that will have an effect on the comparison between simulation and experimental results. Also, liquid conductors could not be simulated using this

software. Therefore the effect of the conductor being a liquid instead of a solid will cause irregularities in the comparison results. From the experiments run, it appears this difference is not drastic. The student version of the software is severely limited in terms of the model elements, the solution specifications and the solution metrics. When modeling larger antenna arrays, the student version has too many limitations to properly analyze the antenna.

Bibliography

[1] D. M. Pozar, *Microwave engineering*, 4th ed. Wiley, 2012.

[2] R. W. Powell, "The electrical resistivity of gallium and some other anisotropic properties of this metal," *Proceedings of the Royal Society A: Mathematical, Physical and Engineering Sciences*, vol. 209, no. 1099, pp. 525–541, 1951.

[3] R. Fogelholm, O. Rapp, and G. Grimvall, "Electrical resistivity of indium: Deviation from linearity at high temperatures," *Physical Review B*, vol. 23, no. 8, pp. 3845–3851, 1981.

[4] D. J. Griffiths, *Introduction to electrodynamics*, 4th ed. Pearson Education, 2012.

[5] W. Wang and Z. Jiang, "Design and construction of a wheeler cap test set-up," Master's Thesis, University of Gavle, 09 2010.

[6] H. Wheeler, "The radiansphere around a small antenna," *Proceedings of the IRE*, vol. 47, no. 8, pp. 1325–1331, 1959.

[7] R. Johnston and J. McRory, "An improved small antenna radiation-efficiency measurement method," *IEEE Antennas and Propagation Magazine*, vol. 40, no. 5, pp. 40–48, 1998.

[8] D. Agahi and W. Domino, "Efficiency measurements of portable-handset antennas using the wheeler cap," RF Cafe. [Online]. Available: http://www.rfcafe.com/references/articles/Efficiency-Measurement-Antenna-Wheeler-Cap.htm

[9] J. Zhang, S. Pivnenko, and O. Breinbjerg, "A modified wheeler cap method for radiation efficiency measurement of balanced electrically small antennas,"

Proceedings of the Fourth European Conference on Antennas and Propagation, pp. 1–5, April 2010.

[10] Q. Garca-Garca, "Patch-antenna efficiency based on wheeler cap and measured q factor," *Microwave and Optical Technology Letters*, vol. 40, no. 2, pp. 132–142, 2003.

[11] M. M. Weiner, *Monopole antennas*, 1st ed. Marcel Dekker, 2003.

[12] C. A. Balanis, *Antenna theory: analysis and design*. Wiley Interscience, 2005.

[13] W. L. Stutzman and G. A. Thiele, *Antenna theory and design*, 2nd ed. Wiley, 1998.

[14] D. H. Staelin, *Electromagnetics and Applications*, 1st ed. Massachusetts Institute of Technology (MIT), 2011. [Online]. Available: https://ocw.mit.edu/courses/electrical-engineering-and-computer-science/6-013-electromagnetics-and-applications-spring-2009/readings/MIT6_013S09_notes.pdf

[15] *United States Frequency Allocations - The Radio Spectrum*. National Telecommunications and Information Administration (NTIA), 2016. [Online]. Available: https://www.ntia.doc.gov/files/ntia/publications/january_2016_spectrum_wall_chart.pdf

[16] M. D. Dickey *et al.*, "Eutectic gallium-indium (EGaIn): A liquid metal alloy for the formation of stable structures in microchannels at room temperature," Harvard SEAS Soft Matter Wiki. [Online]. Available: http://soft-matter.seas.harvard.edu/index.php/Eutectic_Gallium-Indium_(EGaIn):_A_Liquid_Metal_Alloy_for_the_Formation_of_Stable_Structures_in_Microchannels_at_Room_Temperature

[17] *ASM Handbook*. ASM International, 2012.

[18] M. Pourbaix, *Atlas of electrochemical equilibria in aqueous solutions*, 1st ed. Pergamon Press, 1966.

[19] A. Davidson, "Aluminum: A potential solution to the grid storage problem," p. 41, 2016. [Online]. Available: http://slideplayer.com/slide/10652587/

[20] P. Bevelacqua, "Helical antenna (helix antenna)," Antenna Theory, 2009. [Online]. Available: http://www.antenna-theory.com/antennas/travelling/helix.php

[21] "IEEE standard for definitions of terms for antennas," *IEEE Std 145-2013 (Revision of IEEE Std 145-1993)*, pp. 1–50, March 2014.

[22] A. S. Kholapure and R. G. Karandikar, "Emerging techniques for printed reconfigurable antenna: a review," *2016 Second International Conference on Research in Computational Intelligence and Communication Networks (ICRCICN)*, pp. 57–61, Sept 2016.

[23] A. Petosa, "An overview of tuning techniques for frequency-agile antennas," *IEEE Antennas and Propagation Magazine*, vol. 54, no. 5, pp. 271–296, Oct 2012.

[24] S. Phadte, "Reconfigurable antenna methodologies and switch technologies: a review," *International Journal of Innovative Research and Development*, vol. 5, no. 2, 2016. [Online]. Available: http://www.ijird.com/index.php/ijird/article/view/86182

[25] T. Debogovic and J. Perruisseau-Carrier, "MEMS - reconfigurable metamaterials and antenna applications," *International Journal of Innovative Research and Development*, 2014. [Online]. Available: https://www.hindawi.com/journals/ijap/2014/138138/

[26] Y. Yashchyshyn, "Reconfigurable antennas by RF switches technology," *2009 5th International Conference on Perspective Technologies and Methods in MEMS Design*, pp. 155–157, April 2009.

[27] C. G. Christodoulou, Y. Tawk, S. A. Lane, and S. R. Erwin, "Reconfigurable antennas for wireless and space applications," *Proceedings of the IEEE*, vol. 100, no. 7, pp. 2250–2261, July 2012.

[28] P. D. Grant, M. W. Denhoff, and R. R. Mansour, "A comparison between RF MEMS switches and semiconductor switches," *MEMS, NANO and Smart Systems, 2004. ICMENS 2004. Proceedings. 2004 International Conference on*, pp. 515–521, Aug 2004.

[29] C. A. Balanis, *Modern Antenna Handbook*, 1st ed. Wiley, 2008.

[30] T. Liu, P. Sen, and C. J. Kim, "Characterization of nontoxic liquid-metal alloy galinstan for applications in microdevices," *Journal of Microelectromechanical Systems*, vol. 21, no. 2, pp. 443–450, April 2012.

[31] X. Liu, L. P. B. Katehi, and D. Peroulis, "Non-toxic liquid metal microstrip resonators," *2009 Asia Pacific Microwave Conference*, pp. 131–134, Dec 2009.

[32] M. D. Dickey *et al.*, "Eutectic gallium-indium (EGaIn): A liquid metal alloy for the formation of stable structures in microchannels at room temperature," *Advanced Functional Materials*, vol. 18, no. 7, pp. 1097–1104, 2008. [Online]. Available: http://dx.doi.org/10.1002/adfm.200701216

[33] C. Karcher, V. Kocourek, and D. Schulze, "Experimental investigations of electromagnetic instabilities of free surfaces in a liquid metal drop," *International Scientific Colloquium Modelling for Electromagnetic Processing*, 2003. [Online]. Available: http://sci-toys.com/scitoys/scitoys/thermo/liquid_metal/oscillations_in_galinstan.pdf

[34] M. R. Khan, "Engineering the yield properties of the oxide skin on a liquid metal alloy," Master's Thesis, North Carolina State University, 2011.

[35] J.-H. So, "Controlling the shape and interfacial properties of eutectic gallium indium," Ph.D. Dissertation, North Carolina State University, 2012.

[36] Z. Wu, K. Hjort, and S. H. Jeong, "Microfluidic stretchable radio-frequency devices," *Proceedings of the IEEE*, vol. 103, no. 7, pp. 1211–1225, July 2015.

[37] "Cesium (Cs) - chemical properties, health and environmental effects," Lenntech, 2017. [Online]. Available: http://www.lenntech.com/periodic/elements/cs.htm

[38] "Cesium," PubChem Open Chemistry Database, 2017. [Online]. Available: https://pubchem.ncbi.nlm.nih.gov/compound/cesium#section=Top

[39] "Rubidium," ESPI Metals, 2017. [Online]. Available: http://www.espimetals.com/index.php/technical-data/193-Rubidium

[40] "Technical data sheet: Sodium-potassium alloy (NaK)," BASF Corporation, 2003. [Online]. Available: http://worldaccount.basf.com/wa/NAFTA~en_GB/Catalog/ChemicalsNAFTA/doc4/BASF/PRD/30230091/.pdf?urn=urn:documentum:eCommerce_sol_EU:09007bb280047733.pdf

[41] O. J. Foust, *Sodium-NaK engineering handbook*, 1st ed. Gordon and Breach, 1972.

[42] P. T. Cummings, "Shear viscosity of liquid rubidium at the triple point," *Journal of Physics F: Metal Physics*, vol. 18, no. 7, pp. 1439–1447, 1988.

[43] E. N. da C. Andrade and E. R. Dobbs, "The viscosities of liquid lithium, rubidium and caesium," *Proceedings of the Royal Society A: Mathematical, Physical and Engineering Sciences*, vol. 211, no. 1104, pp. 12–30, 1952.

[44] W. W. Strong, "On the possible radioactivity of erbium, potassium and rubidium," *Physical Review (Series I)*, vol. 29, no. 2, pp. 170–173, 1909.

[45] "Phased array antennas," Microwaves 101. [Online]. Available: https://www.microwaves101.com/encyclopedias/phased-array-antennas

[46] I. Rouissi, J. M. Floc'h, H. Rmili, and H. Trabelsi, "Design of a frequency reconfigurable patch antenna using capacitive loading and varactor diode," *2015 9th European Conference on Antennas and Propagation (EuCAP)*, pp. 1–4, May 2015.

[47] Y. Turki and R. Staraj, "CPW-fed frequency-agile shorted patch," *Microwave and Optical Technology Letters*, vol. 25, no. 5, p. 291, 2000.

[48] J. M. Carrere, R. Staraj, and G. Kossiavas, "Small frequency agile antennas," *Electronics Letters*, vol. 37, no. 12, pp. 728–729, Jun 2001.

[49] J. M. Floc'h and I. B. Trad, "Printed frequency reconfigurable planar inverted-f antenna for ISM applications," *2016 Loughborough Antennas Propagation Conference (LAPC)*, pp. 1–5, Nov 2016.

[50] C. Luxey, L. Dussopt, J. L. L. Sonn, and J. M. Laheurte, "Dual-frequency operation of CPW-fed antenna controlled by PIN diodes," *Electronics Letters*, vol. 36, no. 1, pp. 2–3, Jan 2000.

[51] Y. Cao, S. W. Cheung, and T. I. Yuk, "A simple planar polarization reconfigurable monopole antenna for GNSS/PCS," *IEEE Transactions on Antennas and Propagation*, vol. 63, no. 2, pp. 500–507, Feb 2015.

[52] Y. B. Chaouche *et al.*, "Design of reconfigurable fractal antenna using PIN diode switch for wireless applications," *2016 16th Mediterranean Microwave Symposium (MMS)*, pp. 1–4, Nov 2016.

[53] G. I. Kiani, K. P. Esselle, A. R. Weily, and K. L. Ford, "Active frequency selective surface using PIN diodes," *2007 IEEE Antennas and Propagation Society International Symposium*, pp. 4525–4528, June 2007.

[54] L. Ge, K. M. Luk, and S. Chen, "360 degree beam-steering reconfigurable wideband substrate integrated waveguide horn antenna," *IEEE Transactions on Antennas and Propagation*, vol. 64, no. 12, pp. 5005–5011, Dec 2016.

[55] X. Zhang, F. Yang, and P. Yang, "A beam-steering dual-polarization reconfigurable antenna," *2016 Progress in Electromagnetic Research Symposium (PIERS)*, pp. 414–417, Aug 2016.

[56] Y. Kim and Y. J. Yoon, "A high gain pattern reconfigurable antenna with simple structure," *2016 IEEE International Symposium on Antennas and Propagation (APSURSI)*, pp. 653–654, June 2016.

[57] S. Genovesi *et al.*, "Frequency-reconfigurable microstrip antenna with biasing network driven by a PIC microcontroller," *IEEE Antennas and Wireless Propagation Letters*, vol. 11, pp. 156–159, 2012.

[58] L. N. Pringle *et al.*, "A reconfigurable aperture antenna based on switched links between electrically small metallic patches," *IEEE Transactions on Antennas and Propagation*, vol. 52, no. 6, pp. 1434–1445, June 2004.

[59] X. Yang, J. Lin, G. Chen, and F. L. Kong, "Frequency reconfigurable antenna for wireless communications using GaAs FET switch," *IEEE Antennas and Wireless Propagation Letters*, vol. 14, pp. 807–810, Dec 2015.

[60] "Introduction to microelectromechanical systems (MEMS)," Bringham Young University Compliant Mechanisms Research. [Online]. Available: https://compliantmechanisms.byu.edu/content/introduction-microelectromechanical-systems-mems

[61] D. Anagnostou, M. Khodier, J. C. Lyke, and C. G. Christodoulou, "Fractal antenna with RF MEMS switches for multiple frequency applications," *IEEE Antennas and Propagation Society International Symposium (IEEE Cat. No.02CH37313)*, vol. 2, pp. 22–25 vol.2, 2002.

[62] D. E. Anagnostou *et al.*, "Design, fabrication, and measurements of an RF-MEMS-based self-similar reconfigurable antenna," *IEEE Transactions on Antennas and Propagation*, vol. 54, no. 2, pp. 422–432, Feb 2006.

[63] C. won Jung, M. Lee, G. P. Li, and F. De Flaviis, "Reconfigurable scan-beam single-arm spiral antenna integrated with RF-MEMS switches," *IEEE Transactions on Antennas and Propagation*, vol. 54, no. 2, pp. 455–463, Feb 2006.

[64] G. H. Huff and J. T. Bernhard, "Integration of packaged RF MEMS switches with radiation pattern reconfigurable square spiral microstrip antennas," *IEEE Transactions on Antennas and Propagation*, vol. 54, no. 2, pp. 464–469, Feb 2006.

[65] R. George, C. R. S. Kumar, and S. A. Gangal, "Design of a frequency reconfigurable pixel patch antenna for cognitive radio applications," *2016 International Conference on Communication and Signal Processing (ICCSP)*, pp. 1684–1688, April 2016.

[66] "Rotary switches," COM DEV International. [Online]. Available: http://www.meslmicrowave.com/rotary-switches/overview/

[67] C. J. Panagamuwa, A. Chauraya, and J. C. Vardaxoglou, "Frequency and beam reconfigurable antenna using photoconducting switches," *IEEE Transactions on Antennas and Propagation*, vol. 54, no. 2, pp. 449–454, Feb 2006.

[68] X. S. Yang, B. Z. Wang, W. Wu, and S. Xiao, "Yagi patch antenna with dual-band and pattern reconfigurable characteristics," *IEEE Antennas and Wireless Propagation Letters*, vol. 6, pp. 168–171, 2007.

[69] J. Gibson and S. V. Georgakopoulos, "Reconfigurable antenna using shape memory polymers," *2016 IEEE International Symposium on Antennas and Propagation (APSURSI)*, pp. 1673–1674, June 2016.

[70] L. Liu and R. J. Langley, "Liquid crystal tunable microstrip patch antenna," *Electronics Letters*, vol. 44, no. 20, pp. 1179–1180, September 2008.

[71] G. J. Hayes *et al.*, "Flexible liquid metal alloy (EGaIn) microstrip patch antenna," *IEEE Transactions on Antennas and Propagation*, vol. 60, no. 5, pp. 2151–2156, May 2012.

[72] S. Cheng *et al.*, "Foldable and stretchable liquid metal planar inverted cone antenna," *IEEE Transactions on Antennas and Propagation*, vol. 57, no. 12, pp. 3765–3771, Dec 2009.

[73] J.-H. So *et al.*, "Reversibly deformable and mechanically tunable fluidic antennas," *Advanced Functional Materials*, vol. 19, no. 22, pp. 3632–3637, 2009. [Online]. Available: http://dx.doi.org/10.1002/adfm.200900604

[74] B. J. Blaiszik *et al.*, "Autonomic restoration of electrical conductivity," *Advanced Materials*, vol. 24, no. 3, pp. 398–401, 2011.

[75] A. Vorobyov, C. Henemann, and P. Dallemagne, "Liquid metal based antenna for wearable electronic," *2016 10th European Conference on Antennas and Propagation (EuCAP)*, pp. 1–3, April 2016.

[76] D. M. Whitacre, *Reviews of environmental contamination and toxicology*, 229th ed. Springer International Publishing, 2014.

[77] A.-M. Florea and D. Busselberg, "Occurrence, use and potential toxic effects of metals and metal compounds," *BioMetals*, vol. 19, no. 4, pp. 419–427, 2006.

[78] "Sodium-potassium alloy: Technical data sheet," BASF, 2002. [Online]. Available: http://worldaccount.basf.com/wa/NAFTA~en_GB/Catalog/ChemicalsNAFTA/doc4/BASF/PRD/30230091/.pdf?urn=urn:documentum:eCommerce_sol_EU:09007bb280047733.pdf

[79] "Sodium-potassium alloy: Material safety data sheet," Callery Chemical Company, 2000. [Online]. Available: http://www.youngshin.com/wwwboard/data/3/NaK-MSDS.pdf

[80] "Indium metal: Material safety data sheet," Teck, 2013. [Online]. Available: https://wcam.engr.wisc.edu/Public/Safety/MSDS/Indium.pdf

[81] "Indium: Safety data sheet," ESPI Metals, 2016. [Online]. Available: http://www.espimetals.com/index.php/msds/146-Indium

[82] A. M. Morishita *et al.*, "A tunable amplifier using reconfigurable liquid-metal double-stub tuners," *Wireless and Microwave Circuits and Systems (WMCS), 2015 Texas Symposium on*, pp. 1–4, April 2015.

[83] K. Ling, H. K. Kim, M. Yoo, and S. Lim, "Frequency-switchable metamaterial absorber injecting eutectic gallium-indium (egain) liquid metal alloy," *Sensors*, vol. 15, no. 11, p. 28154, 2015. [Online]. Available: http://www.mdpi.com/1424-8220/15/11/28154

[84] M. R. Khan *et al.*, "A pressure responsive fluidic microstrip open stub resonator using a liquid metal alloy," *IEEE Microwave and Wireless Components Letters*, vol. 22, no. 11, pp. 577–579, Nov 2012.

[85] W. M. Zhu *et al.*, "Metamaterial tunable filter with liquid metal," *Micro Electro Mechanical Systems (MEMS), 2013 IEEE 26th International Conference on*, pp. 725–728, Jan 2013.

[86] R. C. Gough *et al.*, "Reconfigurable coupled-line bandpass filter with electrically actuated liquid-metal tuning," *2014 Asia-Pacific Microwave Conference*, pp. 932–934, Nov 2014.

[87] A. T. Ohta *et al.*, "A liquid-metal tunable electromagnetic-bandgap microstrip filter," *Wireless Information Technology and Systems (ICWITS), 2012 IEEE International Conference on*, pp. 1–4, Nov 2012.

[88] G. Mumcu, A. Dey, and T. Palomo, "Frequency-agile bandpass filters using liquid metal tunable broadside coupled split ring resonators," *IEEE Microwave and Wireless Components Letters*, vol. 23, no. 4, pp. 187–189, April 2013.

[89] J. H. Dang *et al.*, "A tunable x-band substrate integrated waveguide cavity filter using reconfigurable liquid-metal perturbing posts," *2015 IEEE MTT-S International Microwave Symposium*, pp. 1–4, May 2015.

[90] W. G. Tonaki, W. Hu, A. T. Ohta, and W. A. Shiroma, "A reconfigurable, liquid-metal-based low-pass filter with reversible tuning," *Wireless Symposium (IWS), 2013 IEEE International*, pp. 1–3, April 2013.

[91] N. Vahabisani, S. Khan, and M. Daneshmand, "Microfluidically reconfigurable rectangular waveguide filter using liquid metal posts," *IEEE Microwave and Wireless Components Letters*, vol. 26, no. 10, pp. 801–803, Oct 2016.

[92] M. M. Moorefield *et al.*, "A planar liquid-metal shunt switch," *2016 IEEE/ACES International Conference on Wireless Information Technology and Systems (ICWITS) and Applied Computational Electromagnetics (ACES)*, pp. 1–2, March 2016.

[93] A. J. Mitcham, D. H. Prothero, and J. C. Brooks, "Liquid metal switches for electromagnetic railgun systems," *IEEE Transactions on Magnetics*, vol. 27, no. 1, pp. 438–443, Jan 1991.

[94] A. M. Morishita *et al.*, "A liquid-metal reconfigurable log-periodic balun," *2014 IEEE MTT-S International Microwave Symposium (IMS2014)*, pp. 1–3, June 2014.

[95] D. Kim *et al.*, "Gallium-based liquid metal inkjet printing," *2014 IEEE 27th International Conference on Micro Electro Mechanical Systems (MEMS)*, pp. 967–970, Jan 2014.

[96] G. Li, X. Wu, and D. W. Lee, "A novel liquid metal-based inkjet nozzle for flexible electronics," *2015 Transducers - 2015 18th International Conference on Solid-State Sensors, Actuators and Microsystems (TRANSDUCERS)*, pp. 339–342, June 2015.

[97] A. M. Morishita, C. K. Y. Kitamura, A. T. Ohta, and W. A. Shiroma, "A liquid-metal monopole array with tunable frequency, gain, and beam steering," *IEEE Antennas and Wireless Propagation Letters*, vol. 12, pp. 1388–1391, 2013.

[98] C. K. Y. Kitamura *et al.*, "A liquid-metal reconfigurable yagi-uda monopole array," *Microwave Symposium Digest (IMS), 2013 IEEE MTT-S International*, pp. 1–3, June 2013.

[99] A. M. Morishita, C. K. Y. Kitamura, A. T. Ohta, and W. A. Shiroma, "Two-octave tunable liquid-metal monopole antenna," *Electronics Letters*, vol. 50, no. 1, pp. 19–20, January 2014.

[100] M. Wang *et al.*, "A reconfigurable liquid metal antenna driven by electrochemically controlled capillarity," *Journal of Applied Physics*, vol. 117, no. 19, 2015. [Online]. Available: http://scitation.aip.org/content/aip/journal/jap/117/19/10.1063/1.4919605

[101] M. Wang *et al.*, "Pump-free feedback control of a frequency reconfigurable liquid metal monopole," *2015 IEEE International Symposium on Antennas and Propagation USNC/URSI National Radio Science Meeting*, pp. 2223–2224, July 2015.

[102] A. Dey, R. Guldiken, and G. Mumcu, "Wideband frequency tunable liquid metal monopole antenna," *2013 IEEE Antennas and Propagation Society International Symposium (APSURSI)*, pp. 392–393, July 2013.

[103] A. Dey, R. Guldiken, and G. Mumcu, "Microfluidically reconfigured wideband frequency-tunable liquid-metal monopole antenna," *IEEE Transactions on Antennas and Propagation*, vol. 64, no. 6, pp. 2572–2576, June 2016.

[104] M. R. Moorefield *et al.*, "Frequency-tunable patch antenna with liquid-metal-actuated loading slot," *Electronics Letters*, vol. 52, no. 7, pp. 498–500, 2016.

[105] M. Kelley *et al.*, "Frequency reconfigurable patch antenna using liquid metal as switching mechanism," *Electronics Letters*, vol. 49, no. 22, pp. 1370–1371, Oct 2013.

[106] D. L. Diedhiou *et al.*, "Inset-fed liquid metal patch antenna," *The 8th European Conference on Antennas and Propagation (EuCAP 2014)*, pp. 1739–1741, April 2014.

[107] B. Aissa *et al.*, "Fluidic patch antenna based on liquid metal alloy/single-wall carbon-nanotubes operating at the s-band frequency," *Applied Physics Letters*, vol. 103, no. 6, 2013. [Online]. Available: http://scitation.aip.org/content/aip/journal/apl/103/6/10.1063/1.4817861

[108] A. Ha and K. Kim, "Frequency tunable liquid metal planar inverted-f antenna," *Electronics Letters*, vol. 52, no. 2, pp. 100–102, 2016.

[109] J. H. Dang *et al.*, "Liquid-metal frequency-reconfigurable slot antenna using air-bubble actuation," *Electronics Letters*, vol. 51, no. 21, pp. 1630–1632, 2015.

[110] R. C. Gough *et al.*, "Frequency-tunable slot antenna using continuous electrowetting of liquid metal," *2014 IEEE MTT-S International Microwave Symposium (IMS2014)*, pp. 1–4, June 2014.

[111] T. Anderson and I. Ansara, "The Ga-In (gallium-indium) system," *Journal of Phase Equilibria*, vol. 12, no. 1, pp. 64–72, 1991.

[112] M. D. Dickey, "Emerging applications of liquid metals featuring surface oxides," *ACS Applied Material Interfaces*, vol. 6, no. 21, pp. 18 369–18 379, 2014.

[113] W. M. Haynes, *CRC Handbook of Chemistry and Physics*, 92nd ed. CRC Press, 2011.

[114] R. N. Lyon, *Liquid Metals Handbook*, 2nd ed. U.S. Government Printing Office, 1952.

[115] S. Yu and M. Kaviany, "Electrical, thermal, and species transport properties of liquid eutectic Ga-In and Ga-In-Sn from first principles," *The Journal of Chemical Physics*, vol. 140, no. 6, p. 064303, 2014. [Online]. Available: http://dx.doi.org/10.1063/1.4865105

[116] Y. Plevachuk *et al.*, "Thermophysical properties of the liquid Ga-In-Sn eutectic alloy," *Journal of Chemical and Engineering Data*, vol. 59, no. 3, pp. 757–763, 2014.

[117] Y. I. Dutchak, V. Y. Prokhorenko, and E. A. Ratushnyak, "Resistivity of the ternary In-Ga-Sn eutectic system near the melting point," *Soviet Physics Journal*, vol. 13, no. 7, pp. 937–939, 1970.

[118] M. J. Regan *et al.*, "X-ray study of the oxidation of liquid-gallium surfaces," *Physical Review B*, vol. 55, pp. 10 786–10 790, Apr 1997. [Online]. Available: http://link.aps.org/doi/10.1103/PhysRevB.55.10786

[119] "Electrical conductivity of aqueous solutions," Department of Chemistry, Colorado State University. [Online]. Available: http://sites.chem.colostate.edu//diverdi/all_courses/CRC%20reference%20data/electrical%20conductivity%20of%20aqueous%20solutions.pdf

[120] "Table of conductivity vs concentration for common solutions," Wentworth Institute of Technology. [Online]. Available: http://myweb.wit.edu/sandinic/Research/conductivity%20v%20concentration.pdf

[121] G. Anderson, "Saltwater composition," Marine Science, 2003. [Online]. Available: http://www.marinebio.net/marinescience/02ocean/swcomposition.htm

[122] "pH," HyperPhysics. [Online]. Available: http://hyperphysics.phy-astr.gsu.edu/hbase/Chemical/ph.html

[123] "The pH scale with some common examples," PMEL NOAA. [Online]. Available: http://www.pmel.noaa.gov/co2/file/The+pH+scale+with+some+common+examples

[124] S. Lim and H. Ling, "Design of electrically small, pattern reconfigurable yagi antenna," *Electronics Letters*, vol. 43, no. 24, pp. 1326–1327, Nov 2007.

[125] B. H. Sun, S. G. Zhou, Y. F. Wei, and Q. Z. Liu, "Modified two-element yagi-uda antenna with tunable beams," *Progress In Electromagnetics Research*, vol. 100, pp. 175–187, 2010.

[126] "Oxygen connecting tubing, 7 foot, 3/16inch I.D." 2015. [Online]. Available: https://www.boundtree.com/oxygen-connecting-tubing-87-3007ea-pharm-8669-41.aspx?search=87-3007EA

[127] Y. T. Lo and S. W. Lee, *Antenna handbook*, 1st ed. Van Nostrand Reinhold, 1988.

[128] "Feko," 2015. [Online]. Available: https://www.feko.info/

[129] P. Jithu *et al.*, "Dual band monopole antenna design," *International Journal of Engineering and Technology (IJET)*, vol. 5, no. 3, 2013.

[130] K. Britain, "850-6500 MHz PCB LP," WA5VJB. [Online]. Available: http://www.wa5vjb.com/pcb-pdfs/LP8565.pdf

[131] J. T. MacDonald and D. R. Ucci, "Design of a passive element array," *2000 IEEE-APS Conference on Antennas and Propagation for Wireless Communications*, pp. 125–128, 2000.

[132] M. Meserve, "Martin e. meserve - K7MEM - yagi design help," K7MEM. [Online]. Available: http://www.k7mem.com/Electronic_Notebook/antennas/yagi_vhf_help.html

[133] C. Wolff, "Radar basics - yagi antenna," Radar Tutorial, 1997. [Online]. Available: http://www.radartutorial.eu/06.antennas/Yagi%20Antenna.en.html

[134] "Single-enclosure GPS anti-jam technology (GAJT) for marine applications," NovAtel, 2016. [Online]. Available: http://www.novatel.com/assets/Documents/Papers/GAJT-710MS-PS.pdf

[135] F. Leveau, S. Boucher, E. Goron, and H. Lattard, "Anti-jam protection by antenna," GPS World, 2013. [Online]. Available: http://gpsworld.com/anti-jam-protection-by-antenna/

[136] M. Wang, M. R. Khan, M. D. Dickey, and J. J. Adams, "A compound frequency and polarization reconfigurable crossed dipole using multi-directional spreading of liquid metal," *IEEE Antennas and Wireless Propagation Letters*, vol. PP, no. 99, pp. 1–1, 2016.

[137] N. Jin, F. Yang, and Y. Rahmat-Samii, "A novel patch antenna with switchable slot (PASS): dual-frequency operation with reversed circular polarizations," *IEEE Transactions on Antennas and Propagation*, vol. 54, no. 3, pp. 1031–1034, March 2006.

[138] Y. J. Sung, T. U. Jang, and Y. S. Kim, "A reconfigurable microstrip antenna for switchable polarization," *IEEE Microwave and Wireless Components Letters*, vol. 14, no. 11, pp. 534–536, Nov 2004.

[139] S. J. Mazlouman, A. Mahanfar, C. Menon, and R. G. Vaughan, "Reconfigurable axial-mode helix antennas using shape memory alloys," *IEEE Transactions on Antennas and Propagation*, vol. 59, no. 4, pp. 1070–1077, April 2011.

[140] J. Costantine *et al.*, "A reconfigurable/deployable helical antenna for small satellites," *2013 IEEE Antennas and Propagation Society International Symposium (APSURSI)*, pp. 390–391, July 2013.

[141] X. Liu *et al.*, "Reconfigurable helical antenna based on an origami structure for wireless communication system," *2014 IEEE MTT-S International Microwave Symposium (IMS2014)*, pp. 1–4, June 2014.

[142] Y. Zhou, S. Fang, H. Liu, and S. Fu, "A liquid metal conical helical antenna for circular polarization-reconfigurable antenna," *International Journal of Antennas and Propagation*, vol. 2016, pp. 1–7, 2016.

[143] *User's guide for building and operating environmental satellite receiving stations*, 2nd ed. National Oceanic and Atmospheric Administration (NOAA), 2009. [Online]. Available: http://noaasis.noaa.gov/NOAASIS/pubs/Users_Guide-Building_Receive_Stations_March_2009.pdf

[144] *Space Network Users' Guide (SNUG)*, 10th ed. National Aeronautics and Space Administration (NASA), 2012. [Online]. Available: https://elibrary.gsfc.nasa.gov/_assets/doclibBidder/tech_docs/4.%20450-SNUG%20-%20Copy.pdf

[145] "Polarization," University of Hawaii at Manoa. [Online]. Available: http://www.phys.hawaii.edu/~anita/new/papers/militaryHandbook/polariza.pdf

[146] P. Spychalski, "Antennas: power loss on polarization mismatch," Quad Me Up, 2016. [Online]. Available: https://quadmeup.com/antennas-power-loss-on-polarization-mismatch/

[147] K. Blattenberger, "Electronic warfare and radar systems engineering handbook - polarization," RF Cafe. [Online]. Available: http://www.rfcafe.com/references/electrical/ew-radar-handbook/polarization.htm

[148] S. J. Chen, T. Kaufmann, D. C. Ranasinghe, and C. Fumeaux, "A modular textile antenna design using snap-on buttons for wearable applications," *IEEE Transactions on Antennas and Propagation*, vol. 64, no. 3, pp. 894–903, March 2016.

[149] C. Chen, "Beamforming structure for modular phased array antennas," Nov. 10 1992, US Patent 5,162,803. [Online]. Available: https://www.google.com/patents/US5162803

[150] M. Johansson, S. Petersson, and S. Johansson, "Modular high-gain antennas," *2008 IEEE Antennas and Propagation Society International Symposium*, pp. 1–4, July 2008.

[151] D. Gioia, R. Uskali, and P. Kindinger, "Modular printed antenna," Sep. 11 2003, US Patent App. 10/093,877. [Online]. Available: https://www.google.com/patents/US20030169205

[152] G. Quagliaro, "Modular antenna system," Nov. 20 2003, US Patent App. 10/408,660. [Online]. Available: https://www.google.com/patents/US20030214454

[153] M. B. Lara *et al.*, "Modular interchangeable high power helical antennas," *2011 IEEE Pulsed Power Conference*, pp. 358–363, June 2011.

[154] D. Rodrigo, L. Jofre, and B. A. Cetiner, "Circular beam-steering reconfigurable antenna with liquid metal parasitics," *IEEE Transactions on Antennas and Propagation*, vol. 60, no. 4, pp. 1796–1802, April 2012.

[155] Y. Zhang and C. Wu, "An approach for optimizing the reconfigurable antenna and improving its reconfigurability," *2016 IEEE International Conference on Signal Processing, Communications and Computing (ICSPCC)*, pp. 1–5, Aug 2016.

[156] G. Kiesel and K. Cook, "Optimization of pixelated antennas," *2015 IEEE International Symposium on Antennas and Propagation USNC/URSI National Radio Science Meeting*, pp. 1328–1329, July 2015.

[157] J. Ashjaee *et al.*, "Dual-frequency choke-ring ground planes," Aug. 21 2001, US Patent 6,278,407. [Online]. Available: https://www.google.com/patents/US6278407

[158] C. D. Saintsing, B. S. Cook, and M. M. Tentzeris, "An origami inspired reconfigurable spiral antenna," *38th Mechanisms and Robotics Conference*, vol. 5B, 2014.

[159] E. E. Altshuler and D. S. Linden, "Design of a loaded monopole having hemispherical coverage using a genetic algorithm," *IEEE Transactions on Antennas and Propagation*, vol. 45, no. 1, pp. 1–4, Jan 1997.

[160] E. E. Altshuler and D. S. Linden, "Wire-antenna designs using genetic algorithms," *IEEE Antennas and Propagation Magazine*, vol. 39, no. 2, pp. 33–43, Apr 1997.

[161] M. R. Khan *et al.*, "Influence of water on the interfacial behavior of gallium liquid metal alloys," *ACS Applied Materials & Interfaces*, vol. 6, no. 24, pp. 22 467–22 473, 2014.

[162] E. M. Borges, F. A. Braz Filho, and F. N. F. Guimaraes, "Liquid metal flow control by dc electromagnetic pumps," *Thermal Engineering*, vol. 9, no. 1, pp. 47–54, 2010.

[163] L. J. Briggs, "Gallium: Thermal conductivity; supercooling; negative pressure," *The Journal of Chemical Physics*, vol. 26, no. 4, pp. 784–786, 1957.

[164] X. Y. Yin and G. S. Collins, "The solubility of indium in liquid gallium supercooled to 12 k," *Defect and Diffusion Forum*, vol. 323-325, pp. 503–508, 2012.

[165] "Fluidic factory 3d printer," Dolomite Microfluidics. [Online]. Available: http://www.dolomite-microfluidics.com/webshop/fluidic_factory

[166] "Antenna & radome design aids," COBHAM, 2001. [Online]. Available: http://www.cobham.com/media/83787/805-1.pdf